Characterization of radiochromic film to measure small photon field output factors

Thulani Mabhengu

(Student No:765996)

A dissertation submitted to the Faculty of Science, University of the Witwatersrand, Johannesburg, in fulfillment of the requirements for the degree of Master of Science (Physics)

Supervisor: **Dr. S.A Ngcezu**

Co-supervisor: **Prof. I.T. Usman**

Declaration

I declare that this dissertation is my own, unaided work. It is being submitted for the degree of master of science in physics at the University of the Witwatersrand, Johannesburg. It has not been submitted before for any degree or examination at any other University.

Thulani Mabhengu

28 April 2023

Date

Abstract

AIM: This study aimed to investigate radiochromic (EBT3 type) film's characteristics for the measurement of small photon field output factors and beam profiles for the field sizes ranging from 0.5 x 0.5 cm^2 to 10 x 10 cm^2 for the three photon energies, 6MV flattening filter free (FFF), 6MV flattening filter (FF), and 10MV FF.

MATERIALS AND METHODS: Small-field dosimetry poses significant challenges and remains an active area of research in medical physics. In this study, radiochromic film (RCF), specifically Gafchromic EBT3 was used for small field measurements. The performance of RCF was compared with other conventional detectors such as ionization chambers, and a two-dimensional (2-D) detector amorphous silicon electronic portal imaging device (a-Si EPID). In addition, a comparison of the film measurements with software-calculated data, i.e, treatment planning system (TPS) was conducted.

RESULTS: The field output factors (FOF) measured with EBT3 film compared to the TPS data for the smallest field size of 0.5 x 0.5 cm^2 was found to be less or equal to 0.06% in all three photon energies. Volumetric detectors in 6MV FF beam showed an increase in % difference of up to 0.3 higher than the EBT3 film and TPS data. A higher quantitative percentage difference of 0.6% in FOF measured with a-Si EPID compared with the RCF data was observed in the smallest field size of 0.5 x 0.5 cm^2 in higher energy beam, 10MV FF beam.

CONCLUSION: The properties of RCF such as tissue-equivalent, less photon perturbation as well as volume averaging effects improve the accuracy of FOF measurements in small-fields compared to the ionization chambers utilized in this study. Therefore, RCF could serve as a reliable reference detector for small-field measurements.

Dedication

In memory of my mother

Ntombizanele Mabhengu

1942 - 1989

and my brother

Xolani Templeton Mabhengu

1967 - 2011

Acknowledgments

I would like to express my deepest gratitute to my supervisor, Dr. S.A Ngcezu for his patience, guidance, encouragement, and professional critique. I was privileged to experience his exceptional scientific knowledge. To my wonderful co-supervisor, Prof. I.T Usman for her constant support, prompt response, constructive suggestions, and positive outlook in my research.

A special thanks to Ms L.A Segone for her assistance with EPID configuration and measurements and Ms N. Masango for spending her weekends at CMJAH assisting me with the measurements. The contributions and suggestions made by Mr N. Maphumulo are highly appreciated. To Mr. M. Boroto, and Mr L.C. Nethwadzi for their valuable contributions on my research. To Mr P. Sithole, Mr. S.T Temaugee and Mr. J. Mbewe for assisting me with the latex writting. To my friend, my brother, and my confidante Mr B. Van Wyk, thank you so much for always being there for me during tough times. I would also like to thank Charlotte Maxeke Johannesburg Academic Hospital (CMJAH) for allowing me to use their equipment.

I would not have completed this work without the emotional support of my family, my lovely wife, my pillar of strength Ms Thembisa Mabhengu for her unconditional love and endless support, my two eldest daughters Nasiphi Mabhengu, and Mandisa Mabhengu, my one and only son Athule Mabhengu, and my last born Uyanda Mabhengu.

Last, but not least, to my late brother Xolani Templeton Mabhengu and my brother Baphathe (Pat) Mabhengu, I am forever grateful for your patience, support and limitless sacrifices; without the two of you "bakhuluwa bam" I would not have reached this far. Ndiyambulela kakhulu u-Thixo ngani bafowethu.

Contents

List of Figures

List of Tables

List of abbreviations

AAPM	American Association of Physicists in Medicine
a-Si	Armophous Silicon
CAX	Central Axis
CMJAH	Charlotte Maxeke Johannesburg Academic Hospital
CPE	Charged Particle Equilibrium
CT	Computed Tomography
D_{max}	Depth of maximum dose
DICOM	Digital Imaging and Communication in Medicine
DR	Dose rate
dpi	Dots per inch
EPID	Electronic Portal Imaging Device
FF	Flattening Filter
FFF	Flattening Filter Free
FOF	Field Output Factor
FOCF	Field Output Correction Factor
F/S	Field Size
FWHM	Full Width at Half Maximum
Gy	Gray
HU	Hounsfield Units
IAEA	International Atomic Energy Agency
IC	Ionization Chamber
IMRT	Intensity Modulated Radiation Therapy
LCPE	Lateral Charged Particle Equilibrium
LEDE	Lateral Electronic Disequilibrium Effect
Linac	Linear Accelerator
msr	Machine Specific Reference
Meas	Measured
MeV	Mega electron-volt
MLC	Multi-Leaf Collimator

MP	Medical Physicist
MV	Megavolt
OD	Optical Density
OF	Output Factor
PDD	Percentage Depth Dose
Pub	Published
PP	PinPoint
RCF	Radiochromic Film
ROI	Region Of Interest
SAD	Source to Axis Distance
SDD	Source to Detector Distance
SFD	Source to Film Distance
SF	Semiflex
S_{clin}	Specific clinical equivalent square field
SRS	Stereotactic Radiosurgery
SRT	Stereotactic Radiotherapy
SSD	Source to Surface Distance
TG	Task Group
TPR	Tissue Phantom Ratio
TPS	Treatment Planning System
TRS	Technical Report Series
3-D	Three Dimensional
2-D	Two Dimensional
VMAT	Volumetric Arc Therapy

Chapter 1

Introduction

Various modalities, including surgery, chemotherapy and ionizing radiation, are used for cancer management [1]. Radiotherapy is a major modality in the modern cancer management [2]. Various ionizing radiation types such as X-rays, electrons, protons, etc are employed in radiotherapy, with different unique physical and radiobiological properties for killing cancerous cells. They deposit energy as they pass through tissues in the body to cause damage to the DNA in the cancer cells. Advanced radiotherapy techniques such as external beam, brachytherapy, and proton therapy are used for precise targeting of the tumor while sparing healthy tissues. This is achieved through dose fractionation over a period of time to allow normal cells to repair [3].

In the radiotherapy unit, the clinical team comprises radiation oncologists, medical physicists, radiation therapists, as well as the nursing staff. The primary role of clinical medical physicists (MP) is to design, and implement radiation treatment plans for cancer patients. This involves working closely with the radiation oncologists to determine the appropriate radiation dose is delivered to the tumor volume while minimizing the dose to the surrounding critical organs [2].

Historically, in the era of two dimensional (2-D) treatment planning, large non-conforming photon fields were used in radiation therapy to treat different cancer sites. The use of large radiation fields had serious limitations in the practice of radiotherapy; for example, the constraints of dose escalation to reach an optimum dose level for tumour control due to the dose-limiting organs at risk. The consequences of these limitations have resulted in high treatment toxicity and sub-optimal tumour control [4]. However, the introduction of

three-dimensional (3-D) treatment planning which is primarily based on the use of a computed tomography (CT) scanner led to the visualization of the target and surrounding normal tissues. Multi-leaf collimators (MLCs) instead of cerrobend blocks were used to shape the treatment field. In 3-D treatment planning, uniform fluence is delivered to the patient. This results in a higher dose to normal tissues with no improvement in target coverage of complex shapes [5].

Modern treatment planning is done through intensity-modulated radiotherapy (IMRT) and volumetric modulated arc therapy (VMAT). IMRT technique is associated with inverse treatment planning to determine optimal fluence profiles. The non-uniform fluence is delivered by the movement of MLCs in a linear accelerator (Linac). The more advanced technique called VMAT improved the accuracy and efficiency of IMRT. In VMAT technique, modulation of the beam intensity and dose rate, movement of the leaves and gantry rotation around the patient are performed simultaneously. These new modalities are employing small fields for better targeting and conformance to reduce toxicity and escalate the dose to the tumor for better control [4]. Modern radiotherapy is driven by technological advances that have ushered in delivery techniques capable of significant improvements in planning and delivering more conformal isodoses for better clinical outcomes [4].

With the introduction and ubiquitous use of IMRT and VMAT, an era of small photon fields treatment delivery presents new treatment solutions with accompanying challenges. IMRT and VMAT effectively uses small photon fields created by MLC to modulate the beam intensity to maximize treatment goals. However, there are practical and dosimetric challenges associated with small photon beams. Small photon fields are now applied in modern radiotherapy for IMRT treatments, VMAT, Stereotactic Radiosurgery (SRS) and in Stereotactic Body Radiotherapy (SBRT) to achieve maximum dose to the target volume and to spare healthy tissues/organs around the target [6]. These advanced treatment techniques produce treatment plans with small beam apertures that produce steep dose gradients for better dose distributions [7]. The treatment fields produced by modern radiation therapy modalities are considered small and are exceedingly difficult to measure and model [8]. Therefore, quality assurance (QA) programs including the treatment planning system checks and patient-specific QA should be established in the radiotherapy de-

partment to ensure safety and accurate delivery of IMRT and VMAT. Some of the challenges can be addressed with treatment planning systems equipped with good optimization algorithms and well-trained personnel in IMRT/VMAT planning and delivery.

Radiotherapy machines that can be used to deliver the advanced treatment planning regimes for example Cyberknife has been used for treatment using small radiation fields and has been used for years in the irradiation of small lesions. Conventional linacs can now treat small lesions down to a field size of 0.5 x 0.5 cm^2. Therefore, irradiation of small photon fields has, as a result, become standard in radiotherapy. However,there are fundamental differences between dosimetric measurements in larger field sizes and smaller photon fields [9].

The response of different small field detectors varies significantly in small beams. Small photon field measurements require high precision in both absolute and relative dosimetry [9]. According to the joint International Atomic Energy Agency and American Association of Physicists in Medicine (IAEA-AAPM) code of practice in static small photon fields, any field size that meets the following conditions is regarded as a small field [9]:

- Loss of lateral charge particle equilibrium
- Partial occlusion of the photon source by the collimating device on the beam axis
- The size of the detector is larger or similar to the beam dimensions

The protocol [9] covers the dosimetry of small static fields in external beam radiotherapy. These challenges with small field measurements are discussed comprehensively in chapter two as per the IAEA-AAPM code of practice.The method of measuring output factors in small photon fields for different detectors is well explained in TRS 483 [9], except for film dosimeters. The IAEA-AAPM code of practice recommends using more than one detector for small fields measurements. The protocol presents procedures for measuring small photon field output factors, correction factors and their uncertainties. The film is recommended in TRS 483 as one of the best detectors to use in small photon fields [10]; however, the protocol does not describe the procedure on how to measure small fields using a film. Uncertainties in estimating small field output correction factors are clearly described and presented in Table 37

of the IAEA-AAPM small photon field protocol for different types of detectors except for film [10].

Currently; there are few protocols available for film measurements to guide clinical medical physicists in small-field measurements [11]. Several studies have shown the use of vented ionization chambers and solid-state detectors in small field dosimetry and provided correction factors for the estimation of field output factors [12, 13, 14], this study added to the body of work on film dosimetry as an alternative dosimeter that has desirable properties to overcome the limitations of volumetric detectors in a small field.

In the literature, researchers used various chambers to measure the output factors to look at the response of each chamber at different field sizes [15, 16, 17, 18, 19]. The amount of time spent in the machine to obtain an accurate set-up to perform measurements is still a big challenge in small photon fields. Thus far, there is no ideal detector for small photon field measurements [20]. The existing protocol recommends using more than one detector for small field measurements and comparing the results with published data.

Currently, film is used in radiation therapy mostly to measure flatness and symmetry, radiation versus light field, as well as a two-dimension (2-D) dosimeter to provide a map of intensity distribution which is converted to dose through characteristic curve [21]. Film presents unique challenges in dose measurements compared to other detectors. Variations in film orientation with respect to the incident radiation, its response over a wide range of doses, post-exposure changes, and the uncertainties in calibration due to batch-to-batch variability should be taken into consideration in setting up the film for dose measurements. Handling of films prior to measurements, and the scanning resolution used to accurately measure the dose within the area of interest can affect the film response to radiation. Despite these challenges, RCF provides higher spatial resolution in dose measurements. Therefore, appropriate calibration protocols and guidelines must be followed; appropriate software for film analysis is required [11].

This study aims to investigate and characterize the use of film and its associated uncertainties in output factors measurements. The method for performing dosimetry measurements in small photon fields using the EBT3 Gafchromic

film which is a type of radiochromic film is described and compared with small ionization chambers obtained in the facility and from the published literature. In addition, data acquired from EPID detectors were also compared with film results.

1.1 Problem Statement

This study seeks to address the following research questions emanating from the published joint International Atomic Energy Agency (IAEA) and American Association of Physicists in Medicine (AAPM) code of practice, TRS-483, for the dosimetry of static small photon fields) as a guide on how to perform dosimetry in small photon fields:

- Does film dosimetry improve the accuracy of data collection and overcome some or all the limitations of the small volumetric detectors used in small fields?
- Are the benefits of using film outweigh the challenges of setting up the film dosimetry protocol for small fields?
- Can film be used as a standard detector for small fields in radiotherapy departments to eliminate all the challenges in the alignment of the small volumetric detectors with the central axis of the beam?
- Does film dosimetry have superior accuracy compared to all the detectors listed in the IAEA/AAPM Code of Practice for the Dosimetry of Static Small Photon Fields (TRS483)?

1.2 Research Objectives

The main objective of this study is to characterize the EBT3 film to perform field output factor measurements in small photon beams. Examine film results against volumetric detectors that are used in small field measurements. Review these two methods and analyze the uncertainties. In order to achieve this aim the following objectives need to be accomplished:

- Comprehensively review the measured small photon field data for Elekta versa HD Linac at CMJAH to verify the errors and the challenges encountered with ionization chambers in small photon fields due to their dimensions.

- Compare the results with published data.
- Set-up and characterize radiochromic film for measurement in small fields using three photon energy beams equipped with flattening filters (WFF), 6 MV photon beam free of the flattening filter (FFF), and 10MV with flattening filter (WFF) photon energy beams which are commonly used in small field treatments.
- Determine all the sources of uncertainties in the dose measured with film versus the dose measured with other detectors.
- Establish a standard procedure used at CMJAH to measure the small photon fields data using film accurately.

1.3 Outline of Dissertation

Chapter one provides an introduction of the main modalities used in cancer management. The purpose, motivation and some research questions to be addressed by this study are covered in the introductory chapter.

Chapter two gives a literature review on some concepts and definitions used in dosimetry of small static fields. The challenges encountered with various detectors in small photon fields are discussed in detail in this chapter. The field output factor is defined according to the new IAEA protocol. The use of radiochromic films in small photon fields is covered comprehensively.

Chapter three provides the materials and the methodology followed in setting-up a proper protocol for film dosimetry as well as data acquisition for EPID.

Chapter four provides the results and discussions of the measured data (dose profiles and FOF) with various detectors.

Chapter five gives the conclusion and recommendation based on the results obtained in this study.

Chapter 2

Literature review

2.1 Introduction

Thus far, there is no ideal detector for small photon field measurements. Consequently, there is more interest in investigating the ideal detector to perform accurate measurements in small photon fields. The existing protocol recommends using more than one detector for small-field measurements [9] and comparing the results with the published data.

In modern radiotherapy, a high conformal dose to the target is delivered with a very small field, obviating the need for an accurate and reliable dosimetry system for applications in radiotherapy. Sources of uncertainty in small areas are described in the new protocol[9, 20].

2.2 Small photon field size

A seminal document focused on a well-established framework developed by a combined effort by the International Atomic Energy Agency (IAEA) in collaboration with the American Association of the medical physicist in Physics and Medicine (AAPM) came up with the following three physical conditions to define a small photon field [9]:

- Loss of lateral charged particle equilibrium
- Partial occlusion of the photon source by the collimator
- Size of the detector

2.2.1 Lateral Charged Particle Disequilibrium

In relative dosimetry measurements, photons create charged particles in the chamber wall, and some of these charged particles deposit their energy in the chamber-sensitive volume while others are scattered away from the volume.

Charged particle equilibrium (CPE) is the condition in which the electrons leaving the chamber collecting volume are compensated by those entering the volume. Therefore, the loss of lateral charged particle equilibrium (LCPE) refers to the lack of laterally scattered electrons created by photons upon interaction with the medium in which the detector does not measure these electrons. However, some of the electrons will scatter and leave the chamber's sensitive volume. This is due to the dimensions of the beam being too small in relation to the length of the electrons.

As illustrated in Figure 2.1, incident photons create secondary electrons in all different directions. The detector measures most of the laterally scattered electrons created within the field borders at point A. Point B depicts the non-equilibrium effect in which most secondary electrons produced outside the field borders do not contribute to the dose [22].

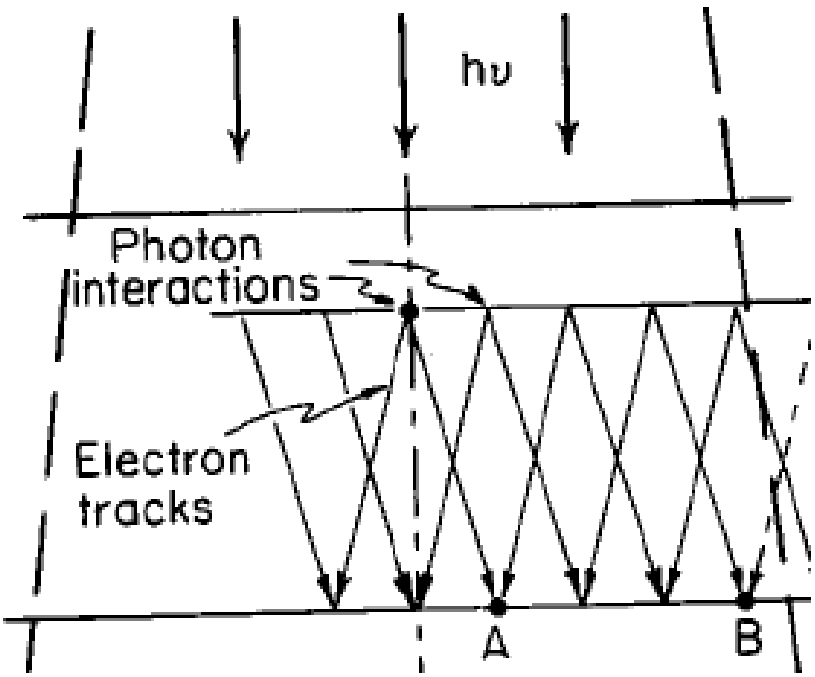

Figure 2.1: Lateral charged particle equilibrium (point A), and the loss of electronic equilibrium (point B) at the field borders. (Diagram from Ref.[22]).

In contrast, in large field measurements, the detector collects all the electrons that get scattered in a lateral direction towards the field borders. However, as stated above, small fields are characterized by the lack of lateral charged particle equilibrium caused by the short range of charged particles; therefore, most used detectors are subject to a low signal [9, 23, 24, 25].

For a charged particle equilibrium to exist, the number of particles entering the chamber-sensitive volume must be the same as the number of charged particles leaving it [10]. Therefore, enough scattering area around the detector is required. This limits the smallest field size that can be measured with a volumetric detector. Hence smaller sensitive volume detectors are essential for measuring radiation field output factors in small photon fields. This phenomenon depends on the radius of the ionization chamber volume and becomes worse in higher energy photon beams and lower density medium [26].

As the photon energy increases, the electron range increases. Figure 2.2 shows the ratio of dose (D) to collisional kerma (K_{col}) as a function of radius of a photon field [27]. As shown in the figure below, the LCPE depends on the energy of the photon beam. The LCPE for Co-60 is fulfilled at the cavity radius of 0.5 cm. In contrast, for 24 MeV the LCPE is achieved at 2.5 cm volume radius. At the largest cavity radius of 3 cm, the ratio of dose to collisional kerma is almost the same for all different photon energies. For 1 cm radius, the ratio of dose to collisional kerma becomes less than one for 6 MV, 10 MV,15 MV, and 24 MV photon energies. The radius of the field where the charged particle equilibrium is maintained is calculated based on the beam quality [9]

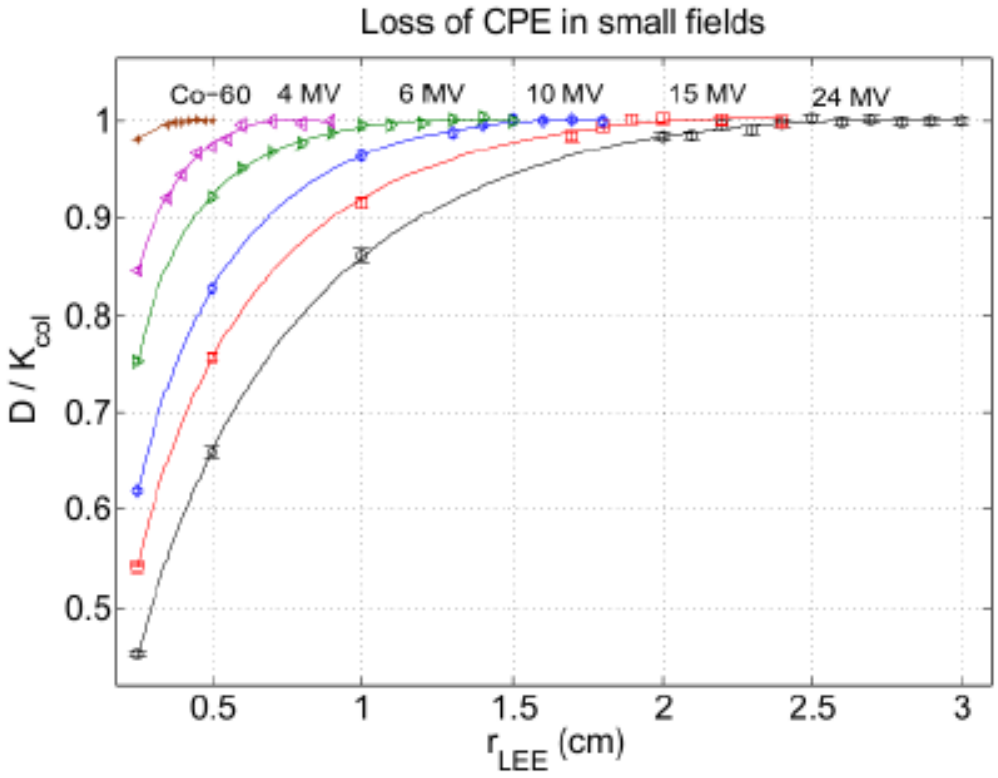

Figure 2.2: Ratio of dose to collisional kerma (D/K) for different energies as a function of radius is used to illustrate the loss of LCPE. (Diagram from Ref.[9]).

2.2.2 Partial occlusion of the photon source

For standard fields, the primary photon fluence is uniformly distributed. Photons are emitted from different parts (both left and right sides) in the target, not from a point source. If the collimator jaws are closed, photons that are emitted from both the target's left and right sides are attenuated by the jaws. Only photons emitted along the central part will reach the detector. Therefore, the two penumbras (left and right) overlap due to a small collimator opening, which results in dose exaggeration in the penumbra region .The penumbra for small fields becomes very large and overlap with the primary photon fluence.This overlap of the penumbra results in large FWHM compared to the actual collimator settings [13].

Source occlusion arises when the field size is reduced and the collimating devices partially block the direct beam [26]. Contrary to large fields, the radiation field size in small beams is defined by the FWHM instead of the jaw settings [26]. The dose at the beam's central axis is underestimated due to the decrease

in the scattering distribution. This results in a decrease in the field output factors due to reduced scatter and direct fluence [9]. The partial occlusion effect is illustrated in Figure 2.3 below, the collimator jaws block a portion of the focus, and the two penumbras overlap. Only the fraction of the detector is struck by the primary photon fluence.

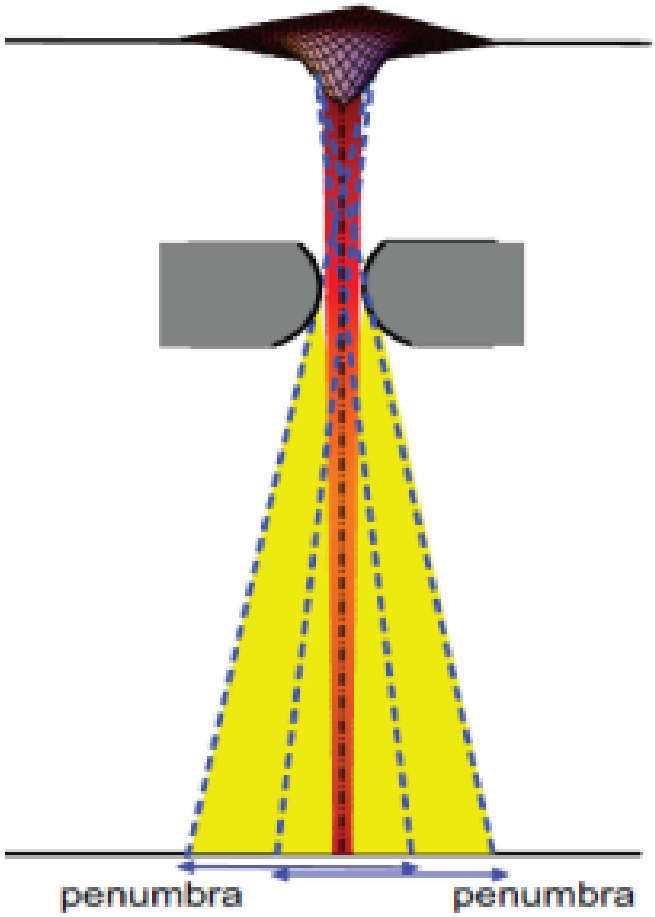

Figure 2.3: Photon source occlusion by the collimator jaws. Only the central axis of the beam is clearly visible. The two penumbras overlap due to a small collimator opening(Figure from Ref.[13]).

This effect is common in field sizes less than 3 x 3 cm^2 for measurements performed using volumetric detectors [10]. The accuracy in the alignment of the detector is significantly low causing a big dosimetric uncertainty in small field measurements [28].

2.2.3 Detector size

In broad beams, the entire sensitive volume of the chamber is irradiated by the flat region of the beam. The detector averages the collected signal over its

sensitive volume [13, 29]. Contrary to small fields, the sensitive volume of the detector may be bigger than the dimensions of the beam. Therefore, only a portion not the entire chamber-sensitive volume is irradiated by the primary photon fluence. However, the measured signal is averaged over the entire sensitive volume of the detector.

Volume averaging is one of the detector-related effects in small fields. This effect occurs in larger volume detectors with respect to beam size. It is a phenomenon in which the signal produced by the detector is the mean average dose over its sensitive volume [29]. This effect can be observed in a 1 x 1 cm^2 beam profile depicted in Figure 2.4 below.

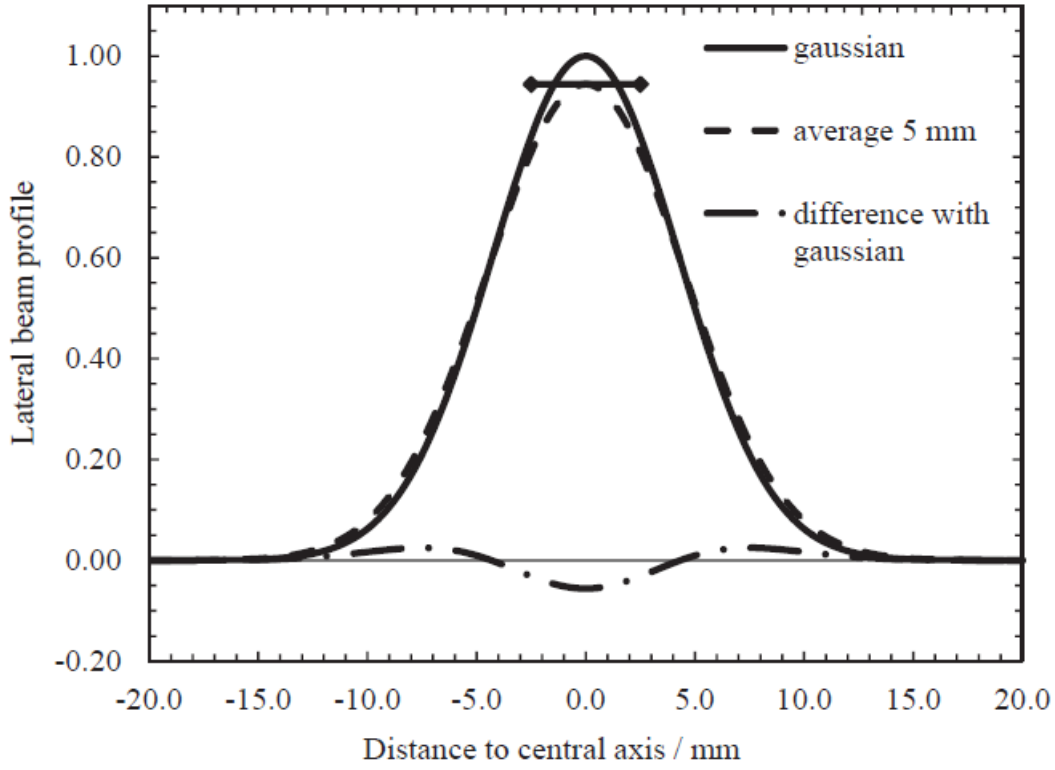

Figure 2.4: Volume averaging effect of the dose profile measured with a large detector compared to the dimensions of the beam size. The output of the field is represented by the solid Gaussian function, detector sensitive volume is represented by the double arrows, and the dashed lines are representing the measured value (Image from Ref.[9]).

In a situation where the volume averaging effect occurs, the dose in the center of the small field may be underestimated [9]. The dashed line shows beam profile measured by a detector similar or larger compared to the beam dimensions. The signal is significantly reduced at the center of the field where

the detector is not fully irradiated due to the chamber sensitive-volume which is bigger than the dimensions of the beam [30]. At 50 % isodose, volume averaging effect is not visible.

2.3 Absolute dosimetry

In clinical practice, clinicians prescribe treatment to the patient using the quantity absorbed dose. Related to this quantity is the so-called "output" from the treatment unit, which should be a measurable and reproducible quantity for accurate treatment delivery [26].

This is important because the amount of radiation dose given to patients correlates to radiotherapy treatment outcomes. Therefore, the prescription and prediction of clinical outcomes needs the knowledge of the absorbed dose for the planning target volume to be covered and delivered accurately with an uncertainty of less than 5% [31].

2.3.1 Output calibration

Linear accelerators (Linacs) are calibrated to deliver one cGy per monitor unit (1cGy/MU) for a field size of 10 x 10 cm^2 at a depth of maximum dose (dmax) using either 100 cm from the source to chamber distance (SCD) or 100 cm from the source to surface distance (SSD). This is critical in dosimetric calculations and ensuring treatment uniformity in prescriptions around the world [26] for the interpretation of fractionation schemes.

The absorbed dose refers to the energy imparted to a medium per unit mass (joules per kilogram) [32].

$$D = \frac{d\bar{E}}{dm} \tag{2.1}$$

Where $d\bar{E}$ is the mean energy deposited to a medium, and dm is the mass of the absorbing material. This absorbed dose is prescribed to patients in gray (Gy) for their treatment in radiotherapy. It is estimated through absolute dosimetry measurements in a water phantom with a farmer-type ionization chamber using international dosimetry protocols (i.e. The IAEA TRS-398) [33].

2.3.1.1 Farmer-type ionization chamber

The cylindrical farmer-type ionization chamber with a sensitive volume of 0.6 cm^3 is a gas-filled detector. The chamber operate at 300 volts and is based on the principle of relating the amount of energy deposited in the chamber volume to the size of the created ion pairs. Photons interact in a gas-filled detector to produce ion pairs which are collected by an electrode and then by an electrometer [29].

The amount of charge generated in the gas by ionizing radiation as it passes through the air cavity is measured strictly with a 0.6 cc farmer-type chamber in absolute dosimetry. Its response is characterized by well-established correction factors such as recombination, polarity, temperature and pressure [34].

Figure 2.5 shows a schematic diagram of a farmer typer chamber. This is a detector that is used mostly for calibrating the machine output in radiotherapy.

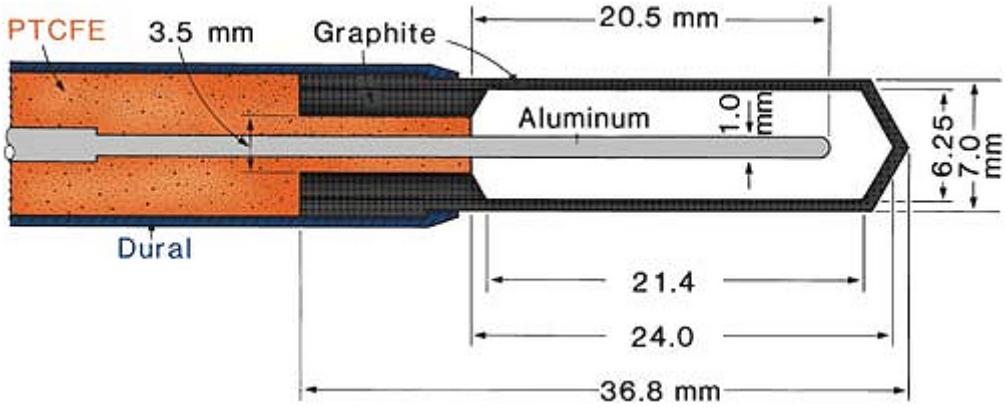

Figure 2.5: Schematic diagram of a graphite/aluminum ionization chamber with sensitive air volume of 0.6 cc and the central electrode.(Figure from Ref.[34]).

In absolute dosimetry, specific reference conditions are defined to perform dose rate measurements to a clinical relevant depth[26]. In current clinical practice, two protocols are widely used in reference dosimetry: American Association of Physicists in Medicine, Task Group 51 (AAPM TG-51) [35], and the International Atomic Energy Agency Technical Report Series (IAEA TRS) 398 [33].

2.3.2 Bragg-Gray cavity theory

Photons are indirectly ionizing; they transfer their energy to electrons in the irradiated medium. The electrons, in turn are released and deposit their energy into the gas in the cavity of the ionization chamber. The electron stopping power dictates the probability of this process. The stopping power refers to the energy lost by an electron per unit length in a medium [36].

Bragg-Gray cavity theory is the foundation of absolute dosimetry measurements. This theory provides a translation formula relating the doses in two media [37]. The dose measured in the gas inside the ionization chamber must be converted to the absorbed dose to water at the effective point of measurement of the chamber. Bragg-Gray cavity theory is then applied to convert the dose measured in the chamber to the dose in the medium for both higher-energy photons and electrons using the following expression [34]:

$$D_{water} = J_{gas} \left(\frac{\bar{W}}{e} \right) \left(\frac{\bar{S}}{\rho} \right)_{gas}^{water} \tag{2.2}$$

Where D_{water} is the absorbed dose to water, J_{gas} is the charge produced per unit mass of the air cavity, corrected for influence quantities such as temperature and pressure (P_{TP}), ionization collection efficiency (P_{ion}), replacement correction for the perturbation in the fluence due to the placement of the chamber in the medium (P_{repl}), and the wall correction when the chamber wall and phantom composition are different (P_{wall}), $\left(\frac{\bar{W}}{e} \right)$ is the average energy required to produce a certain amount of charge which is approximately 33.97 Joules per coulomb (J/C) in dry air, and $\left(\frac{\bar{S}}{\rho} \right)_{gas}^{water}$ is the mean mass stopping power ratio of water to gas of electrons crossing the air cavity.

However, the charge generated in the gas-filled cavity is measured in absolute dose measurements, not the dose. Therefore, the charge reading to a point in a medium needs to be converted to dose. Many correction factors are applied to convert the charge to dose: the first step is to correct the measured charge for temperature and pressure, and ion recombination correction to account for the fact that not all charges generated within the chamber volume will be measured. Some of the positive and negative particles may recombine and not be measured by the electrode, and the direction of the applied polarity across the chamber can affect the reading (chamber polarity) [34].

Second, the detector calibration factor is applied to convert the measured charge into the energy deposited in a gas within the chamber volume (dose). The dose provided by this calibration factor is measured for the Co-60 beam under reference conditions [26]. The Co-60 beam is different from the linear accelerator beams. The beam quality conversion factor is provided in the TRS398 tables as a function of the beam quality index to relate the clinical beam quality to that of the Co-60 beam [33].

Once the dose to the gas in the cavity is known, the final step transfers the dose to water from the absorbed dose in the gas through the ratio of the collision stopping power of water to that of gas in the cavity. Thus, the application of the Bragg-Gray cavity theory converts the dose from the detector effective volume to the absorbed dose in water [37].

The theory uses the mean collision mass stopping powers ratio to convert the dose measured in one medium to another [37]. In practice, the application of the Bragg-Gray cavity theory is done under the following important assumptions:

- The cavity must be small compared to the charged particle range [29]
- The charged particle fluence must be the same in both media (water and gas) [26]
- The absorbed dose in the cavity is deposited by the charged particles crossing not photons [37]

2.3.3 Spencer-Attix theory

The Bragg-Gray cavity theory assumes that the dose measured within the chamber volume is the same as the dose deposited around the detector. However, if there is a difference in energy absorbed and energy released, this theory is inaccurate in describing the dose in two media. Therefore, the accuracy of the Bragg-Gray cavity theory is modified by considering restricted stopping powers in the absorbed dose determination [26]. This is known as the Spencer-Attix formalism; developed by J. S. Spencer and F. H. Attix [37].

The Spencer-Attix theory recommends the use of the ratio of energy absorbed

in two media instead of the mean collisional stopping powers. Hence the restricted stopping power ratio instead of the collisional stopping power ratio is used to relate the dose in two different media [38]. The amount of energy absorbed from the electron passing through a medium per centimetre can be approximated. Therefore, the dose to water is calculated from the dose to air by using the following equation [37]:

$$D_{water} = D_{gas} \left(\frac{\bar{L}}{\rho} \right)_{gas}^{water} \tag{2.3}$$

Where D_{gas} is the dose to air cavity and $\left(\frac{\bar{L}}{\rho}\right)_{gas}^{water}$ is the restricted stopping power ratio. Detectors can impact the measurements when placed in the central axis of the beam; the fluence at the point of measurement is perturbed which alters the dose when water is replaced with a detector [39]. Perturbation correction is needed if the detector density material differs from water. This changes both the way that electrons are set in motion and their fluency [26].

2.4 Relative dosimetry

The accuracy of the treatment planning systems relies on dose calculation algorithms. Therefore, beam variation with depth, field size, energy, and source-surface distance (SSD) is characterized for accurate radiation dose delivery. Relative dosimetry is performed to determine the shape of the dose distribution within an absorbing and scattering medium.

The change in field size, beam energy, and SSD can affect the dose distribution within the patient. This dose distribution is generated by several sources: the primary beam from the target, the head scattered photons, and the photon scattered within the patient. The dose delivered to a target is proportional to the number of electrons passing through the area.

The dose to a point is contributed by the electrons from the surrounding material and is characterized by percentage depth dose (PDD), beam profile, and beam output factor. There are different parameters used to analyze the dose distribution within the patient. They are measured for a wide range of field sizes for treatment planning and radiation dosimetry purposes [8, 10, 34].

2.4.1 Percentage depth dose

The knowledge of how the dose from the radiotherapy beam is distributed with depth inside the patient is required. This dose distribution at each point in a water phantom is modeled through percentage depth dose (PDD). PDD is defined as the dose in percentage at any given depth to the dose at a depth of maximum [34]. PDD describes how the dose varies with depth and is approximated by the following equation:

$$PDD = \frac{D_{depth}}{D_{dmax}} * 100 \tag{2.4}$$

Where D_{depth} is the dose at any depth along the beam's central axis and D_{dmax} is the maximum dose at a certain depth in tissue or water.

This parameter is measured mostly with an ionization chamber in a scanning water tank along the beam's central axis. The dose is measured in the up and down movement while the beam is on at a constant source to surface distance (SSD). The PDD has a build-up region to a depth of maximum dose and drops exponentially at a deeper depth as shown in Figure 2.6.

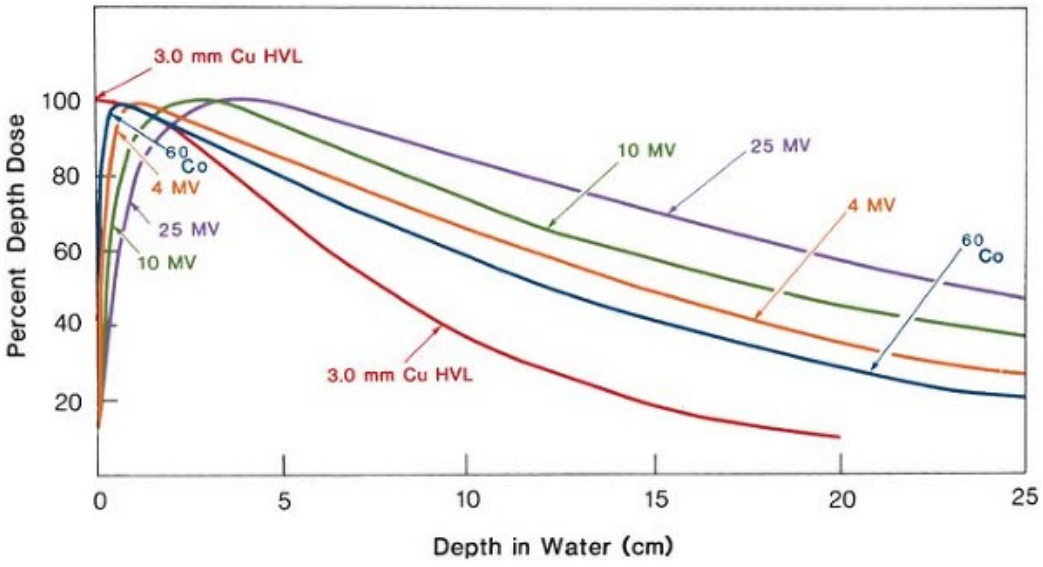

Figure 2.6: Depth dose distribution measured along the beam's central axis for different photon energies at a reference field size of 10 x 10 cm^2 (Figure from Ref.[34]).

.

The surface dose in photon beams is caused by electron contamination through the treatment head of the linear accelerator. Photon interactions

occur at a deeper depth compared to electron beams. This is known as the skin-sparing effect in photon beams. The amount of dose at each depth varies with beam energy, hence the depth of maximum dose for each photon and electron energy beam differs. The Build-up region is underneath the surface, low dose with no sufficient medium above. The dose is proportional to the number of electrons passing through the point in a medium. More electrons are passing through at the depth of maximum dose; hence there is a high dose. The fall-off region is due to photon attenuation. Scattered photons do not contribute to the percentage depth dose in small fields [34, 36].

2.4.2 Dose profiles

Dose distribution and variation away from the central axis are quantified with beam profile measurements [26]. Dose profile measurements are performed by scanning across the center of the beam at a reference depth of either 5 cm or 10 cm, and the SAD of 100 cm. The dose at each point is normalized to the dose at the beam's central axis. Beam profiles are more important in the treatment planning beam modeling to ensure that the prescribed dose covers the target volume.

The beam profile is divided into two regions: the central region and the penumbra region [26]. The central region is the uniform high dose region that is delivered inside the target volume. The low dose region on the sides of the beam dimensions where the dose drops rapidly is known as the beam penumbra.

Generally, the points at the center of the beam (umbra region) receive enough radiation dose compared to points in the beam penumbra region. The penumbra is wider in large field sizes compared to small photon fields. Some areas outside the beam are not irradiated, yet they are getting a full dose. The entire beam in a small photon field is the penumbra, and the beam profile has no flat portion in the middle [40].

Beam penumbra is defined at the beam edges as the distance between 20% and 80% of the maximum dose. It is a combination of both the physical feature which is related to the source size, and the dosimetric aspect due to electrons scattered at the field edge [34, 36].

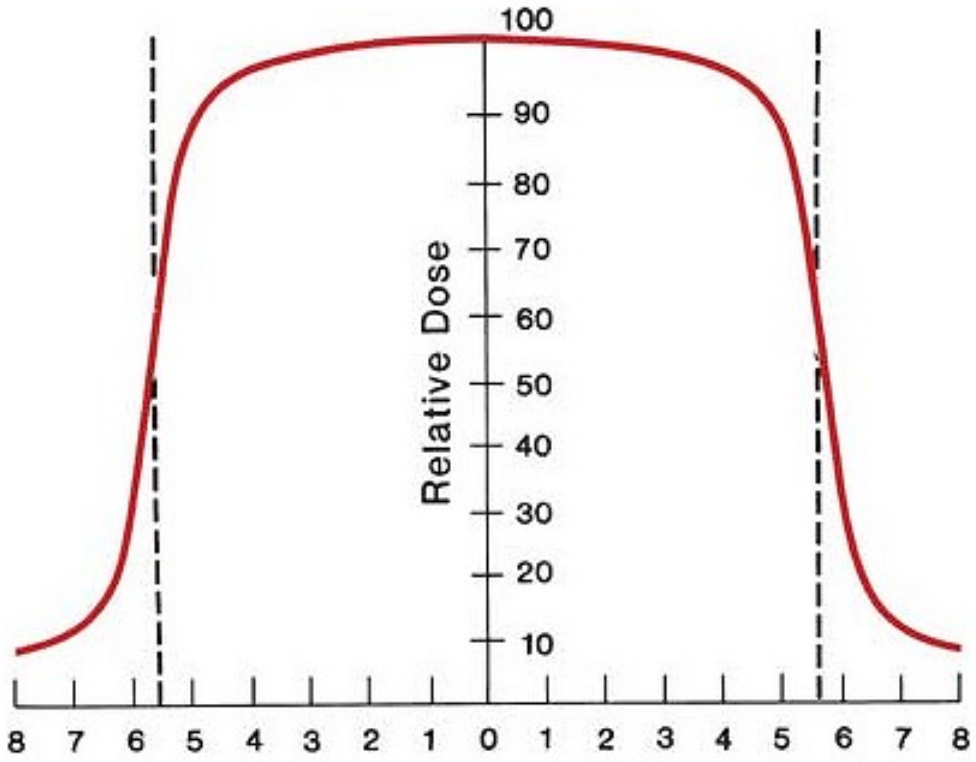

Figure 2.7: Beam profile for a broad beam size. Penumbra is from 20% to 80% with 80% of the field size showing a high dose region. (Figure from Ref.[34]).

The radiation field size ensures that the uniform dose is measured in the beam profile and is defined as the distance between the 50% dose points. The dose distribution across the photon beams axis is shown in Figure 2.7. Due to its dependence on the distance from the source, it is measured at 100 cm from the source. During commissioning, beam profiles, field output factors, and PDDs measured at different beam sizes are modeled into the treatment planning system. Therefore, the planning system uses this information for treatment time calculations.

Bremsstrahlung interactions produce more photons at the center of the beam. Due to higher energy at the center, megavoltage beams experience more filtration. The variation of dose near the umbra region is evaluated. To minimize higher doses at the center of the target, flattening filters are used in radiotherapy. They not only produce a uniform beam but impact the energy spectrum.

The concepts of field flatness and symmetry are used to evaluate the flattening filters. Beam flatness is expressed as the difference between the maximum and

the minimum dose within the 80 region on either side of the beam central axis divided by their sum [34]:

$$F = \frac{D_{max} - D_{min}}{D_{max} + D_{min}} * 100 \tag{2.5}$$

Where D_{max} and D_{min} are the maximum and minimum doses within the 80% region, respectively, the megavoltage (MV) photon beam must be properly aligned with the flattening filter. Symmetry is a measure of how symmetric the beam is on both left and right sides within the umbra. It is determined by comparing the area on the left to the area on the right divide by the sum of these two areas [34, 36]:

$$S = \frac{A_L - A_R}{A_L + A_R} * 100 \tag{2.6}$$

Where A_L and A_R are the areas on the left and right sides of the beam profile within the 80% region.

2.4.3 Field output factors

Photon scatter within the linear accelerator head is divided into two components: the collimator scatter and the phantom scatter [26].Output factors account for scattering from the Linac head and the phantom. They are required to model all the higher energy beams in the treatment planning systems. Output factors are also known as the total scatter correction factors. The detector readings of any field size are normalized to the reference field size of 10 x 10 cm^2 at a reference depth of 10 cm in water. The total scatter correction factor accounts for the effect of field size scatter to the point of interest.

Field output factors characterize how the dose varies with field size to a point in a phantom. This is a field size and phantom scatter-dependent factor. However, in a small beam size, the field output correction factor is included in the ratio of the chamber response [20]:

$$\Omega^{fclin,fmsr}_{Qclin,Qmsr} = \left(\frac{M^{fclin}_{Qclin}}{M^{fmsr}_{Qmsr}} \right) k^{fclin,fmsr}_{Qclin,Qmsr} \tag{2.7}$$

Where $\Omega_{Qclin,Qmsr}^{fclin,fmsr}$ is the field output factor which converts the dose from the reference field to that of the clinical field, M_{Qclin}^{fclin} is the detector response for the clinical field size, M_{Qmsr}^{fmsr} is the chamber reading for the machine-specific reference field, $Qmsr$ and $Qclin$ corrects for the differences in energy for both the machine-specific reference field (fmsr) and clinical field size ($fclin$), respectively, $k_{Qclin,Qmsr}^{fclin,fmsr}$ is the detector-specific output correction factor that accounts for the differences in smaller field sizes from a clinical reference field size. The $fmsr$ is the machine-specific reference field for different radiotherapy machines such as CyberKnife, Gamma-knife, TomoTherapy, Radio-surgical collimators, etc.

The detector-specific output correction factors are given as the function of the square field size for the different chambers in TRS 483 [20]. The expression for the detector-specific output correction factor is given by the following equation [9].

$$k_{Qclin,Qmsr}^{fclin,fmsr} = \left(\frac{D_{Qclin}^{fclin}/D_{Qmsr}^{fmsr}}{M_{Qclin}^{fclin}/M_{Qmsr}^{fmsr}} \right) \tag{2.8}$$

Where $D_{Qclin}^{fclin}/D_{Qmsr}^{fmsr}$ and $M_{Qclin}^{fclin}/M_{Qclin}^{fclin}$ is the ratio of doses and detector readings in clinical fields and msr, respectively.

Previous studies have shown large discrepancies in field output factors measured with various types of detectors in small fields [41, 42, 43]. For the reason that volumetric detectors tend to underestimate the field output factors when the field size is smaller compared to the chamber effective volume due to the volume averaging effect [45, 46].

2.5 Dose calculation algorithms

Dose computation from a photon beam to the point of interest in a material is determined by using a computer treatment planning system (TPS). Dose calculation algorithms are mathematical models used in radiation therapy treatment planning systems to predict the dose distribution in a patient's body. This is performed based on the characteristics of the radiation beam and the anatomy of the patient [34].

In this study a mordern TPS, Monaco, was used in the calculation of dose in 3D volumes. The system uses the following algorithms to calculate the dose to a point in a patient:

- Pencil beam algorithm
- Collapsed cone convolution
- Monte Carlo simulation

Tissue heterogeneity corrections are handled quite differently by these algorithms. Some algorithms are correction based while others are model-based [34]

2.5.1 Pencil beam convolution algorithm

In the pencil beam algorithm, heterogeneity along a one-dimensional path length is considered, and no density scaling non-homogeneity corrections outside the beam path is considered. The change in electron transport in the lateral direction is not taken into account; hence the dose estimation in lung tissues is inaccurate [47].

2.5.2 Collapsed cone convolution algorithm

In collapsed cone convolution, in-homogeneity corrections are applied in three dimensions. Therefore, the changes along tissue that the radiation beam is going through and the changes in lateral electron transport are modeled [34]. However, the heterogeneity correction is applied on the assumption that the dose kernels are based on the density of water for any medium [34]. The dose is then summed from the primary beam, head scatter and electron contamination components [48].

2.5.3 Monte Carlo simulation

The Monte Carlo algorithm models the individual particle tracks from a Linac's head to the patient's volume. Direct Monte Carlo is applied in situations where the transient charged particle equilibrium does not exist [34].

Each particle is tracked in a particular voxel to produce different cross sections for both electrons and photons [47]. Both the Monte Carlo and collapsed

cone account for the change in electron density. However, the Monte Carlo algorithm modeled the radiation transport in tissue more accurately [47]. This is regarded as a gold standard for photon dose calculations in radiotherapy.

2.6 Beam scanning detectors

Various types of detectors respond differently in small photon fields; the choice of a detector is critical.The volume-averaging effect of a detector guides the choice. Hence multiple detectors such as diodes, diamond, organic scintillators, and films are recommended for measurement of the small field output factors [43]. Small volume detectors are mostly used for beam profiles and PDD measurements, while diodes are recommended to measure sharp penumbra.

2.6.1 Small volume detectors

Ionization chambers are most frequently used for absolute dose measurements. All the factors that affect the detector response in point dose measurements are well known. As the steep dose gradient characterizes narrow photon fields, therefore, the use of the ionization chamber still remains a challenge. However, small-volume detectors are still very useful in small photon field measurements.

This work aims to compare the output factors measured with small-volume ionization chambers to the other special 2-D detectors such as films and EPID.

2.6.1.1 Ionization chambers

An ionization chamber is a gas-filled detector with two electrodes, anode and cathode. Incident radiation ionizes the gas molecules within a sensitive volume to form positive and negatives ions. Positive ions move to the cathode(-) while negative ions move to the anode(+). A bias voltage then collects ion pairs to produce a measurable current.

Depending on their specific application, ionization chambers are manufactured in different shapes and sizes. A pinpoint ion chamber with a volume of 0.015 cm^3 might be too large for field sizes smaller than 1 x 1 cm^2. The smallest field size that the pinpoint chamber can measure is 2 x 2 cm^2. The PTW 0.125 cc Semiflex 3-D ion chamber has a volume-averaging effect [44].

Scanning speed is important when using a 3-D semiflex ion chamber with a sensitive volume of a PTW Pinpoint 0.07 cc to measure profiles and penumbra due to its collection efficiency. Smaller volume detectors require low scan speed. However, their response is not affected by the scanning direction [44].

2.6.1.2 Solid state detectors

Silicon diodes are the most commonly used solid-state detectors in radiation therapy. They have a relatively small volume compared to the gas-filled detector to provide the sharpest penumbra. This is due to the density differences and higher atomic number of silicon compared to that of gas.

Silicon diodes are semiconductor detectors based on the principle of the conduction band and valance band with a relatively large energy gap between the two bands. If silicon is doped with impurities such as phosphorus with an extra electron; the diode is known to be an n-type with electrons as the majority carriers. In p-type semiconductors, silicon is doped with boron and holes are the majority carriers.

The schematic representation of a p-n junction of the diode detector is shown in Figure 2.8 below [29]. The p-type and n-type semiconductors are put together to create a depletion zone in the middle. Incident radiation interacts through the depletion zone to create electron-hole pairs. Electrons move towards the n-type while holes move in the direction of the p-type. The signal is detected due to the movement of charges. As a result, the measured current is directly proportional to the energy deposited by the incident radiation [29].

Diodes are designed for different energy ranges. A different response is obtained with various photon energies. The main limitations of diode detectors are temperature dependence, energy dependence, and the directional dependence [29]. Hence they are not used mostly in dosimetry.

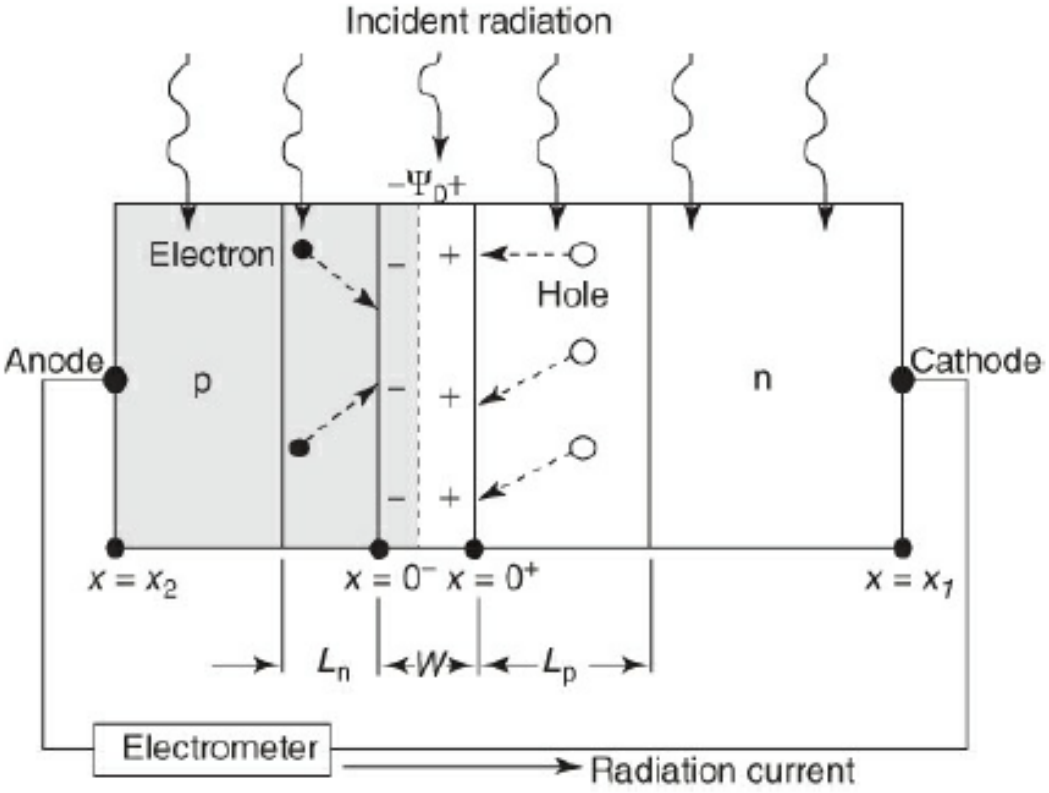

Figure 2.8: A p-n junction of the diode radiation detector. Incident radiation creates electron-hole pairs in the semiconductor detector [29].

2.7 Radiochromic film

Films, in general, are used in radiotherapy departments for quality assurance purposes. They are used to determine the actual field size before performing any measurements. There are two types of films: radiographic and radiochromic [26]. Radiographic films have been used in radiotherapy mostly to measure beam flatness and symmetry, light/radiation field congruence, star shot test, picket fence test as well as a two-dimensional (2-D) dosimeter due to their superior spatial resolution [49].Films can be used to obtain the required accuracy in absorbed dose measurements [50].They are optional in beam profile measurements to eliminate the volume averaging effects.

However,radiographic films are energy-dependent; they produce a different response for different beam energies and reach a saturation point in terms of dose [51].The energy-dependence of radiographic films limit their use in dosimetric applications [49]. In contrast, radiochromic films (RCF) are insensitive to visible light but more sensitive to red light, have no silver halide crystals,

and therefore no need for chemical processing to convert silver ions to silver atoms [52].

2.7.1 Overview of RCF in small fields

As discussed in section 2.2.3, the size of the detector with reference to the field size can lead to volume averaging effect. Therefore, unsuitable detector for relative dose measurements results in up to 60% difference in field output factors [53].

RCF has a great potential for small field measurements due to its high spatial resolution [21]. However, a crucial literature summary on the work done by other investigators in the use of film for the dosimetric measurement of small fields is not provided in the new IAEA TRS-483 protocol [9].

In the study by Gonzalez-Lopez et al(2015), film was used as an alternative for small fields relative dosimetry [54]. The performance of RCF was evaluated against the two volumetric detectors, 31006 (PTW, Freiburg, Germany) Pinpoint (0.015 cm^3), and 31010 Semiflex thimble-type (0.125 cm^3).

A good agreement was obtained for the output factors measured with the three detectors for field sizes equal to or greater than 2 x 2 cm^2 [54]. Also, a good agreement was observed between the RCF measured dose profiles and calculated Monte Carlo profiles for 1 x 1 cm^2 field size [54].

2.7.2 The layout of radiochromic films

Gafchromic film is the most commonly used radiochromic film in radiation therapy for measuring the radiation dose. The structure of Gafchromic EBT3 film consists of two pieces of matte-surface clear polyester base, 125 μm and an inner active layer of approximately 30 μm thick [26, 55]. The function of the polymer layers on top and below the active layer is to keep the film intact. The structure of a radiochromic EBT3 film is shown in Figure 2.9 below. A layer of radiation sensitive organic micro-crystal is sandwiched between the two polyester layers (top and base substrates) with a transparent coating.

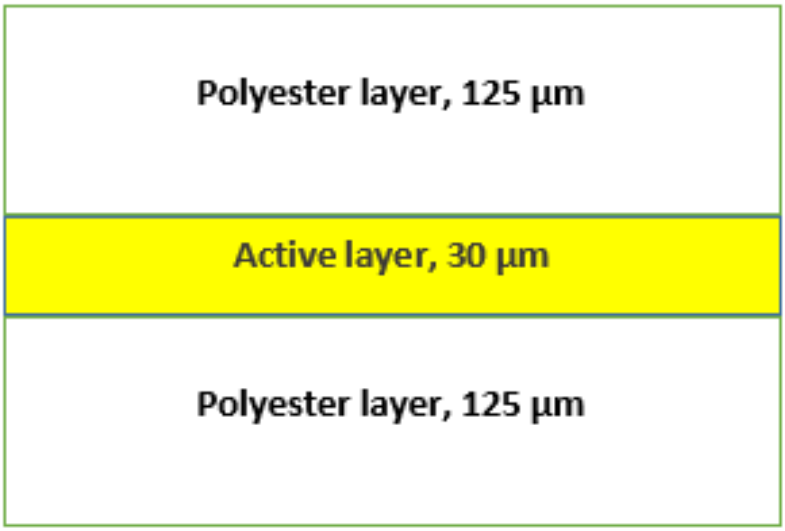

Figure 2.9: Gafchromic EBT3 film configuration showing an active layer sandwiched between the two clear polyester film substrates (taken from Ref.[56]).

EBT3 film is the latest to be produced by GafChromic. EBT2 films had two active layers which led to many issues regarding resolution.

2.7.3 Measurement principle of a radiochromic film

When radiochromic film is exposed to ionizing radiation, the dye molecules are ionized resulting in a change in color. This change in color corresponds to the amount of absorbed dose. Incident radiation interact with the radiation-sensitive layer containing a dye precursor which is sandwiched between the two polyesters as shown in Figure 2.9 [56].

Monomers are induced that creates polymer chains [57]. The chemical process is illustrated in Figure 2.10. Light transmission is measured from the irradiated film. These transmission measurements are then used to determine the optical density to obtain a signal information [29]. The change in both polymerization and opacity is directly related to the amount of radiation absorbed by the film.This causes a change in the film's optical density which is related to the absorbed dose by the film [57]. Therefore, the signal can be measured from the scanned film with a flatbed or Vidar scanners

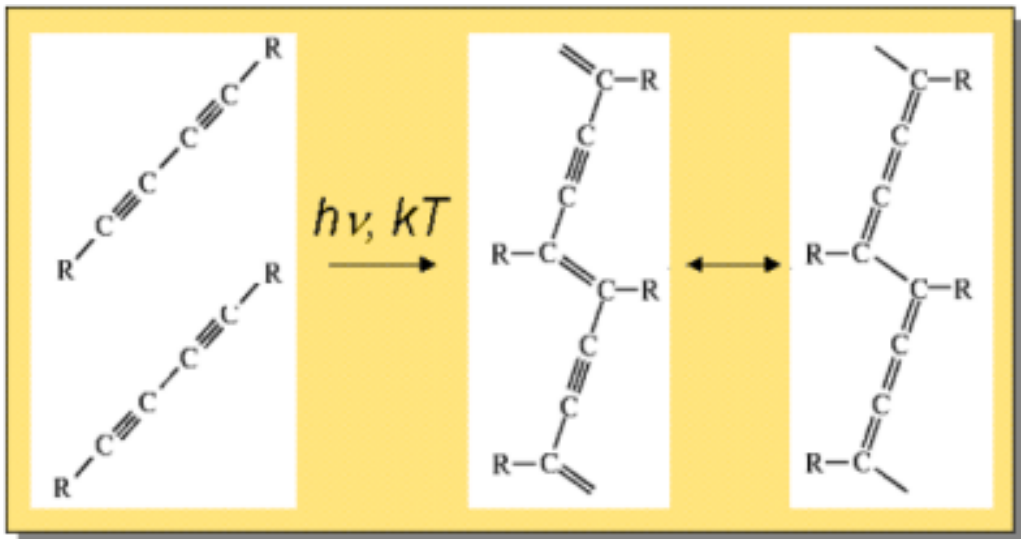

Figure 2.10: The core of radiochromic film technology shows the active component of lithium pentacosa-10,12-diynoate (LiPCDA). Polymerization induced by incident radiation can be seen in the film (taken from Ref.[57]).

Figure 2.11 shows the electron microscopy image of the active crystal. The electron microscopy crystal image shown by the figure below provides information about the crystal structure of the film at the atomic level, including the arrangement of atoms and the orientation of crystal planes.

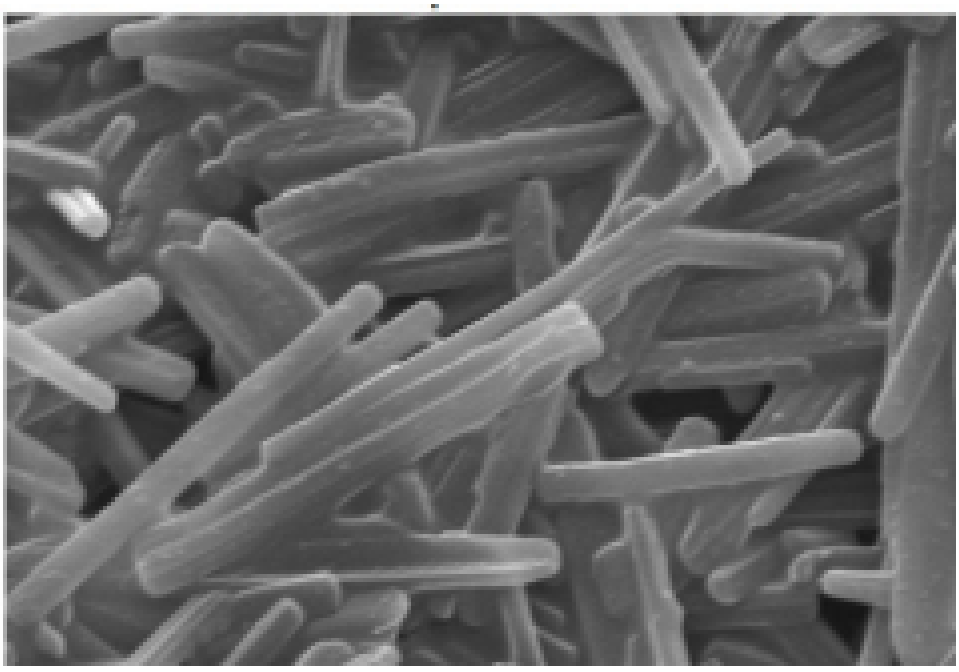

Figure 2.11: Electron microscopy crystal of the active material. This is a radiosensitive component of the EBT-type film. Fluid flow during the coating process orientate the rods shown in the photograph parallel to the coating direction (taken from Ref.[57]).

The orientation of the active material crystal is parallel to the coating direction. This is caused by the fluid flow during the coating process. The active material crystals become light polarizers after irradiation. This polarization creates the directional dependence of the film.

The film thus produces different results when measurements are performed in portraits versus the landscape orientation. As recommended, pixel value measurements must be performed at the centre of the film to minimize the lateral artifacts[29].

2.7.4 Dosimetry measurements with radiochromic film

Gafchromic EBT3 films have been assessed to have a high spatial resolution, and good energy response with a low volume averaging effect; low dose gradient areas can be accurately resolved [40, 21, 26]. These types of films are exposed to a higher radiation dose ranging from 0.2 Gy up to 10 Gy [58], with fitting parameters that are acceptable to a maximum dose of 40 Gy[55]. However, each new batch of the film must be calibrated due to batch-to-batch variation.

The following parameters must be taken into consideration with film dosimetry: calibration curves to be accurately produced, light channel to be properly selected, and consistency in the readout period. The results are not obtained immediately and the response changes depending on the amount of time[29]. Film protocol must be properly set for dose measurements, IMRT and VMAT verification.

Table 2.1 below shows the specifications of GafChromic EBT3 film from the manufacture's website [56]. GafChromic EBT3 film has several specifications, including: the active area of 20 cm x 25 cm, the sensitivity range of 0.1 Gy to 20 Gy which makes it suitable for a wide range of radiation doses, and the spatial resolution of 30 micrometer (μm).

Table 2.1: Specifications of radiochromic (GAFChromic EBT3) film

Property	GAFChromic EBT3 film
Configuration	Active layer of $30\mu m$ is sandwiched between $125\mu m$ polyester substrates
Size	8" x 10"
Dose range	0.1 to 20 Gy
Energy dependence	$< 5\%$ difference in net optical density when exposed up to 18 MeV
Dose fractionation response	$< 5\%$ difference in net optical density for a single 25 Gy dose
Dose rate response	$< 5\%$ difference in net optical density at a rate of 3.4 Gy/min
Stability in light	$< 5 \times 10^{-3}$ change in optical density per 1000 lux-day
Stability in dark	$< 5 \times 10^{-4}$ change in optical density per day at 23
Uniformity	Better than $\pm$ 3% in sensitometric response and better than $\pm$ 2% with FilmProQA

With radiochromic films, the amount of color change or darkening is proportional to the amount of radiation dose delivered; hence the optical density (OD) versus radiation dose curve is linear. Film dosimetry is based on intensity measurements in the form of pixel values which represents the darkness of the image. If the film is too dark, the optical density is very high, which leads to lower pixel values. Therefore, the darker the film, the lesser the measured intensity.

This is a much better film for quantitative measurements in radiotherapy dosimetry; no need for processing. The signal is obtained from a transmission measurement. For the same change in dose, EBT Gafchromic film gives a bigger difference in OD. This provides a better Hurter-Driffied (H-D) curve, which is a typical dose-response curve [59].

Previous studies evaluated parameters such as dose rate response, energy dependence, and dose uniformity of the Gafchromic EBT3 film [26]. The effects of beam energy, and dose rate on the EBT3 films have been characterized and found to be insignificant [60].

2.7.5 Clinical application of EBT3 films

Small fields are more conformal to the target with a very steep dose gradient compared to large fields [26]. The requirements for precision and accuracy are high in small photon fields. The use of a film may minimize errors due to non-tissue equivalence and positional uncertainty in output factor measurements [25].

The first application of Gafchromic EBT films in small photon field dosimetry was in the commissioning of intensity-modulated radiation therapy (IMRT) and volumetric-modulated arc therapy (VMAT) as well as in the dose verification of IMRT and stereotactic treatment plans [61]. The relatively advanced techniques, such as IMRT and VMAT, use small photon fields with steep dose gradients [62]. In other clinics, films are used for invivo dosimetry in total body irradiation (TBI).

A relatively new radiochromic film (Gafcromic EBT -XD) was tested against the EBT3 films for high-dose treatment verification and the study found EBT-XD to be more accurate in terms of measuring the dose distributions for a typical SRS-treatment than EBT3 [63]. EBT-XD are recommended for high dose measurements greater than 10 Gy. EBT3 films are designed for absolute dose measurements of less than 10 Gy in high energy photon beams.

Films with commercially available software were used for patient-specific dose verification for IMRT and VMAT treatment plans to evaluate the agreement between the planned and measured dose distribution. This study found an improvement in the results of gamma passing criteria between the measured dose and the calculated treatment planning dose (calculated maps) [64].

A study by Micke et. al. 2011 used Gafchromic (EBT) film for dose verification in IMRT plans [65]. The need for a consistent procedure during calibration

and measurement for high precession and accuracy was pointed out. In addition, the importance of a high spatial resolution in high-dose gradient regions and some clinical dosimetry challenges related to scanning was indicated [65].

This study by Micke et. al. proved that using Gafchromic(EBT) film is feasible for dose delivery verification in small photon fields of IMRT and SRS treatment plans [65]. Gafchromic EBT3 films are proven to be dose rate independent; no corrections are needed to characterize the high dose rate beam such as flattening filter-free (FFF). It has been reported that the EBT3 film response is not affected by changing photon energy [40].

Any orientation can be used during exposure with no angular dependence.A big difference in output factor measurements between the EBT2 film and volumetric detectors in field sizes less than 2 cm x 2 cm^2 was reported [54]. The report of AAPM TG-101 recommended the use of an appropriate dosimeter to overcome the challenges of the volumetric detector in aligning the detector at the centre of the field [26].

2.8 Electronic portal imaging device

Electronic portal imaging device (EPID) have replaced the use of conventional film cassettes for treatment field verification. Contrary to kilo-voltage (kV) imaging, mega-voltage (MV) energies are used to create portal images with poor contrast. Target position relative to the CT scanner's anatomical information and beam dimensions are shown in the portal images. Therefore, higher photon energies produced images generated by the flat panel detectors are required to verify patient set-up before the radiotherapy treatment.

Its advantage over a film cassette is in detecting and correcting random and systematic errors [66]. Therefore, digital image enhancement for better image quality has made the EPID to be a preferred technology for imaging compared to film. The most commonly used flat panel EPID with the Elekta system is the solid state detector based on amorphous silicon (a-Si) [67]. In this study, EPID will be used for small field output factor measurements only to compare with film measurements.

2.8.1 Operating principle of (a-Si) EPID

The a-Si EPID consists of a copper layer and a phosphor screen with photodiode array [68]. Incident radiation is converted into a visible light by a-Si scintillator material. An array of photodiodes within the a-Si panel then detects this visible photon. A copper (Cu) layer in the a-Si EPID absorbs low energy scattered radiation from the patient [69].

The detection area of an Elekta EPID is 41 x 41 cm^2 with 1024 x 1024 pixels (matrix size) and a spatial resolution of 0.25 mm mounted at a fixed distance of 160 cm from the source [70].

2.8.2 GLAaS algorithm

EPIQA software uses GLAaS algorithm to convert images measured by EPID into dose map. Pixel values from a-Si detectors are transformed into matrices of absorbed dose to water at any given depth [71]. Generally, EPID images are converted into absorbed dose in water at d_{max}. However, in this work the algorithm was configure to transform images to dose at a reference depth of 10 cm.

The a-Si detectors are exposed directly to radiation dose with no build-up or phantom material in between the source and the flat panel [71]. The a-Si detectors produce a linear dose response; therefore GlAaS algorithm uses linear regression parameters to account for differences between the primary dose and MLC-transmitted radiation on a pixel-by-pixel basis [72]. This algorithm was initially developed for IMRT pre-treatment verification, and later applied in dosimetric verification of VMAT treatments [73]. In this study, it is evaluated in small fields output factor measurements.

The differences between the primary dose and the transmitted radiation through the MLC are modeled by using the following expression[73]:

$$d_i = \left(\sum_{s=1}^{N} m_p * r_{i,s} + q_{p,s} \right) + \left(m_t R_i - \sum_{s=1}^{N} m_t r_{i,s} + q_{t,s} \right) \tag{2.9}$$

Where d_i is the total dose in the i-th pixel, m_p and m_t are the slopes for the primary and transmitted radiation respectively, q_p and q_t are the intercepts

for the field size of primary and transmitted beam, r_i is the reading from the primary radiation beam, R is the reading from the PV cassette, N is the number of segments, and s is the segment point.

2.8.3 Special applications of EPID

EPID is applied in geometric pre-treatment verification and for daily treatment set-up. Verification of the treatment fields with respect to patient positioning has become a standard procedure in modern radiotherapy.

Dosimetric verification methods with EPID have been introduced in the past. Pre-treatment verification and dosimetric verification of IMRT and VMAT plans with (EPID) have now become a standard practice in most radiation therapy centers [69].

EPID is attached to almost all the modern linear accelerators. This is due to an easy set-up and two-dimensional (2-D) images that are provided in a digital format [69].

The application of EPID in radiation therapy has been extended to dose verification in small photon fields treatment plans such as IMRT and VMAT. Even though EPID was initially developed for patient set-up verification purposes, it is currently used as a 2-D dosimeter [74].

Chapter 3

Methodology

3.1 Materials and Method

In this study, all the measurements were carried at Charlotte Maxeke Johannesburg Academic Hospital CMJAH on an Elekta HD Versa linear accelerator (linac). Commercially available radiochromic films, GafChromic EBT3 type from Ashland Inc., Wayne, NJ, USA were used in this study. The film response to radiation was measured by a calibrated flatbed Epson 11000 XL scanner.

A calibrated cylindrical ionization chamber with a cavity volume of 0.6 cm^3 and the PTW UNIDOS E electrometer from PTW, Freiburg,Germany was used for the output calibration. In addition to film measurements, both EPID and treatment planning data were acquired as reference measurements and additional measurements.

In order to expose the radiochromic film to a known dose, the machine output was measured with a calibrated 0.6 cc farmer-type chamber in a solid water phantom under reference conditions. Film was irradiated to a range of known doses to establish the calibration curves for each photon energy. This was performed in preparation for dosimetry measurements.

Beam profiles were measured with various detectors for each field and compared with the calculated treatment planning profiles. Dose profiles were required to determine the radiation field size in terms of full width at half maximum (FWHM) prior to field output factor measurements.

3.1.1 Electron density verification

The monitor unit (MU) calculations from the treatment planning systems are performed based on the number of electrons per volume (electron density). Electron density determines the attenuating properties of the radiation beam inside the phantom.

The most common mega-voltage (MV) photon interaction with matter is through compton scattering. Higher photon energies interact at this region and the probability of this interaction depends entirely on the material's electron density and composition. Hence there is a need for the verification of electron density of any material. The electron density of the material is determined by the following equation [34]:

$$\rho_e = \rho_m N_A \left(\frac{Z}{A}\right) \tag{3.1}$$

Where ρ_m is the mass density of the material in gram per cc(g/cc), N_A is the Avogadro's number in atoms per mole, Z is the atomic number, and A is the mass number in grams per mole.

For accurate dosimetry in radiotherapy and also for the treatment planning system (TPS)to account for tissue heterogeneity, the electron density must be verified from the Hounsfield units (HU) provided by the computed tomography (CT).

In practice the CT datasets image gray scale is represented by HU; from air, water and bone given by -1000, 0, and 1000 respectively. Also represented in the grayscale, are CT numbers for very high electron density materials (e.g. prosthesis). The relationship between CT numbers assigned by the CT scanner and the electron densities provided by the TPS is linear in all the structures, as shown in Figure 3.2.

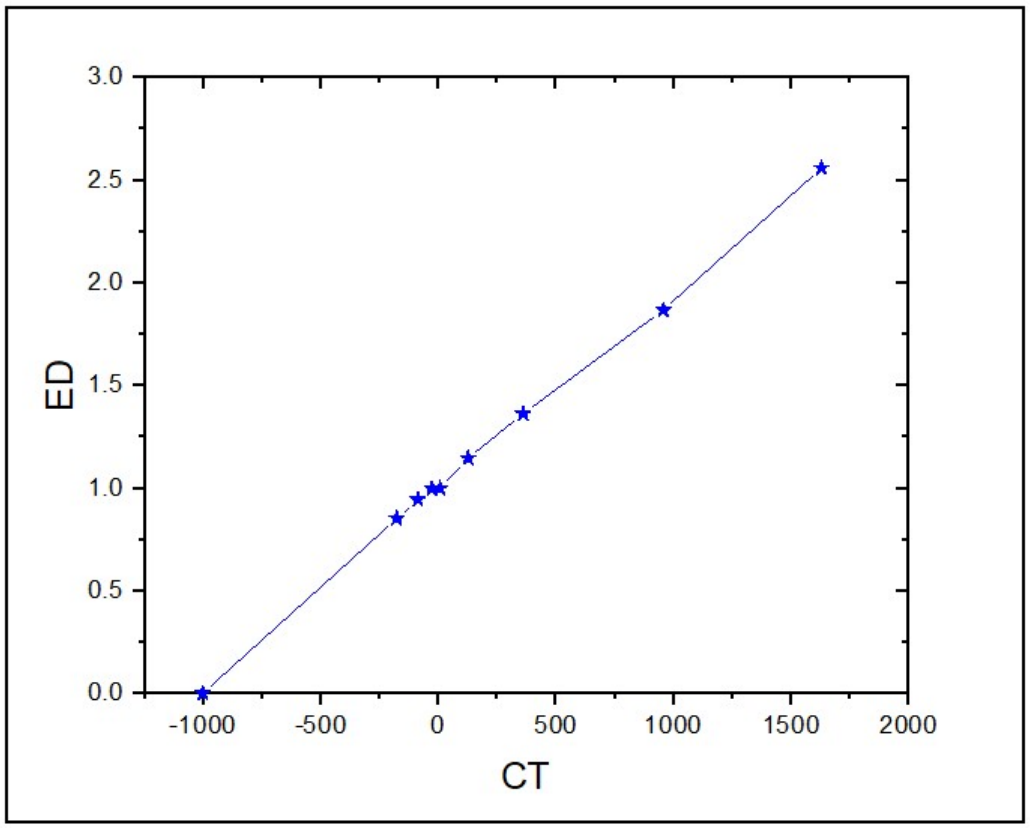

Figure 3.1: CT number (HU) to electron density conversion curve produced by the Monaco TPS.

At high density material, this curve does not follow a linear trend. Therefore, computed tomography (CT) yields incorrect CT to density conversion which results in dosimetry not being accurate.

3.1.1.1 Data acquisition for the TPS

In this study, a solid water phantom was used due to its more convenience in film dosimetry measurements than liquid water. The solid water phantom used for all the film measurements is shown in Figure 3.2 below. The images of the solid water phantom with dimensions: 30 cm x 30 cm x 30 cm were acquired using a Siemens CT scanner and transferred to Monaco TPS. Contouring of the CT images was performed using Monaco contouring tools.

Figure 3.2: Photograph of a solid water phantom placed in a CT scanner for treatment planning and monitor unit calculation.

Monaco software has the option to force different structures of the scanned CT images into one. Therefore, electron densities were assigned to the contoured CT images and forced to be equal to one. Hounsfield unit (HU) of water is equivalent to the electron density of 1 g/cm^3. The electron density of the phantom was verified in the TPS through CT numbers assigned by the CT scanner. The electron density was verified to be equivalent to that of liquid water using the available calibration curves in the TPS . This is necessary for the accuracy of dosimetric calculation with a treatment planning computer.

3.1.2 Film preparation for dosimetry

The sensitivity of the film depends on its orientation during scanning. For consistency with a scanning orientation and calibration purposes, Gafchromic EBT3 films were cut into a rectangular shape of 2 x 25 cm^2 using a film cutter

and marked for correct orientation. Figure 3.3 below shows the film cutter used for cutting films into rectangular or square pieces.

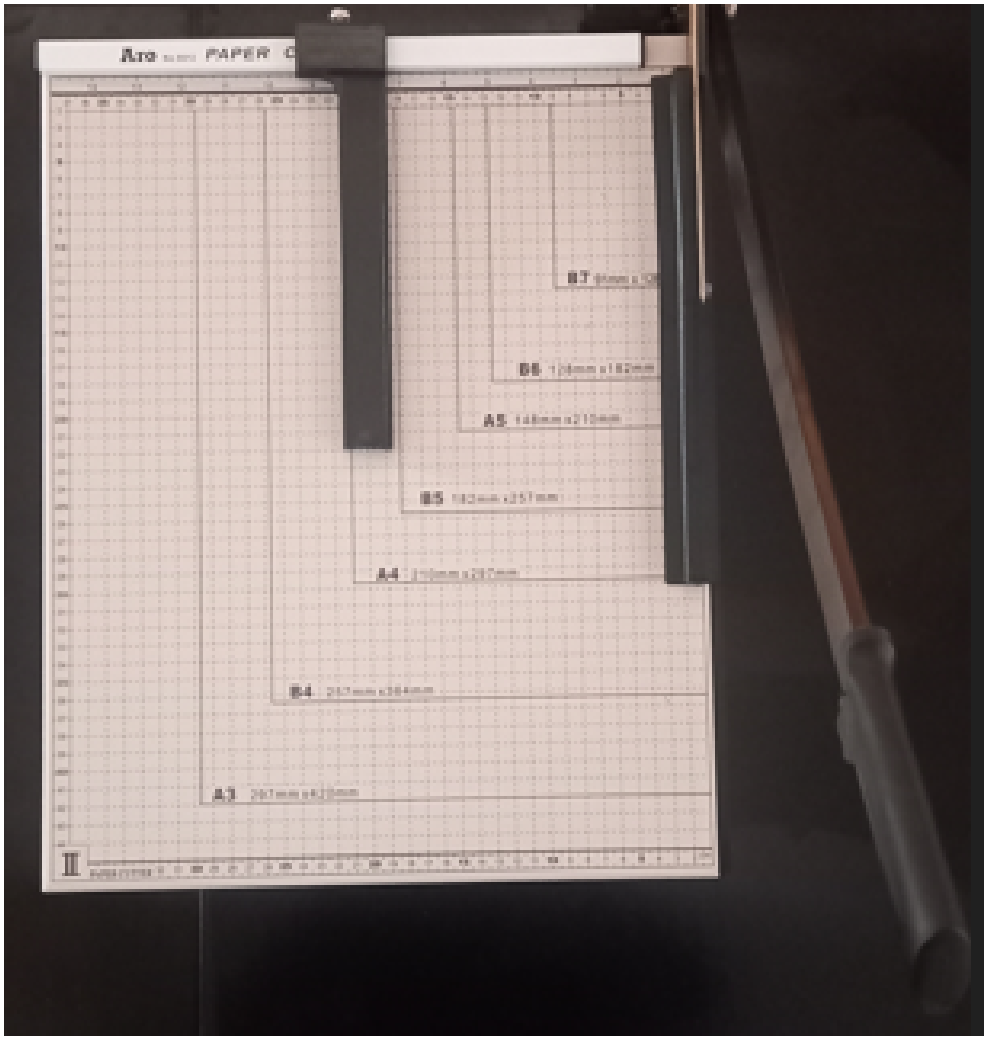

Figure 3.3: Photograph of a guillotine cutter used during film preparation.

The known absorbed dose in the range: 0.5 Gy to 25.0 Gy was measured. To minimize measurement uncertainties due to film handling, gloves and tweezers were used when cutting EBT3 films into smaller pieces. Films were carefully handled from the side, not in the middle to obtain the correct signal.

All the small pieces of film were marked as per the dose that will be given to an individual piece, as shown in Figure 3.4 below with one strip left unexposed. One piece of film was left unexposed to radiation for background measurements.

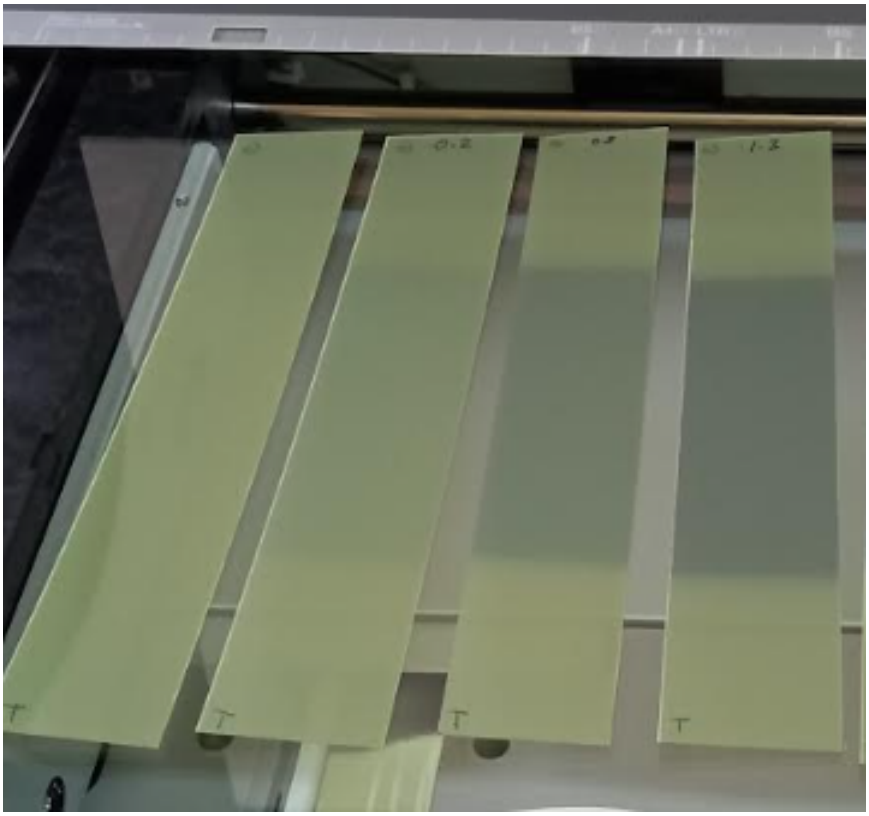

Figure 3.4: Photographs of films cut into small strips and marked according to their exposed doses for calibration purposes.

Film dosimetry protocols recommend scanning of all film pieces prior to irradiation using all three color channels (red, green, and blue) for background correction [42].

3.2 Linac output measurements

Cylindrical ionization chambers with cavity volume of 0.6 cm^3 and are the gold standard for absolute dosimetry measurements under reference conditions. To use film in absolute dose measurements, proper calibration against the ionization chamber is necessary for absolute output measurements. Thus, film was calibrated against the ionization chamber prior to output measurements.

3.2.1 Elekta Versa HD output

Linac output (cGy/MU) was measured with a PTW farmer-type ionization chamber with a collection volume of 0.6 cc in a solid water phantom to ensure that the film was exposed to a known dose.

Chamber measurements were performed at Charlotte Maxeke Johannesburg Academic Hospital (CMJAH) on an Elekta HD Versa linear accelerator. The Solid water phantom used allowed for the insertion of a 0.6 cm^3 cylindrical ionization chamber. The picture of the ionization chamber used for output calibration is shown in Figure 3.5.

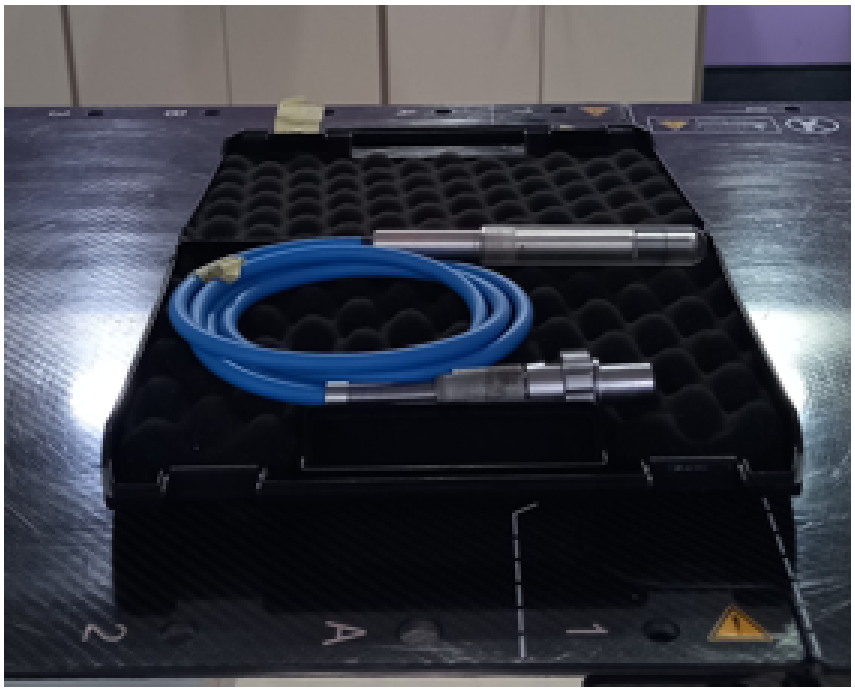

Figure 3.5: Photograph of the calibrated 0.6 cm^3 Farmer type ionization chamber.

The electrometer used to convert the measured charges to dose is shown in Figure 3.6 below. The PTW UNIDOS E which is compatible with the variety of PTW detectors was used for Linac output measurements. The detector generates a signal which is proportional to the energy deposited by the incident radiation is measured and converted to dose by the electrometer using a calibration factor.

Figure 3.6: Photograph of a PTW UNIDOS E (electrometer).

Sufficient scatter and build-up material was used throughout the measurements. The detector was aligned to the beam's central axis. Dosimetry measurements were performed under the following reference conditions(illustrated by the labeled Figure 3.7 below): 90 cm source-surface distance (SSD), 10 x 10 cm^2 and a depth of 10 cm.

The effective point of measurement of the detector was set to be at the center of air cavity. The geometry for linac output measurements is shown in Figure 3.7, the 0.6 cm^3 ionization chamber was placed at a distance of 100 cm from the radiation source. The point of interest was kept at isocenter during the measurements. This is known as the source-axis distance (SAD) technique; the distance from the source to the chamber's effective point of measurement is kept to 100 cm.

Measurements were performed for three photon energies: 6MV FFF and 6MV FF, and 10MV FF beams. The tissue-phantom ratio (TPR) measured at 20 cm and 10 cm depths was used to quantify the two energy beams. Dosimeter reading from the electrometer was recorded after 100 monitor unit (MU) was delivered. All readings were repeated three times to obtain the average value. The absorbed dose to water was calculated as per TRS 398 formalism [33]:

$$D_{water} = \bar{M} N_D k_Q \tag{3.2}$$

Where $\bar{M}$ is the corrected chamber response, N_D is the chamber calibration factor applied to convert charge reading to dose, and k_Q is the beam quality conversion factor. The calibration factor from the Co-60 beam is converted to the linac energy.

All the necessary correction factors such as air density, ion recombination, electrometer and bias polarity, were applied to the chamber reading. The dose rate in Gy/100 MU was obtained from the chamber measurements.

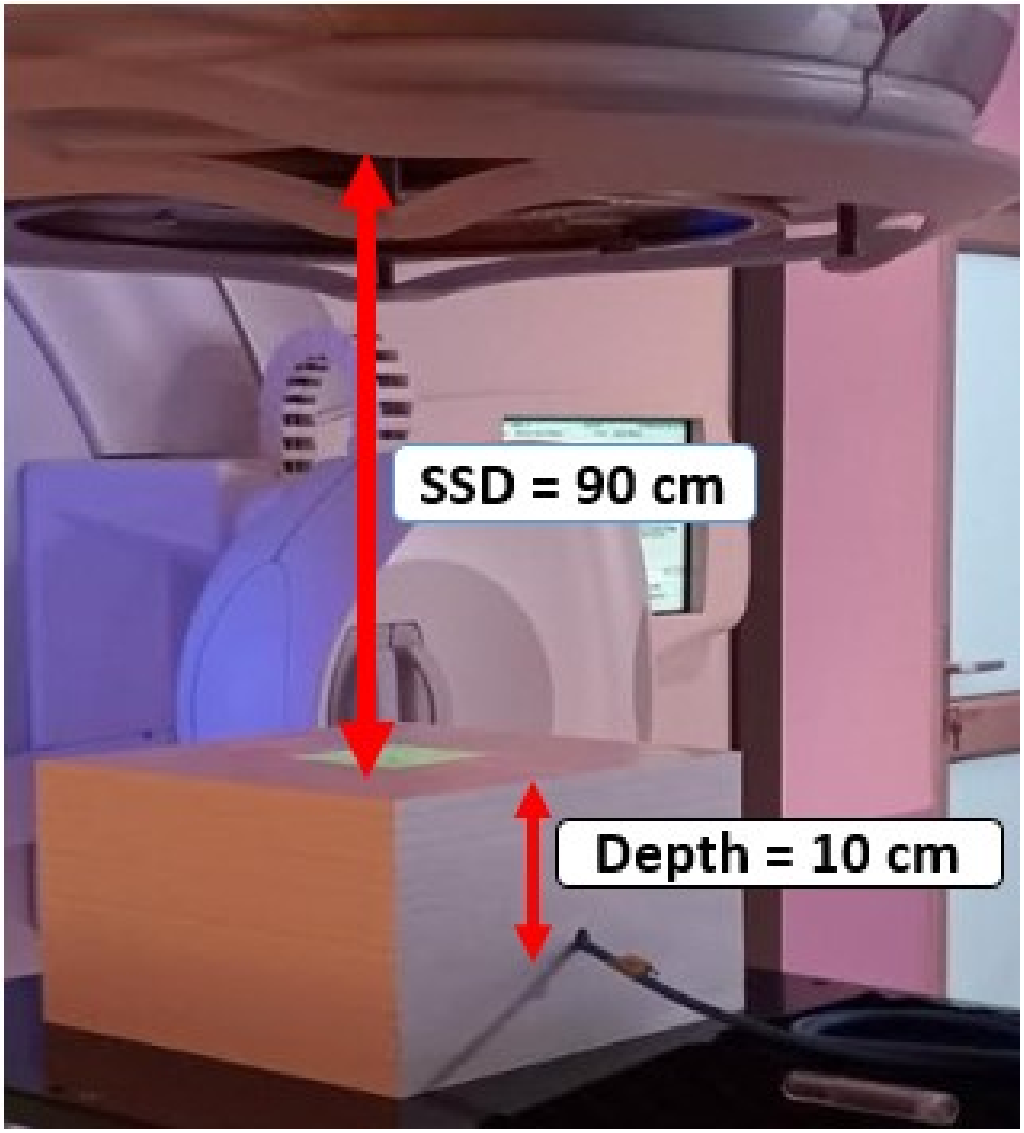

Figure 3.7: Photograph of the set-up for machine output measurements.

3.2.2 Film calibration

Each piece of film was placed at a depth of 10 cm with sufficient scatter material underneath. The light field was used to align each piece of film at the beam's central axis. Gantry and target side were marked on each piece of film. Monitor unit delivered for each film irradiation was calculated from the chamber measurements.

3.2.2.1 Film irradiation

For calibration, films were cut into fifteen strips of 2 x 25 cm^2 and placed in a solid water phantom at 100 cm from source to axis distance (SAD). Films were fixed with adhesive tapes, placed at the corner of each piece of film to hold the film tightly on the phantom during irradiation.

Each film piece was exposed to 6MV FFF, 6MV FF and 10MV FF photon beams with a dose ranging from 0.5 Gy to 25.0 Gy. The maximum dose of 25 Gy was delivered to one of the strips to test the response of the film in high doses. A field size of 10 x 10 cm^2 was used during the calibration process.

For each strip, MU to be delivered were calculated from the measured dose rate determined using ionization chamber. The Linac was well calibrated to ensure accurate dose delivery during film calibration. Figure 3.8 below shows the set-up used for film calibration. Film strip was placed at 100 cm distance from the source, and the build-up of 10 cm was added on top of the film.

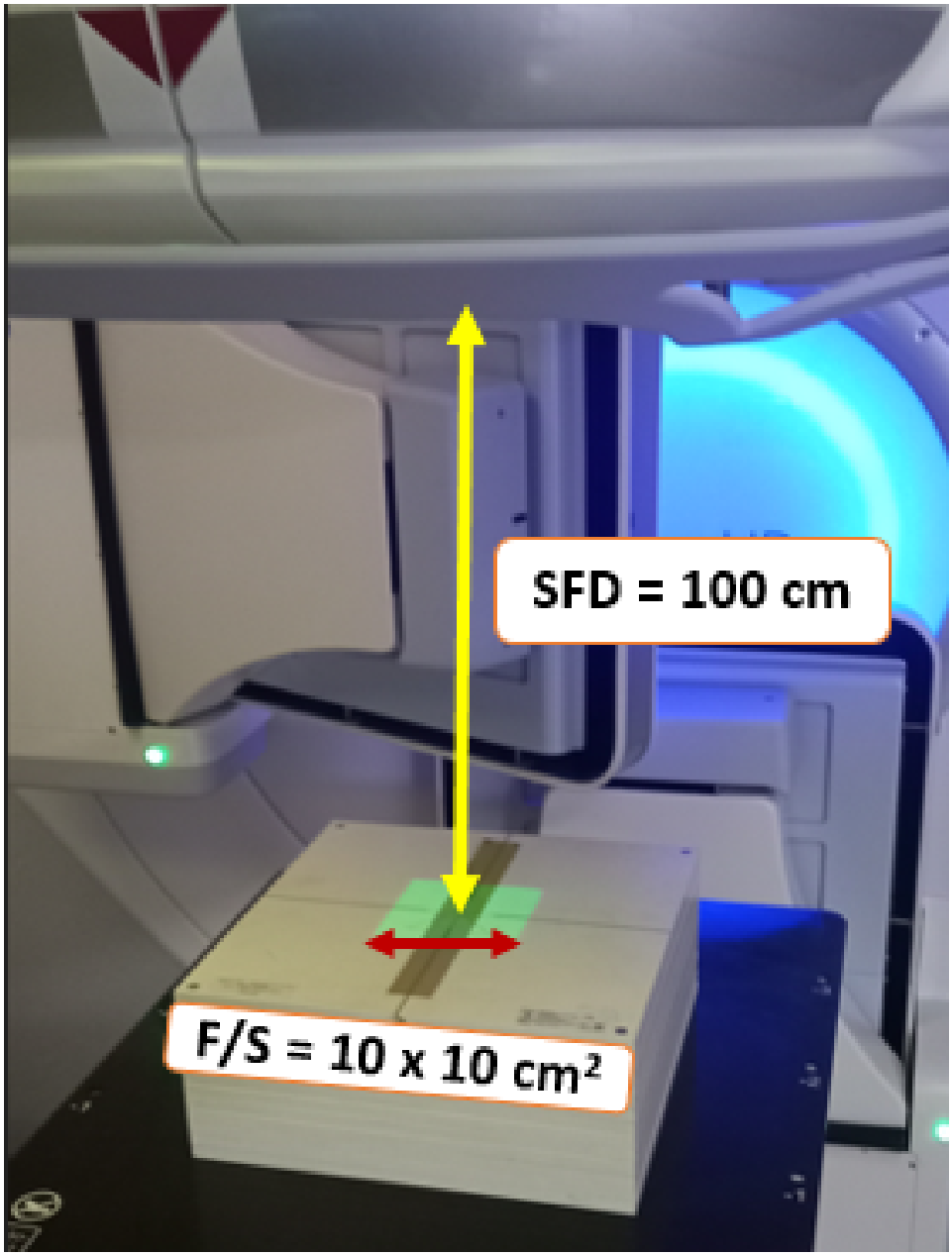

Figure 3.8: Photograph of the film strip placed at a depth of 10 cm for an SSD of 90 cm, and a reference field size of 10 x 10 cm^2.

3.2.2.2 Film scanning

Epson 11000 XL flatbed scanner, shown in Figure 3.9 was used. All irradiated films were scanned 24 hours later to allow for post-exposure changes to diminish [75]. For the lamp stability, three empty scans were performed. All three colour channels were used during the film scans to evaluate film and scanner artifacts for more accurate results.

Figure 3.9: Photograph of an EPSON 11000 XL film scanner used in this study

For calibration purposes, films were placed at the center of the scanner, scanned in the professional mode, and in the same orientation (land scape orientation) throughout the measurements to minimize the lateral artifacts [76]. The resolution of 72 dots per inch (dpi) was used and 48-bit RGB mode. The dose resolution with 48-bit colour produces 16-bits per channel compared to 24-bit color. A glass compression plate was used to ensure that the film was flat on the scanner, as shown in Figure 3.10 below:

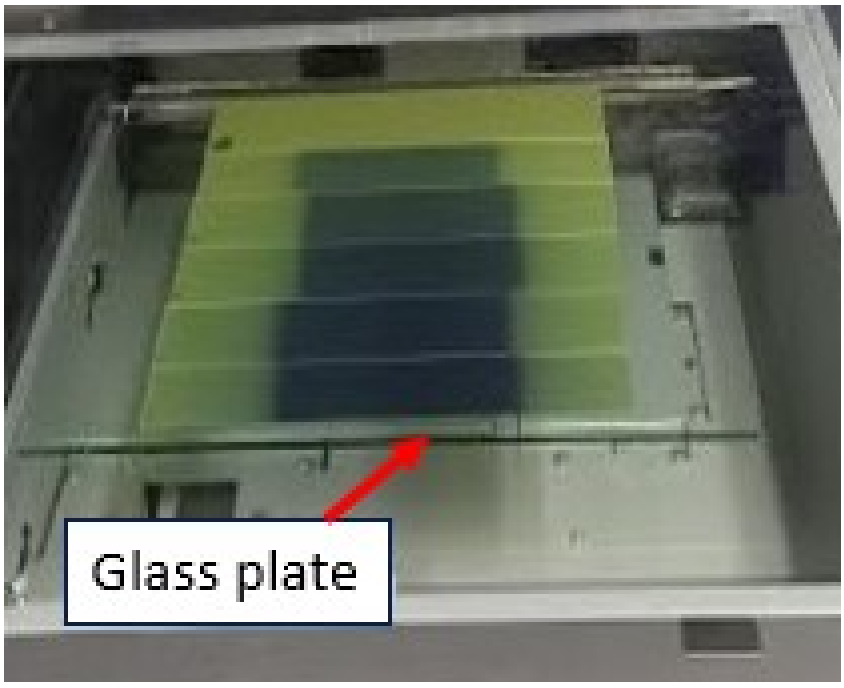

Figure 3.10: Glass compression plate used during film scanning.

Scanning of films started by selecting the "preview" to warm up the light source. This workflow was repeated to ensure the correct alignment and orientation. All images were saved as "TIFF" files .

3.2.2.3 Film analysis

The imageJ software was used to analyze films. All three colour channels were selected for data analysis. Default settings were changed to display a gray-scale. The region of interest (ROI) of 0.5 x 0.5 cm^2 was drawn at the center of each piece of film. The measured mean pixel values were converted into optical density (OD) using the following equation:

$$OD = log_{10}\left(\frac{PVunexp.}{PV_{exp.}}\right) \tag{3.3}$$

Where $PVunexp.$ is the pixel value of the un-exposed film for background correction, and $PV_{exp.}$ is the pixel value of the exposed film. The optical densities calculated from the measured intensities are used to produce the film's characteristic curves.

3.2.2.4 Film beam profile

Films were exposed to 500 MU for different field sizes ranging from 0.5 x 0.5 cm^2 to 10 x 10 cm^2. A line equal to the field width was drawn on a scanned image across the center of film using ImageJ software as shown in Figure 3.11 (a). The distance in pixels was converted to a known absolute distance to convert the units for off center values to set the image scale, shown by Figure 3.11 (b).

Treatment planning data was used as the reference, hence the distance from the off center had to be measured in centimeters. A line profile beyond 2 cm from the edges of the field was drawn across the film to produce the dose profile.

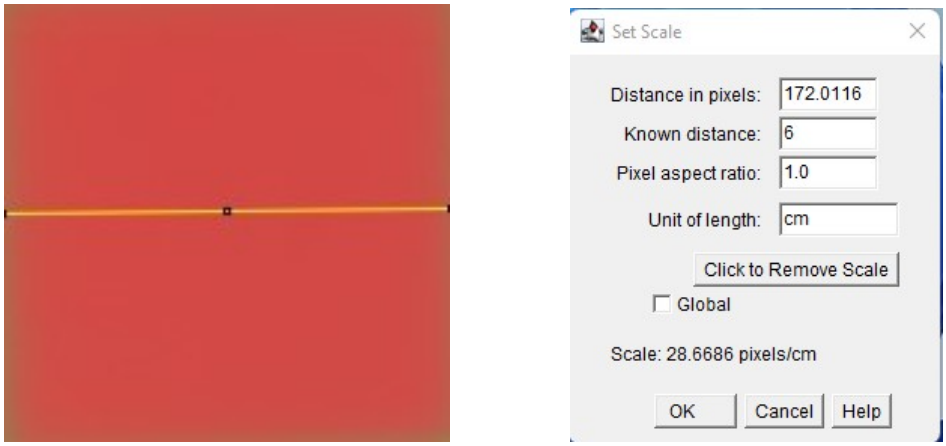

(a) **(b)**

Figure 3.11: Film profile measurements with imageJ software, (a) line drawn across the central axis of the film that is equal to the beam size to set the scale, (b) dialog of the imageJ software to convert the distance in pixel to absolute distance in centimeters.

Figure 3.12 illustrates a beam profile for a (e.g 6 x 6 cm^2) field size measured with imageJ software from the image shown by Figure 3.11 (a).

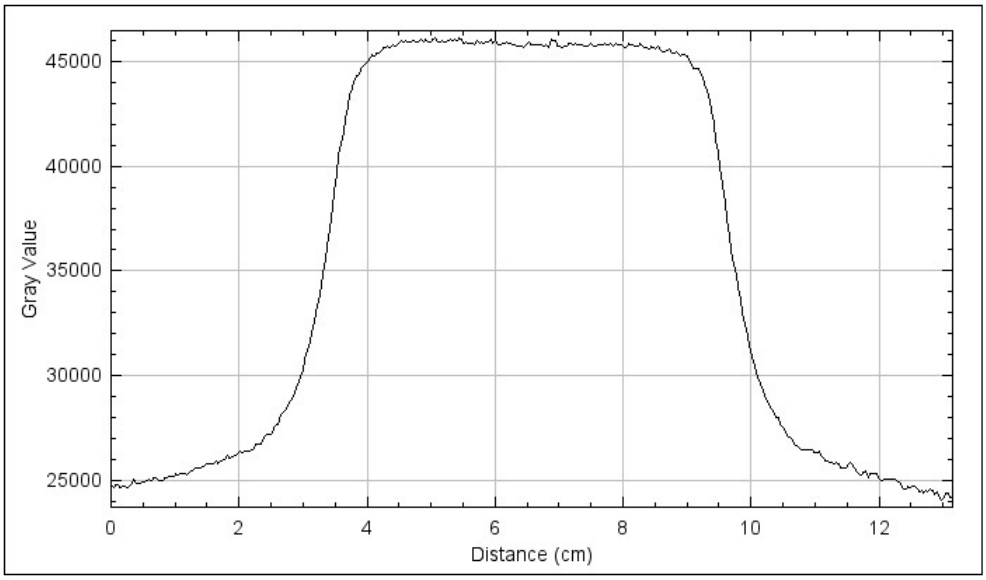

Figure 3.12: Dose profile produced by imageJ software.

The obtained data for all different field sizes were exported to an excel spreadsheet for processing. The logarithmic ratio of the background intensity, and the transmitted intensity, was used to convert the mean grayscale to the optical density (OD) to match the profiles in terms of the field width with the planning data.

3.3 TPS dose rate

Dose rate (DR) in cGy/MU was calculated by the TPS at a depth of 10 cm, with a reference field size of 10 x 10 cm^2 to be compared with the delivered linac output.

CT scanned image from the TPS is shown in Figure 3.13 with a point of interest placed at a depth of 10 cm. Monaco software has an option to force different structures of the scanned CT images to one. Therefore, the electron density of the CT scanned image was forced to be equal to one.

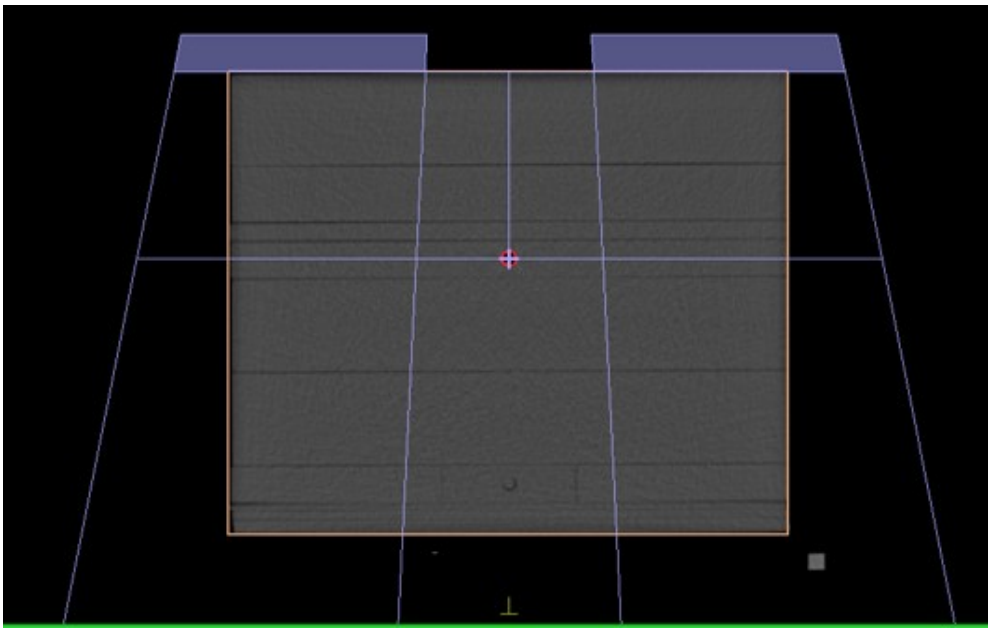

Figure 3.13: Reference conditions for TPS output measurements, 10 x 10 cm^2, 10 cm depth, 90 cm SSD, and 100 MU.

3.4 TPS beam profiles

A line profile was drawn at a depth of 10 cm for each field size in both the transverse plane and sagittal plane. A side view of a CT scanned solid water phantom is shown in Figure 3.14, dose values were determined at several points, left to right of the central axis (across the field) for each field size. The distance of 2 cm beyond the field edge was maintained through out the calculations.

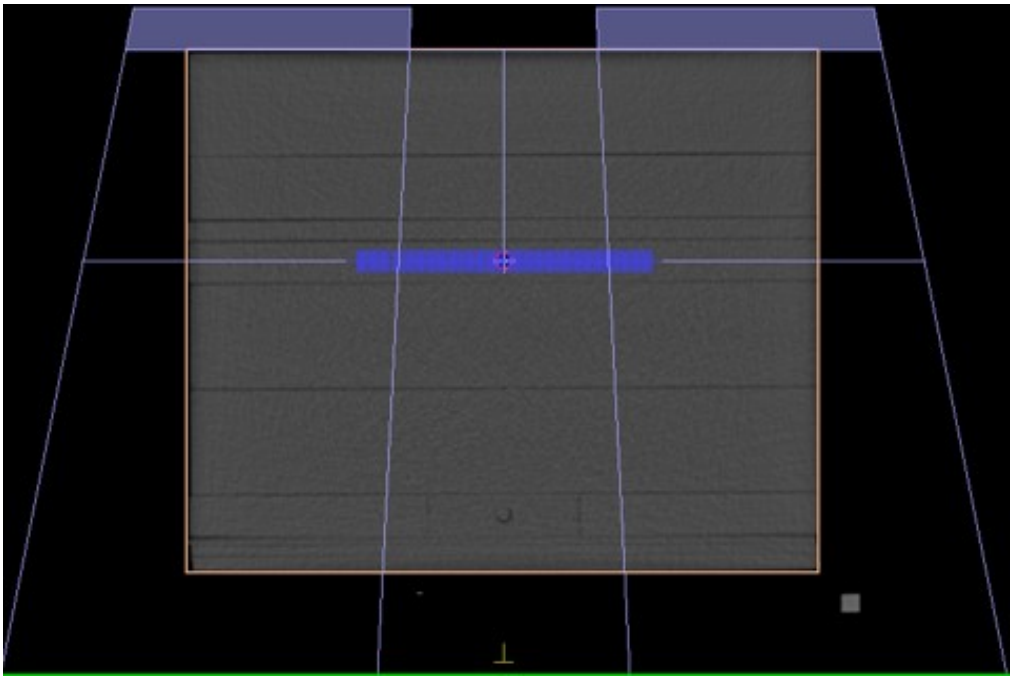

Figure 3.14: Line profile drawn at 10 cm depth for a reference field size of 10 x 10 cm^2. Relative dose calculated at several points across the beam using a resolution of 0.1 mm.

Relative dose values calculated by the treatment planning computer were copied into an excel spreadsheet to plot the beam profile. Using different detectors, TPS beam profiles were compared with measured profiles for the same geometry.

3.5 TPS output factors

Treatment field were created in a solid water equivalent phantom in Monaco. Field output factors were created for a range of field sizes, starting from the smallest field size of 0.5 x 0.5 cm^2 produced by the Elekta linac to a reference field size of 10 x 10 cm^2.The calculation point was set at a fixed depth of 10 cm in solid water phantom with an SSD of 90 cm from the source.

Radiation dose from each field size was calculated and normalized to a reference field size of 10 x 10 cm^2. The output factors calculated using the treatment planning computer was be used to validate the measured data with different detectors. This is illustrated by Figure 3.15 below

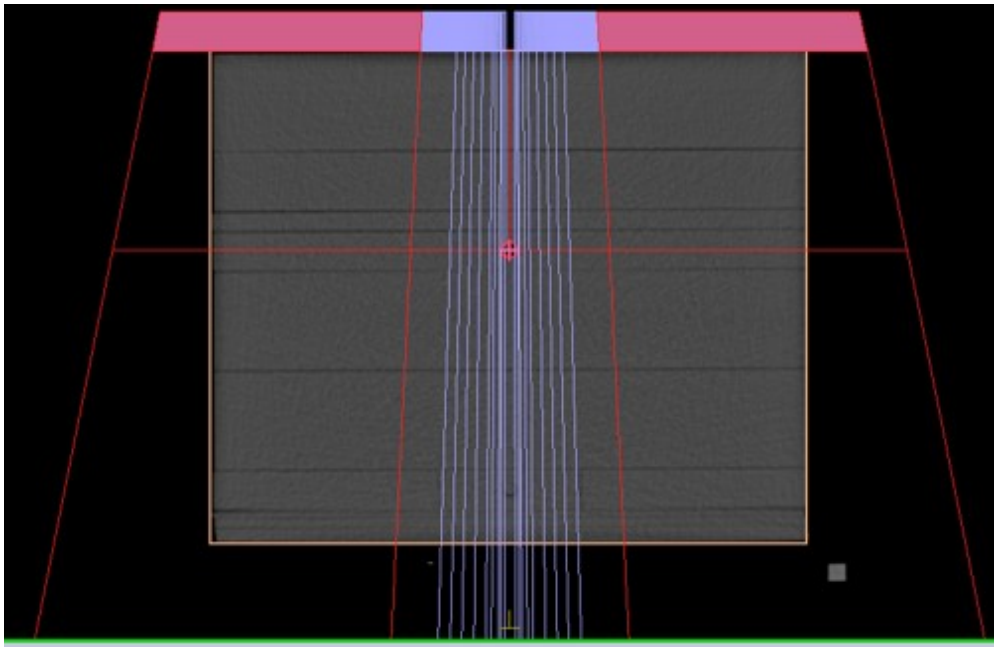

Figure 3.15: CT image of a solid water equivalent phantom with the calculation point placed at 10 cm depth from the surface for field sizes 0.5 x 0.5 cm^2, 0.8 x 0.8 cm^2, 1 x 1 cm^2, 1.5 x 1.5 cm^2, 2 x 2 cm^2, 3 x 3 cm^2, 4 x 4 cm^2, 5 x 5 cm^2, 6 x 6 cm^2, and 10 x 10 cm^2. The vertical blue lines indicate the field edges for the various field sizes

3.6 Field output factor measurements

In this study, three different detectors: EBT3 film, two PTW ionization chambers, 31021 semiflex (SF) three-dimensional (3-D) and 31014 Pinpoint (PP), and a-Si EPID were used to perform field output factor measurements. All measurements were carried out with three high photon energies, 6MV FFF, 6MV FF and 10 MV FF produced by an Elekta HD Versa linear accelerator. Treatment planning results and literature data were used to compare and evaluate the results from these three detectors.

3.6.1 Gafchromic EBT3 film

Output factors are determined at the center of the radiation fields and they map the relative dose from one field to the next and normalized to a reference field size; sufficient monitor unit must be given to the film to obtain good results. The relative dose factors for various small field sizes ranging from 0.5 x 0.5 cm^2 to 10 x 10 cm^2 were measured at a depth of 10 cm and SSD of 90 cm in a solid water phantom.

The set-up for the field output factor measurements is shown in Figure 3.16.

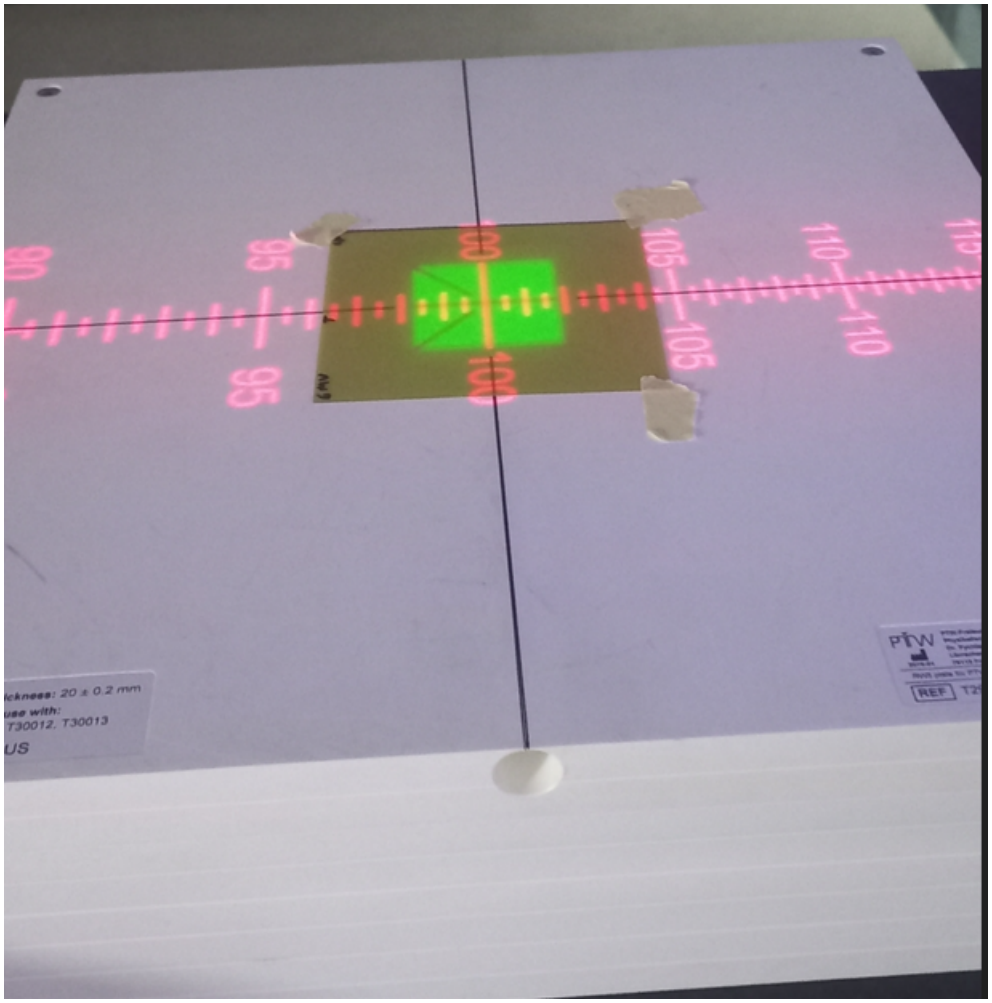

Figure 3.16: Photograph of a piece of film (fixed with three adhesive tapes) placed at 100 cm from the source showing the field size centered on the film. The target side and the beam size is marked at the edges of the film.

The build-up of 10 cm solid water equivalent material was added on the film to perform measurements at a depth of 10 cm. As the response of a film depends on the dose given on it; each piece of film was exposed to 500 MU.

To account for changes in film optical density with time, films were scanned 24 hours after irradiation. This procedure reduces the post-irradiation coloration effects of Gafchromic EBT films.

Flatbed Epson 11 000 XL scanner with the scanning parameters mentioned in sectioned 3.2.2.2 were used for field output factor measurements. The scan

direction also contributes to the in-homogeneity within the exposed area of the film, and the same processes were repeated accordingly. Using the imageJ software, one piece of film was uploaded at the time to perform analysis. The square regions of interest with an area of 0.2 x 0.2 cm^2 was drawn on each piece of film.

The mean pixel values was determined from the measured pixels at different regions to solve for heterogeneity. Optical densities were calculated from the measured mean pixel values using equation 3.3. During the calibration process, the 3rd degree polynomial function was found to be the best fit as the relationship between the dose and OD was shown to be non-linear. The equation from the dose-optical density curve was used to determine the absorbed dose.

3.6.2 PTW ionization chamber

PTW 31014 PinPoint ionization chamber and PTW 31021 3D Semiflex detector were used for field output factor measurements in this study. The two PTW detectors used for output factor measurements are shown in Figure 3.17 below:

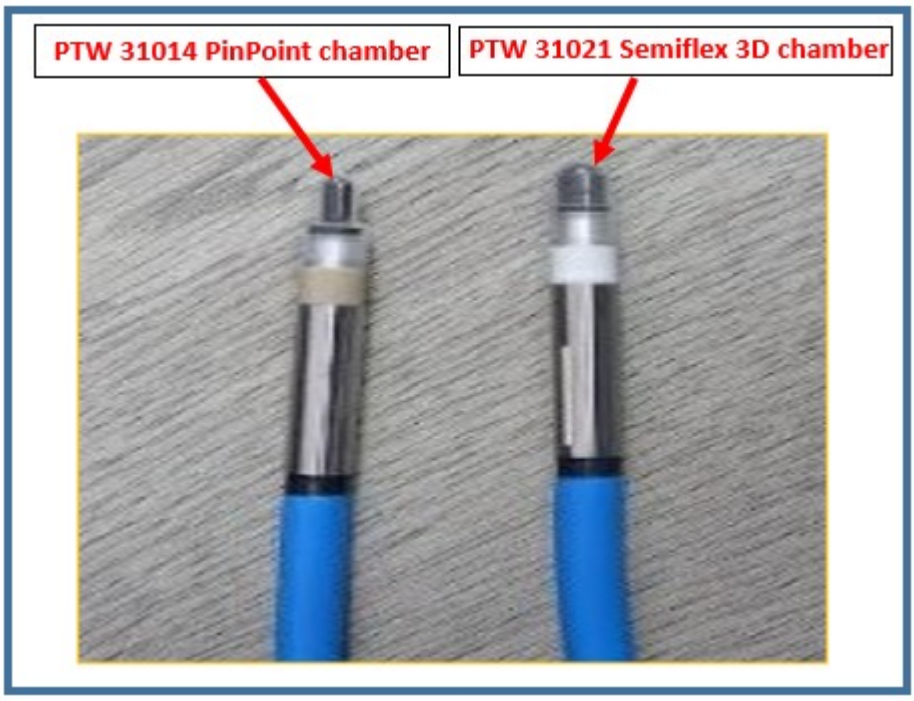

Figure 3.17: PTW 31014 Pinpoint ionization chamber and PTW 31021 3D Semiflex.

Contrary to Gafchromic EBT3 film, all chamber measurements were acquired in water phantom at 90 cm SSD and the 10 cm depth using a PTW MP3 scanning water tank. The gantry and collimator angles were set to zero degrees for all the measurements. The chamber was aligned perpendicular to the beam central axis. For an isocentric set-up, the detector was positioned at 100 cm from the source. Ion chamber measurements were performed under the same geometry set-up as in Gafchromic EBT3 film. The use of the reference detector in small field measurements is not feasible, therefore, all the measurements were performed without the reference detector. The experimental set-up for chamber measurements is illustrated in Figure 3.18.

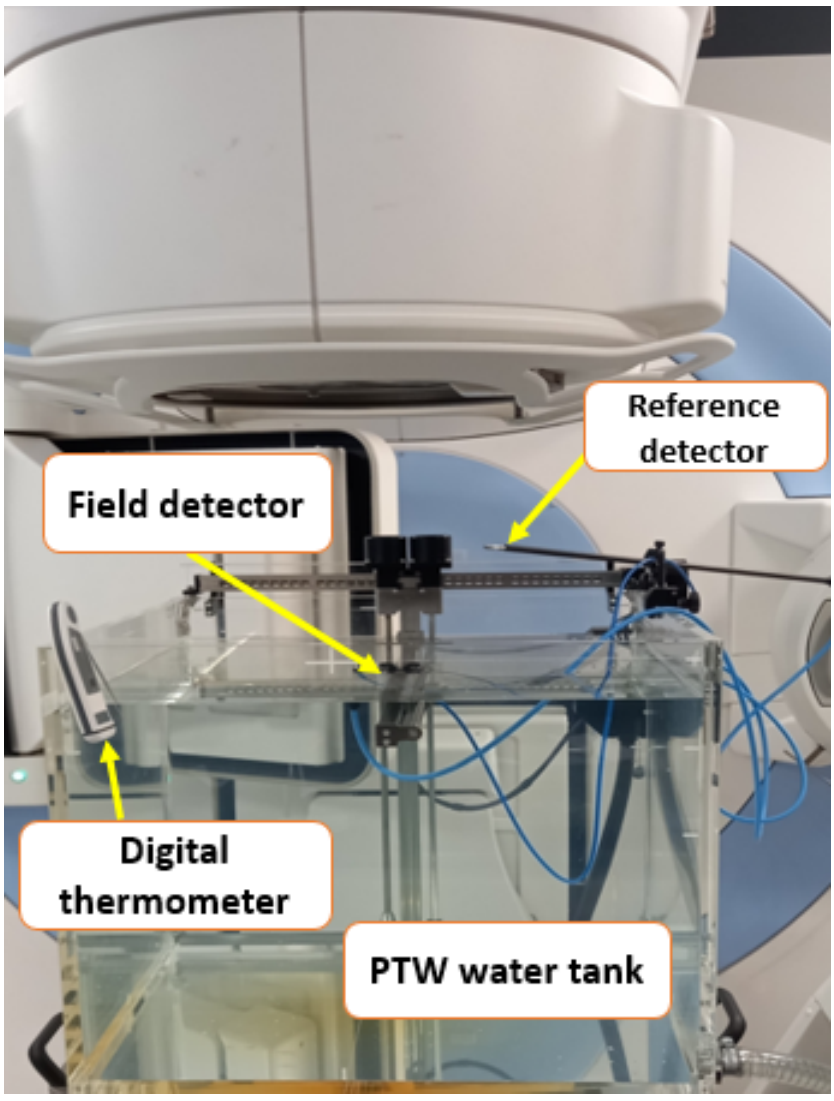

Figure 3.18: Photograph of the PTW MP3 water scanning tank for small volume detectors, showing field and reference detectors in perpendicular orientation for beam profile and field output factor measurements.

3.6.2.1 CenterCheck

The new PTW sotfware includes the detector alignment option. The CenterCheck from the MEDPHYSTO software was used to verify the alignment of detector with the beam central axis. This was done by measuring the beam profiles at a depth of 3 cm in water with machine specific reference field size of 10 x 10 cm^2. Two profiles were first measured, in-plane and cross-plane as shown by the Figure 3.19 from PTW software. This was performed to ensure that the detector is positioned at the center of the radiation field relative to the light field.

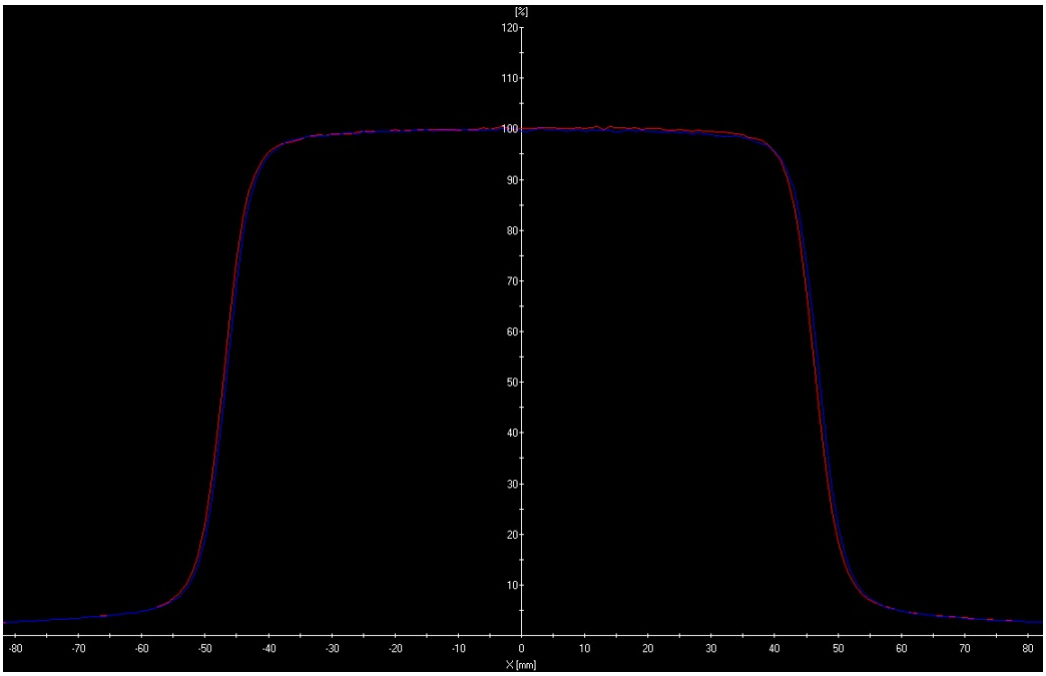

Figure 3.19: Detector alignment to the cross hairs for dose profile measurements and field output factors.

In-plane and cross-plane profiles at the depth of 3 cm to verify the water tank level, field alignment and beam center using PTW software. Also, this is performed to verify accuracy of the effective point of measurements of the volumetric detector. This was performed to minimize the uncertainties associated with the positioning of the detector.

3.6.3 EPIQA configuration

EPID configuration ensures accurate and reliable dose measurements during patient specific quality assurance (QA). Radiation field with known dose were placed on the water phantom Dicom structure to produce photon fluence from

the TPS. The fluence of the transmitted radiation was measured with MLCs closed.

Figure 3.20 shows the water phantom DICOM structure for dose calculation. The acquired EPID images of radiation fields were analyzed using the EPIQA software. Calibration curves generated based on the measured pixel values and the known radiation dose are used to convert the pixel values.

The pixel values acquired using the EPID at depth of maximum dose for photon beams are converted to dose map. EPIQA uses GLAaS algorithm to convert grey scale to dose matrices at depth of maximum dose in water [73].

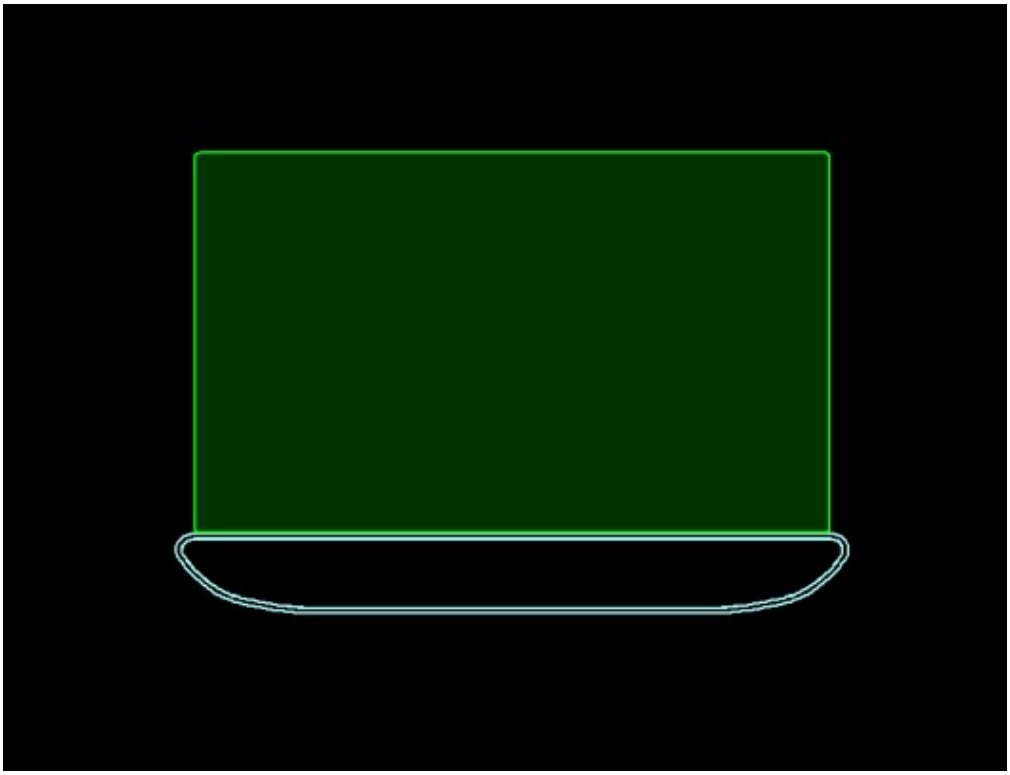

Figure 3.20: Water phnatom Dicom structure set used by GLAas algorithm for dose calculation in TPS.

The portal images from amorphous detectors (a-Si) are transformed into absorbed dose in water for higher energy beams without any build-up material on the panel [73].

The radiation dose calculated by the treatment planing system is verified using this algorithm. Figure 3.21 shows the solid water phantom for calibration factor measurements.

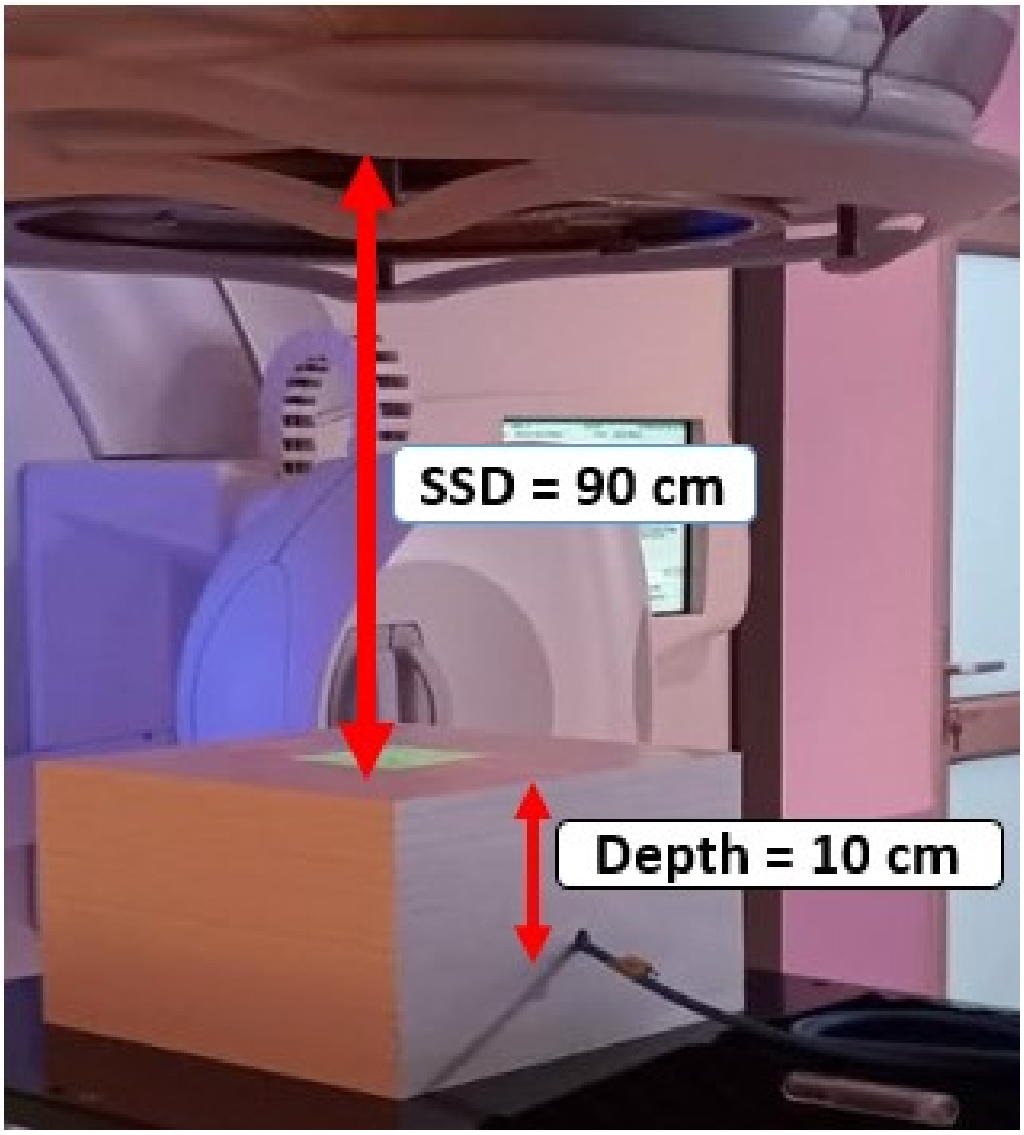

Figure 3.21: Set-up for EPID configuration: solid water phantom for dose calibration factor (MU/Gy) measurements.

The EPIQA software accounts for both the primary beam as well as the transmitted radiation through the multi-leave collimators (MLC). This is performed by the algorithm on a pixel-by-pixel basis([72]).

The a-Si detectors of an Elekta HD versa linac are fixed at a distance of 160 cm from the source, as shown in Figure 3.22 below:

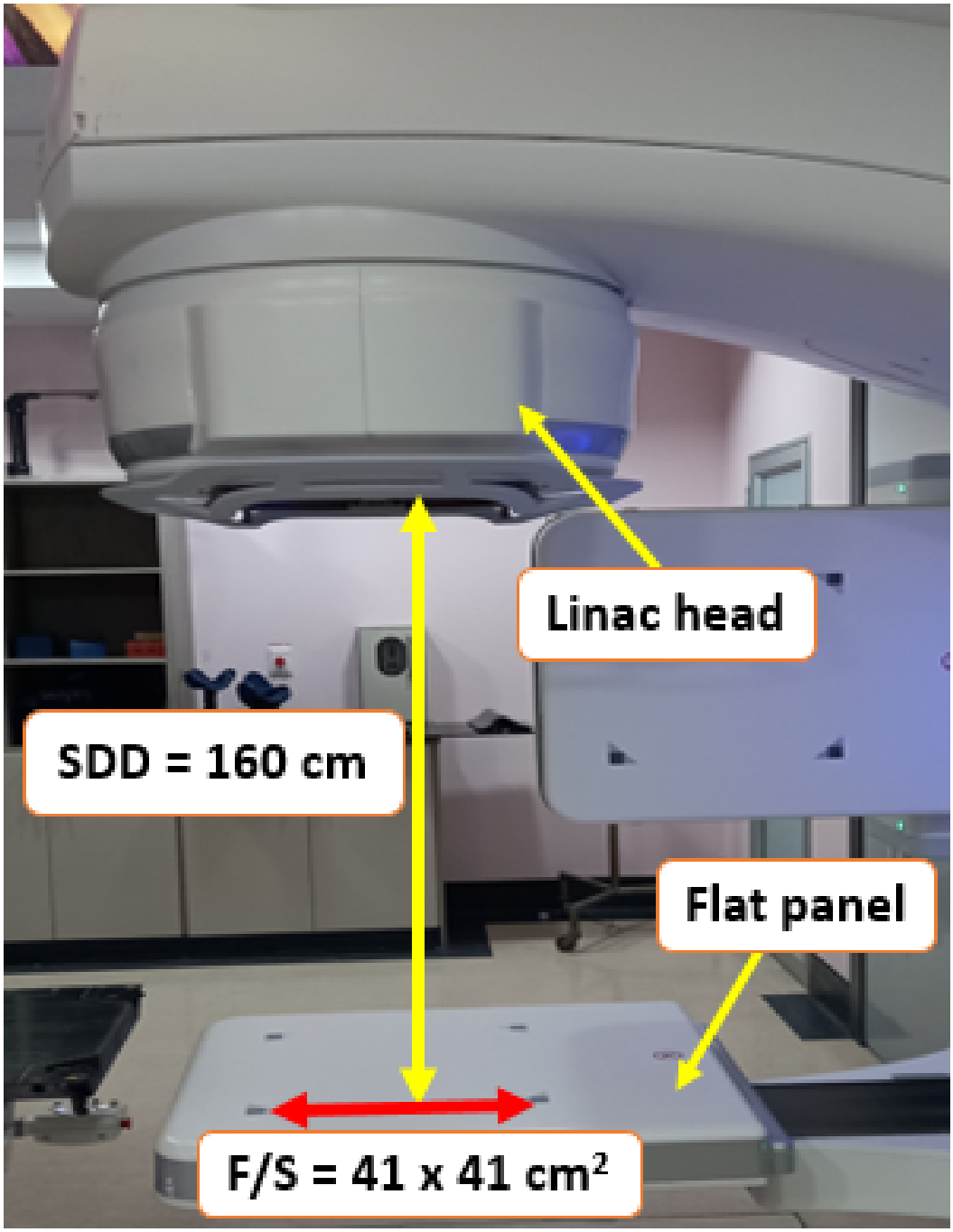

Figure 3.22: Photograph of the Elekta versa HD linac head (source of radiation) and the electronic portal imaging device fixed at 160 cm from the radiation source for primary and MLC transmission measurements

The two dosimetric methods, non-transmission and transmission were adopted in this study. In non-transmission method, there is no attenuating material between the radiation source and the EPID. The intensity is measured on the portal imaging device without passing through any attenuating medium.

3.6.3.1 Primary radiation

In this work, the algorithm was configured to acquire the images at 10 cm depth for 6MV FFF, 6MV FF, and 10MV FF beams. Detector response to both the primary radiation and MLC transmission was determined as per EPIQA manual. For the EPIQA configuration, the data in treatment planning system needed to be label as per the recommendations from the EPIQA manual.

The following field sizes are recommended: 3 x 3 cm^2 , 5 x 5 cm^2, 10 x 10 cm^2, 12 x 12 cm^2, 15 x 15 cm^2, 20 x 20 cm^2, 25 x 25 cm^2. Some fields were modified in the original radiotherapy (RT) plan template to smaller field sizes ranging from 0.5 x 0.5 cm^2 to 2 x 2 cm^2 below 3 x 3 cm^2. The fields that are mandatory for EPIQA configuration are: 3 x 3 cm^2, 10 x 10 cm^2, 25 x 25 cm^2.

Images were acquired using the Elekta electronic portal imager system known as iView. For the calibration process, each field was exposed to three different MUs: 20, 30, and 50 as recommended in the EPIQA manual.The total dose plan and the individual beam doses were obtained from the Monaco treatment planning system.

The farmer type ionization chamber with an air volume of 0.6 cm^3 was used to measure the dose calibration factors at various mandatory field sizes. All the machine output factor measurements were carried out at a depth of 10 cm in a perspex phantom with 100 MU. During measurements, the ionization chamber set-up was made to match the EPIQA set-up geometry.Images for 10 x 10 cm^2 were acquired with 50 MU for all three photon energies (6MV FFF, 6MV FF, 10 MV FF) for calibration purposes.

3.6.3.2 MLC transmission

Firstly, an open square field size of 10 x 10 with 50 MU is recommended; then the transmission through the multi-leaf collimators (MLC) is performed. MLC transmission factors for different MUs(50 MU,100 MU, and 200 MU) were acquired with EPID as per recommendations. Transmitted radiation was also performed with ion chamber for 10 x 10 cm^2 open field and closed MLC. All the acquired data was then exported in DICOM format for EPIQA configuration.

3.6.3.3 Field output factor measurements

Treatment fields for the field output factor measurements were created in a water phantom in the Monaco treatment planning computer and exported to the record and verification system (Mosaiq). TPS dose calculated for portal imaging is shown in the Figure 3.23 below:

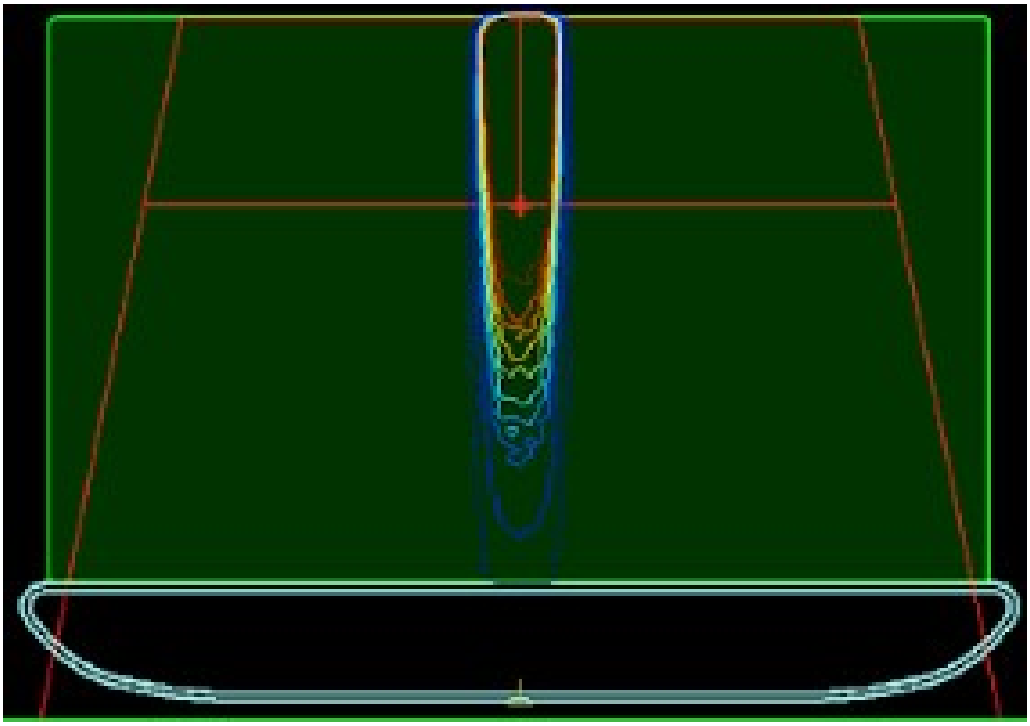

Figure 3.23: Screenshot of a transverse view of the DICOM structure water phantom showing TPS dose calculation for EPID.

EPID images from small photon fields of 0.5 x 0.5 cm^2, 0.8 x 0.8 cm^2, 1.0 x 1.0 cm^2, 1.5 x 1.5 cm^2, 2.0 x 2.0 cm^2, 3.0 x 3.0 cm^2, 4.0 x 4.0 cm^2, 5.0 x 5.0 cm^2, 6.0 x 6.0 cm^2, and 10.0 x 10.0 cm^2 were acquired with 100 MU using the HD Versa Linac and the Iview system and exported to the DICOM server.

For analysis, images from Iview with their logfiles for each image as well as the total plan dose and individual plan doses from TPS are required in the EPIQA software. Absolute dose maps measured at 10 cm depth obtained from the EPID images were compared to a dose calculated by TPS.

Chapter 4

Results and Discussions

4.1 Beam profile

Linac geometric uncertainties affect accuracy in dosimetric measurements of small fields as a result of mechanical machine performance e.g. the determination of the CAX. As a consequence, measurement and confirmation of the correct field sizes are crucial when measuring output factors and evaluating the influence of volumetric chambers on the dosimetric accuracy in small field measurements.

Different detectors such as radiochromic film (RCF) EBT3 type, PTW 31021 3-D Semiflex (SF), and PTW 31014 PinPoint (PP) were used to measure the beam profiles for each field size. Both cross-plane and in-plane profiles measured at 10 cm depth for the square field sizes (F/S) from 10 x 10 cm^2 down to 0.5 x 0.5 cm^2 were used to determine the full width at half maximum (FWHM).

In large fields, there is no loss of LCPE, and primary source occlusion. Therefore, the geometric field size and the FWHM acquired from beam profiles are almost equal. Contrary to small fields, the field becomes an overlap of beam penumbras, this happens in small fields as per the statement made earlier. Hence there is a need to verify the radiation field for each beam size. This depends on a number of factors such as the detector size used for measurements as well as the minimum field size for each photon energy. This was discussed in details in chapter 2, section 2.2.1. For a example, Figure 2.2 showed a range of LCPE of about 1.5 cm in 10MV beam.

Only small field sizes from 2 x 2 cm^2 down to 0.5 x 0.5 cm^2 are selected

for beam profiles presentation. This study used treatment planning data as reference data for beam profiles and field output factors. Treatment planning dose profiles calculated at 10 cm depth are compared to the measured dose profiles with different detectors.

Dose profiles for an Elekta HD versa Linac measured at 10 cm depth with various detectors to verify the beam dimensions for a range of field sizes (0.5 x 0.5 cm^2 to 2.0 x 2.0 cm^2) are shown in the Figures 4.1 to 4.6 below. These dose profiles are normalized to the central axis value.

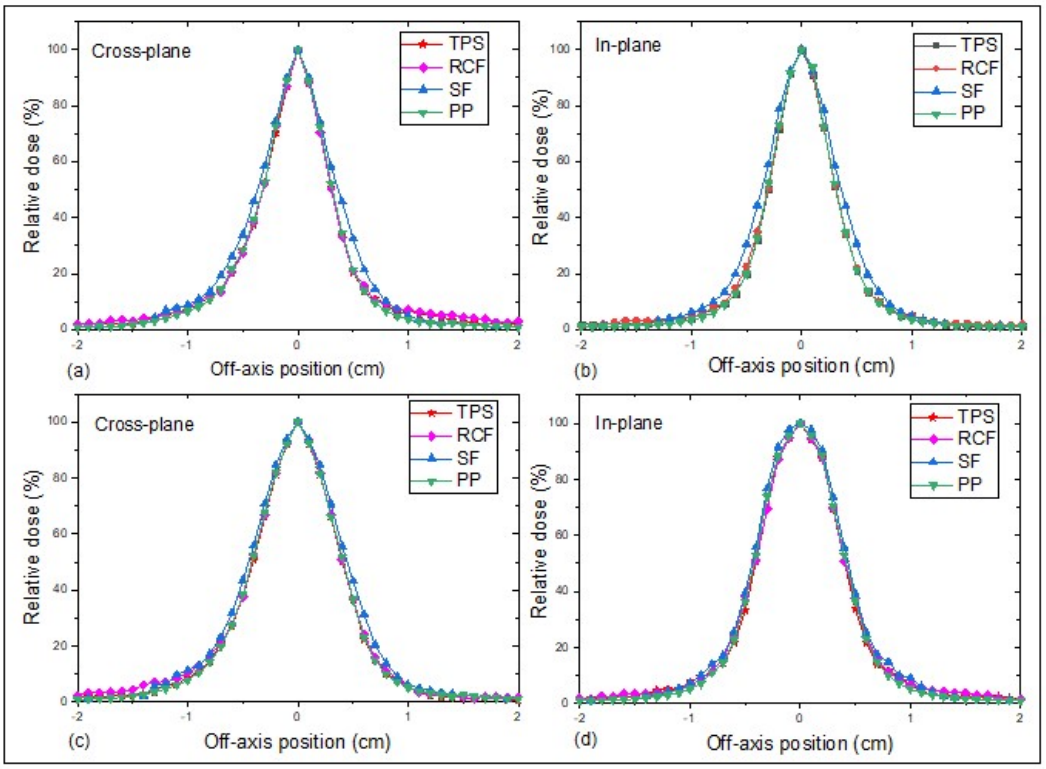

Figure 4.1: Cross-plane and in-plane profiles for 0.5 x 0.5 cm^2, and 0.8 x 0.8 cm^2 field sizes in 6MV FFF beam.

Dose profiles are not the same in smaller field sizes of 0.5 x 0.5 cm^2 and 0.8 x 0.8 cm^2 as illustrated in Figure 4.1. Consistently the SF 3-D detector shows a deviation with the rest of the detector. The signal measured by this detector is subject to volume averaging effect. The dose is accumulated across the dimensions of the detector volume. As a result, the penumbra width is overestimated.

Thus, the SF detector is not suitable to measure small fields beam profiles

in 6MV FFF beam for field sizes below 1 x 1 cm^2. Detector dimension is large compared to the field size, this affects the measured profiles in both fields.

Figs 4.2 (a), (b), (c), and (d) below show both cross-plane and in-plane dose profiles of 1 x 1 cm^2 and 2 x 2 cm^2 respectively, measured by three different detectors in FFF beam.

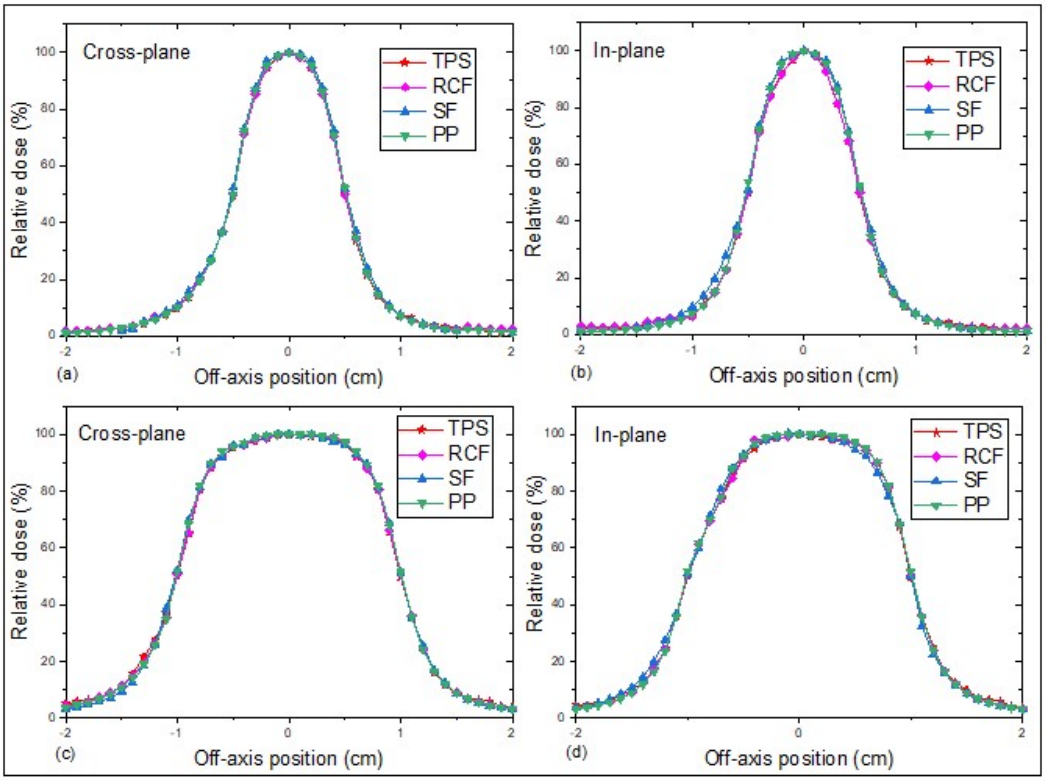

Figure 4.2: Cross-plane and in-plane profiles for 1.0 x 1.0 cm^2, and 2.0 x 2.0 cm^2 field sizes in 6MV FFF beam.

The measured profiles in both directions by the three detectors are comparable to the calculated TPS profiles for 1 x 1 cm^2 beam size, see figure 4.2 (a) and (b). All the three detectors were observed to be suitable for this field size. The dose measured on the beam's central axis and at the edges of the field is almost the same.

For a 2 x 2 cm^2 field size, all the three various detectors used in this study measured the beam profiles more accurately in comparison to the calculated TPS profiles.

The cross-plane and in-plane profiles of EBT3 film, Semiflex 3-D chamber, and PinPoint measured at 10 cm depth are compared to the TPS computed

profiles in Figs 4.3 and 4.4 below for 6MV WFF beam.

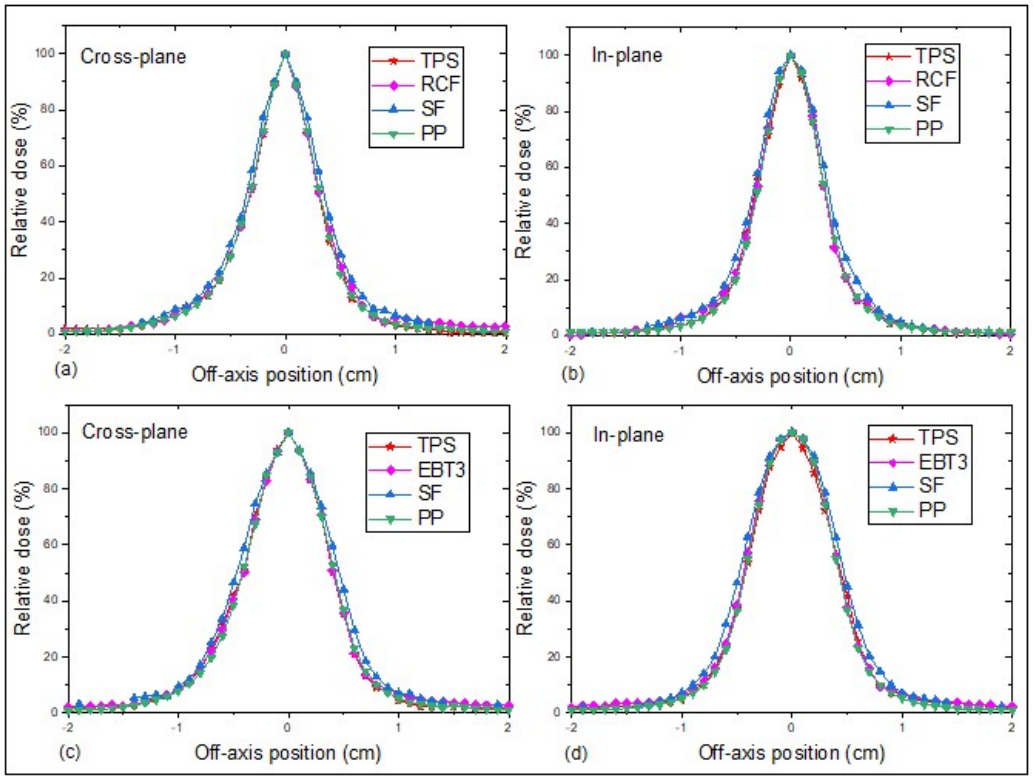

Figure 4.3: Cross-plane and in-plane profiles for 0.5 x 0.5 cm^2, and 0.8 x 0.8 cm^2 field sizes in 6MV photon beam.

The use of a relatively larger ionization chamber (SF) in small fields can scatter and absorb the radiation beam. This has resulted in the perturbation effect which affects the accuracy of the measured beam profile. Therefore, there is a slightly increased in dose profiles measured with the SF detector in both in-plane and cross-plane directions. Good agreement was not obtained with SF detector compared to other detectors for a 0.5 x 0.5 cm^2 and 0.8 x 0.8 cm^2 as shown by the above Figs 4.3 (a) to 4.3 (d).

Figs 4.4 (a) to 4.4 (b) below depict a good match for all beam profiles measured by the three different detectors compared to the TPS calculated profiles.

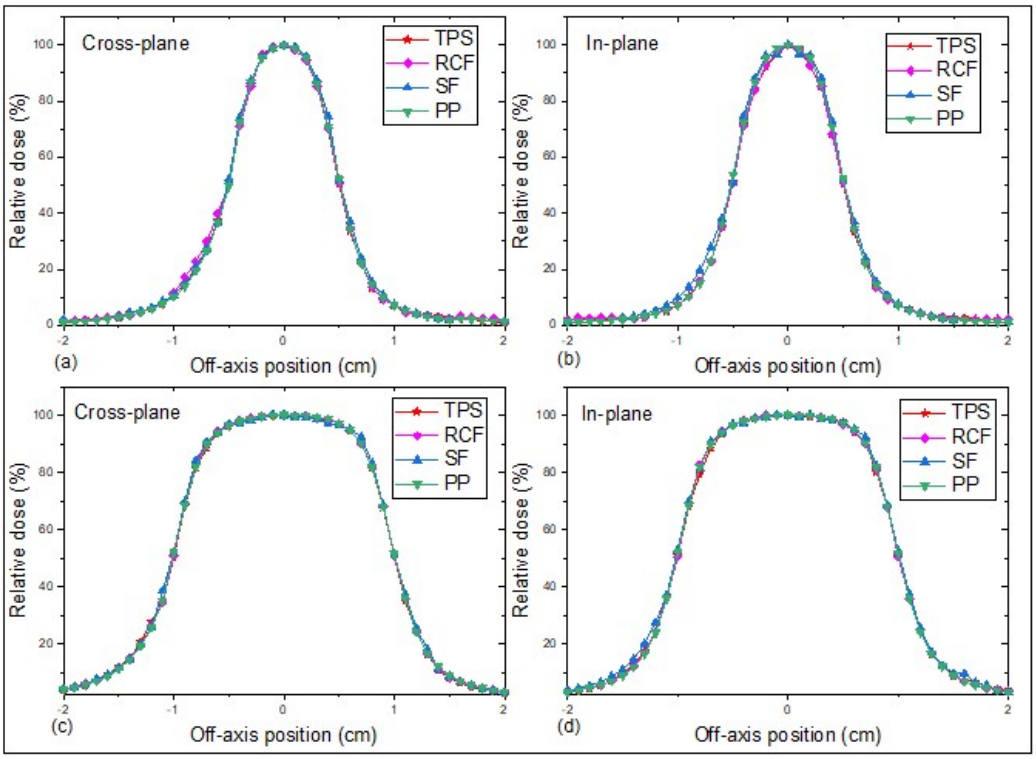

Figure 4.4: Cross-plane and in-plane profiles for 1.0 x 1.0 cm^2, 2.0 x 2.0 cm^2 field sizes in 6MV photon beam.

Beam profiles in small photon fields are quite different from large fields due to the lack of electronic equilibrium, the impact of beam collimation and dose-volume averaging effect. The steep dose gradients are observed at the field edges. Therefore, higher spatial resolution detectors are required to accurately measure the profile in the entire field and in the penumbra region.

Figs 4.5 (a) to 4.5 (d) below illustrate beam profiles measured at 10MV FF beam for the smallest fields.

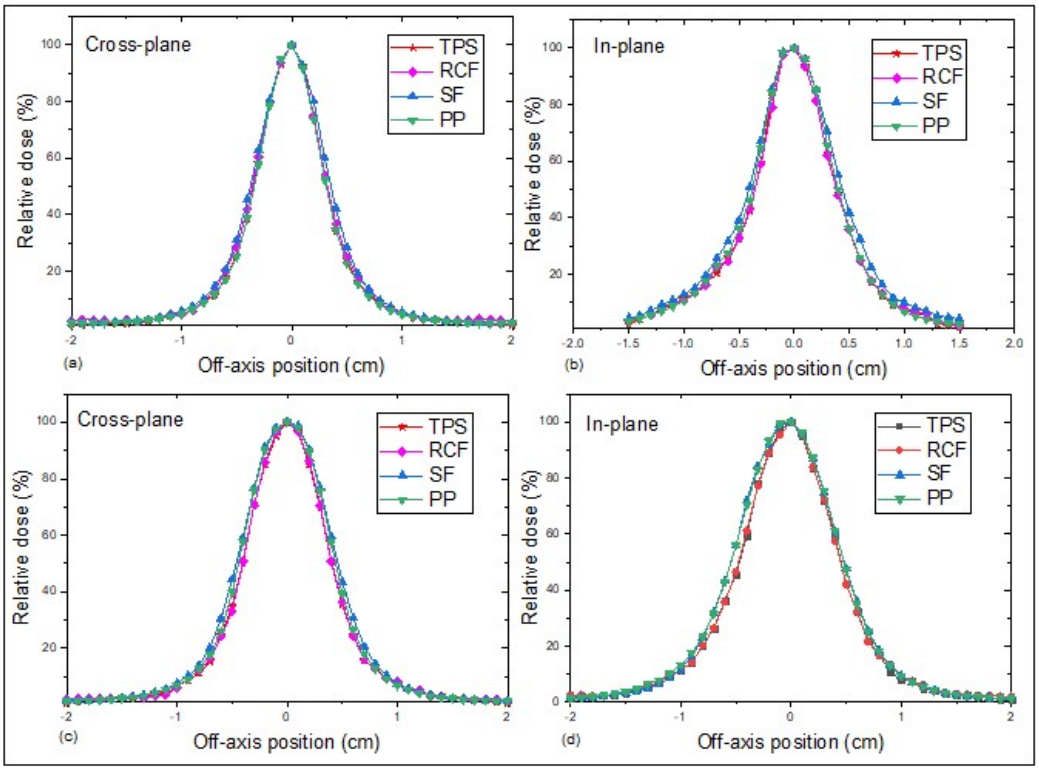

Figure 4.5: Cross-plane and in-plane profiles for 0.5 x 0.5 cm^2, and 0.8 x 0.8 cm^2 field sizes in 10MV photon beam.

The field size is defined by MLC in the X-axis and jaws in the Y-axis. For this reason, a slightly difference was observed in the beam profile measured along the in-plane direction by the SF chamber in both field sizes. Good agreement was obtained in the measured profiles with RCF and PP detectors in both cross-plane direction and in-plane under 10MV FF beam for smaller fields.

Figs 4.6 (a) to 4.6 (d) show beam profiles measured in 10 MV FF for field sizes greater than 0.8 cm.

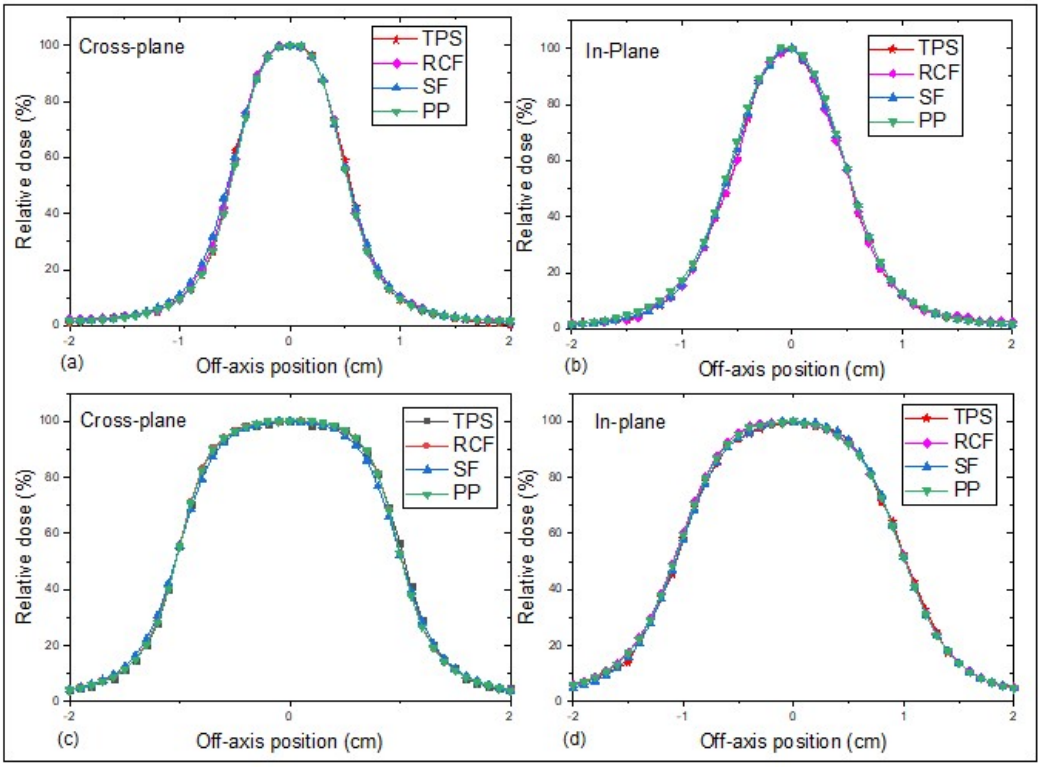

Figure 4.6: Cross-plane and in-plane profiles for 1.0 x 1.0 cm^2, and 2.0 x 2.0 cm^2 field sizes in 10MV photon beam.

As shown by the above Figs, beam profiles measured with different detectors for the F/S$\geq$ 1 x 1 cm^2 along the In-plane direction for 6MV FF photon energy best match the TPS data. In-plane profiles matched very well for all field sizes greater or equal to 1 x 1 cm^2.

Beam profiles look more or less the same in small fields below 1 x 1 cm^2 for all three photon energies except for those measured with a SF chamber. As the field size increases, dose profile are going to start overlapping.

4.2 Determination of radiation field size

The radiation FS in small field measurements is defined by the FWHM. As the field size is reduced, there is a significant difference between the FWHM and the geometrical field size. Therefore, the field size results in uncertainties in the FOF measurements, hence it is important to verify the field for each beam.

According to the new IAEA TRS 483 protocol, the equivalent square field

is determined by the specific clinical equivalent square field size [9]:

$$S_{clin} = \sqrt{X * Y} \tag{4.1}$$

Where S_{clin} is the smallest equivalent square field size, X is the cross-plane field width, and Y is the value measured in the in-plane direction for a specific field size. Equation 4.1 only applies to square field sizes when the ratio of X/Y is greater than 0.7, but less than 1.4. It is also defined as the FWHM at a measuring depth in small photon fields.

4.2.1 FWHM for 6MV FFF beam

Dose profiles of all three photon energies were characterized to verify errors associated with incorrect field width. The F/S defined by the FWHM measured from beam profiles by all three detectors in 6MV FFF beam are illustrated in Figure 4.7. The maximum difference observed between the measured FWHM with a SF and the calculated TPS FWHM is 0.18 cm for the smallest F/S of 0.5 x 0.5 cm^2

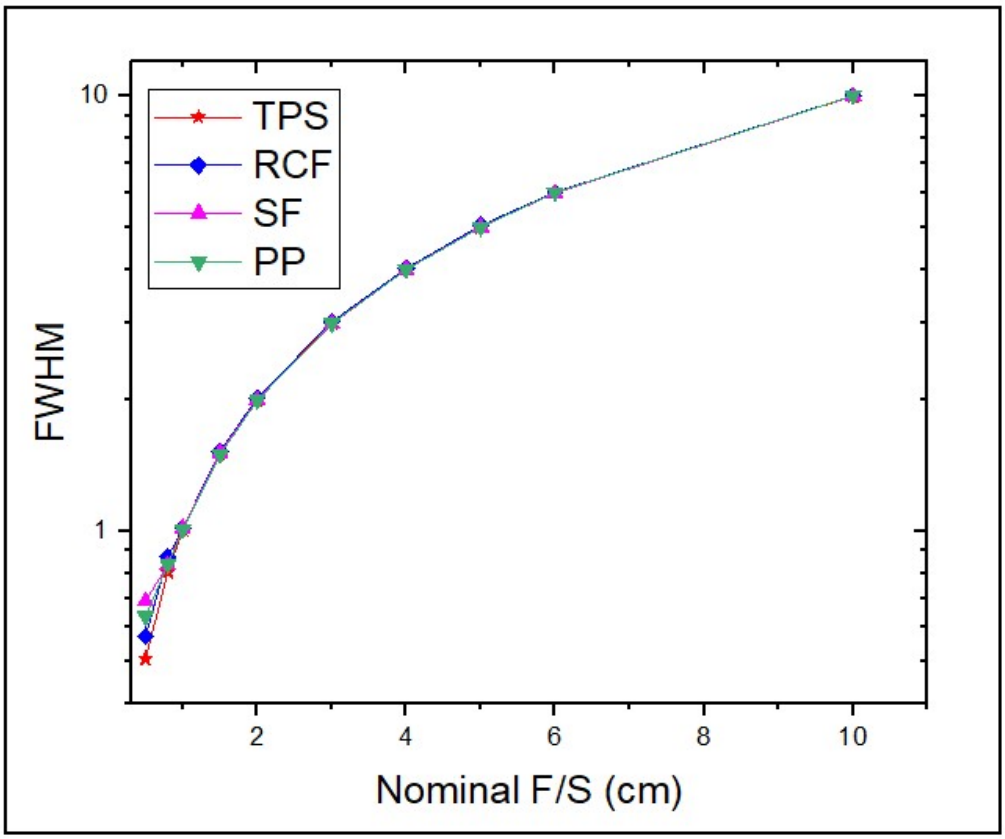

Figure 4.7: Measured FWHM with various detectors in 6MV FFF beam.

The % difference of FWHM for all detector readings in 6MV FFF beam is shown by Figure 4.8 below. The maximum difference obtained between the TPS calculated FWHM and the measured FWHM by all detectors was 26.3% for SF 3-D detector, 20.1% for PP chamber and 11.3% for RCF for the smallest field size of 0.5 x 0.5 cm^2.

This is a detector related condition, the volume of a SF 3-D detector is too big compared to the dimensions of 0.5 x 0.5 cm^2 field size. Thus, the bigger the volume of the detector, the larger the volume averaging effect. The measured field size is broaden, hence the higher % difference in FWHM for smaller fields.

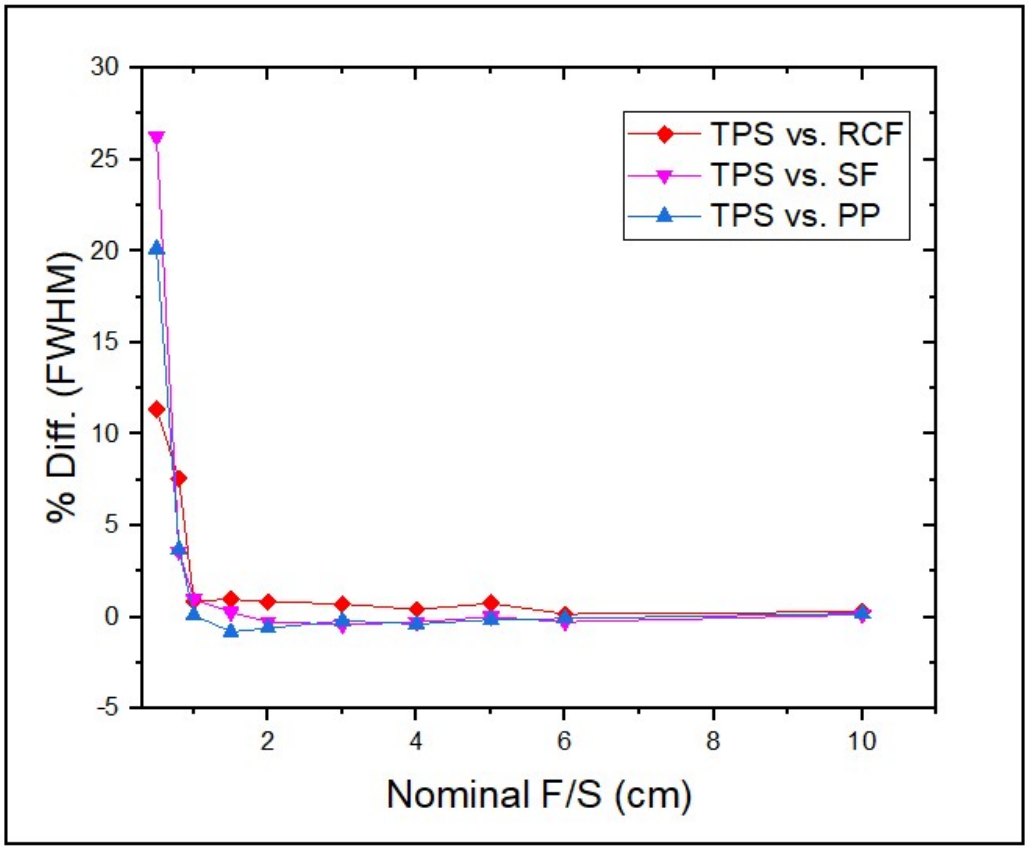

Figure 4.8: % difference of the measured FWHM with various detectors for 6MV FFF beam.

At field sizes below 6 x 6 cm^2, the measured FWHM by the two volumetric detectors is less than the TPS values. The two PTW detectors, semiflex and pinpoint underestimated the FWHM for 6MV FFF beam.

4.2.2 FWHM for 6MV FF beam

Figure 4.9 shows the FWHM measured by various detectors in 6MV FF beam. The maximum value observed between the measured FWHM with a SF and the calculated TPS FWHM is 0.27 cm for the smallest FS of 0.5 x 0.5 cm^2.

The FWHM measured with a 3-D SF chamber is larger than the collimator settings at the smallest field size. Therefore, the differences in FWHM measured by the SF detector increases as the F/S gets smaller due to partial source occlusion, volume averaging effect and the loss of LCPE. Less signal is obtained at the beam's central axis compared to the dose measured outside of the field.

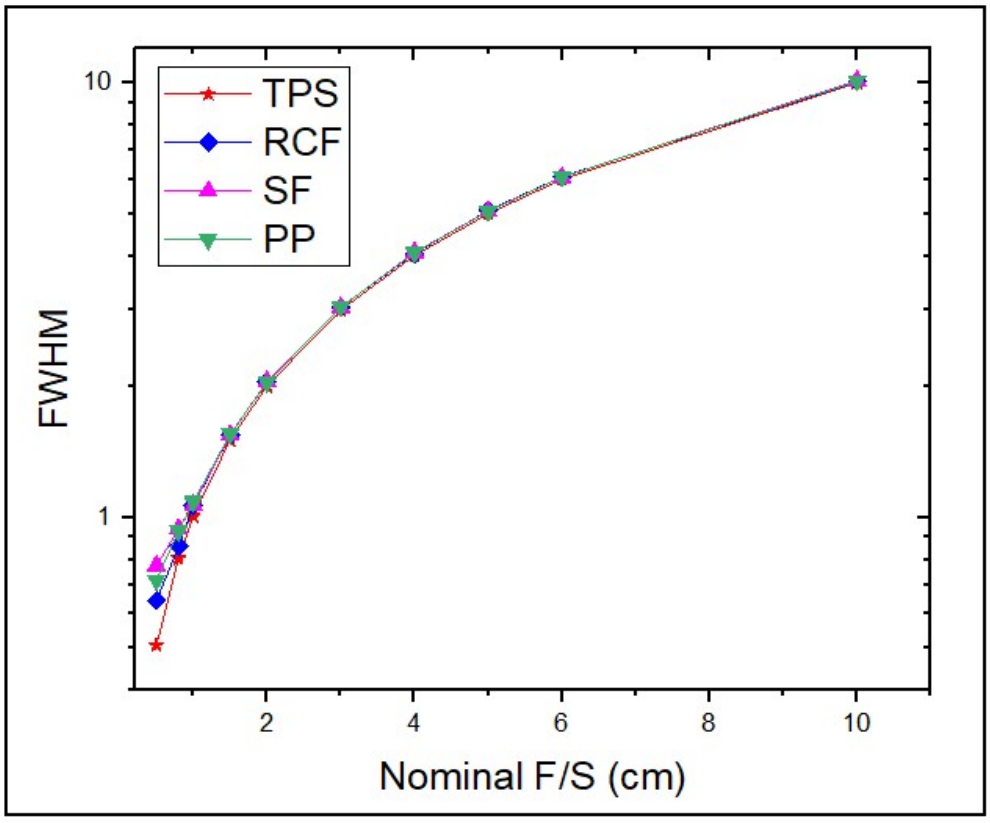

Figure 4.9: FWHM measured with various detectors in 6MV FF beam.

Figure 4.10 shows the % differences in the measured FWHM by all detectors in 6MV FF beam. The maximum difference obtained between the TPS calculated FWHM and the measured FWHM by all detectors was 34.5% for SF detector, 29.1% for PP chamber and 21% for RCF in the smallest beam size of 0.5 x 0.5 cm^2.

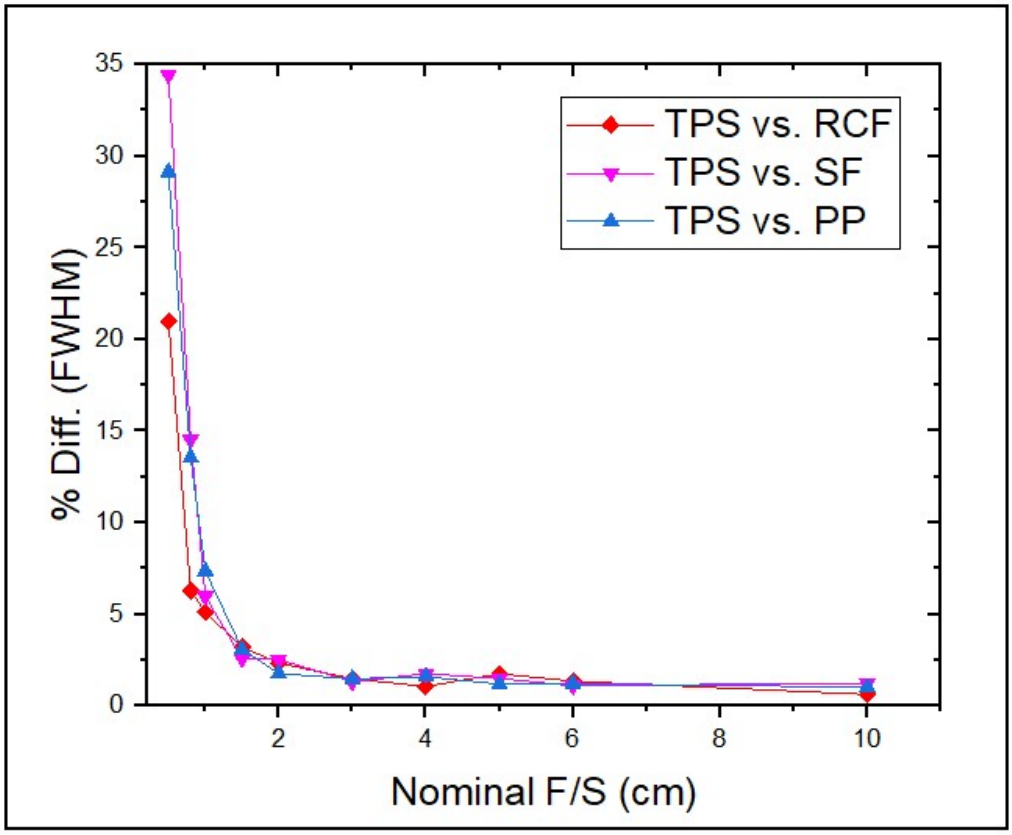

Figure 4.10: % difference of the measured FWHM in 6MV FF beam.

Flattening filters reduce the amount of head scatter component of the beam. However, in FFF beams the increased scattered radiation results in broader dose distribution at the edges of the beam. This larger penumbra region leads to a larger FWHM in the beam profile. Hence the differences in the measured FWHM between FF and FFF beams was observed.

4.2.3 FWHM for 10MV FF beam

The FWHM measured by three different detectors is shown by Figure 4.11. Consistently, the difference in FWHM increases as the field gets smaller in all three photon energies. The maximum difference observed between the measured and the calculated TPS FWHM is 0.28 cm in 10MV FF beam for the smallest F/S of 0.5 x 0.5 cm^2. The difference in the measured FWHM by all detectors was noticeable at the smallest field size of 0.5 x 0.5 cm^2. Partial source occlusion effect as well as the loss of LCPE is observed in smaller field size of 0.5 x 0.5 cm^2 in FWHM measured by all three different detectors used in this study

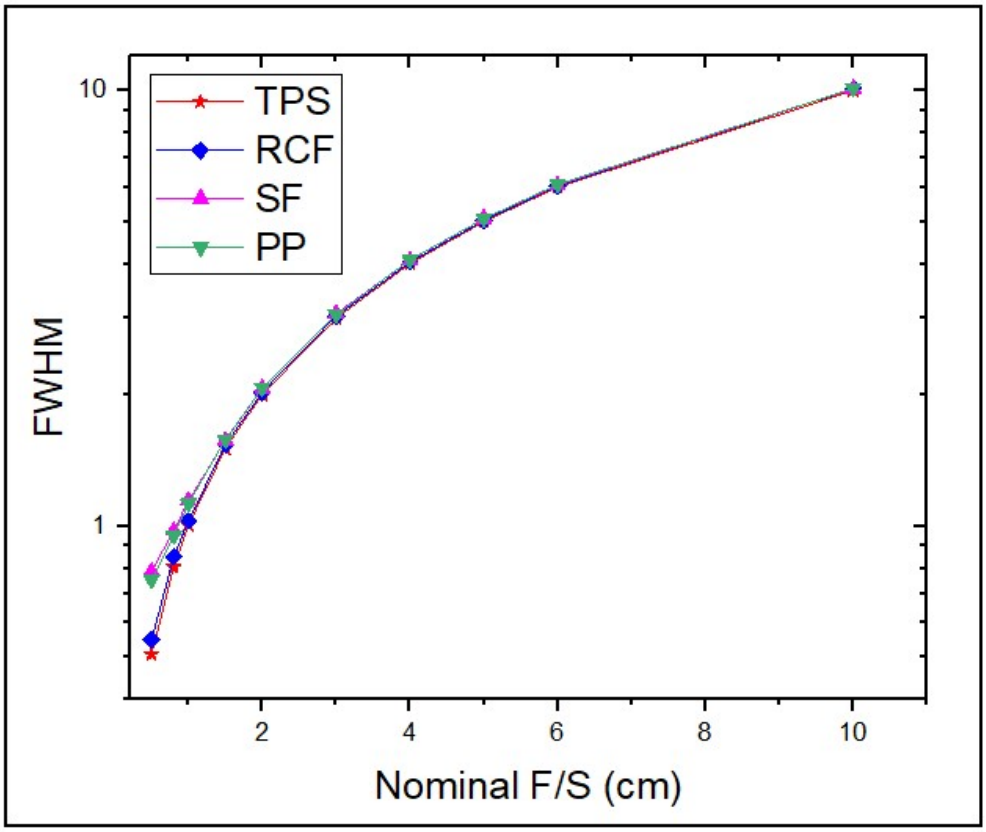

Figure 4.11: FWHM measured with various detectors in 10MV FF beam.

Figure 4.12 shows the measured FWHM % differences in 10MV FF photon beam. The maximum difference obtained between the TPS calculated FWHM and the measured FWHM by all detectors was 35.5% for SF detector, 32.5% for PP chamber and 7.3% for RCF in the smallest beam size of 0.5 x 0.5 cm^2. This was a significant decrease in % difference in the measured FWHM by RCF with an increased in photon energy.

Although the response of RFC shows a minimal energy-dependence, higher energy photons are highly penetrative and less scattered by the medium. This results in a decrease in penumbra width with increasing photon energy. Hence the difference in the measured FWHM of the beam profile with photon energy was observed.

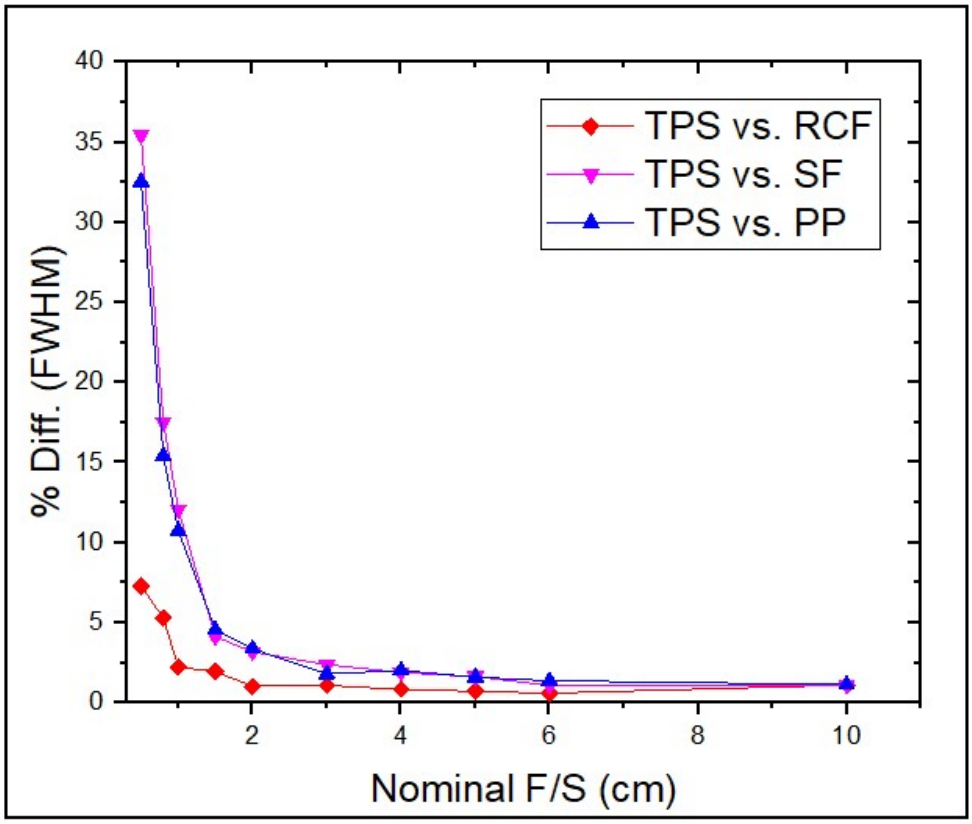

Figure 4.12: % difference of the measured FWHM in 10MV FF beam.

As showed by the figure above, the measured FWHM for a 10MV photon beam at field sizes below 8 x 8 cm^2 is overestimated by both the PTW detectors at higher photon beam.

4.3 Field output factors

Prior to field output factor (FOF) measurements, the dose per 100 MU of the linac was measured at 10 cm depth, 90 cm SSD for 10 x 10 cm^2 field with a calibrated ionization chamber. Film calibration requires a known dose rate (cGy/MU) at a given point in water phantom or solid water equivalent material for each beam energy.

Table 4.1 presents the dose delivered for 100 monitor units (MU) at a depth of 10 cm in a solid water phantom. The chamber correction factor, k_Q to convert the chamber calibration factor, $N_{D,W}$ from the Co-60 beam quality to clinical beam was below unity for all three photon beams as shown in Table 4.1 below.

Table 4.1: Solid water measurements of Elekta Versa HD linac under reference conditions: 10 x 10 cm^2, 10 cm depth, and 90 cm SSD.

Energy (MV)	$TPR_{20,10}$	k_Q	Linac (cGy/MU)
6 FFF	0.674	0.9908	0.8129
6 WFF	0.676	0.9905	0.8041
10 WFF	0.733	0.9814	0.8858

The machine output (Gy/MU) shown in the above table was used to determine the MU to be delivered to a film.

The beam quality specification ($TPR_{20,10}$) for a reference field size of 10 x 10 cm^2 is determined by the ratio of the chamber reading measured at a depth of 20 cm and 10 cm in a solid water phantom. Values of the $TPR_{20,10}$ were compared with the commissioning data, see Table 4.2 below.

Table 4.2: Verification of the measured beam quality index under reference conditions: 10 x 10 cm^2, 10 cm depth, and 20 cm depth at both 90 cm SSD and 80 cm SSD.

Energy (MV)	$TPR_{20,10}$ [Measured]	$TPR_{20,10}$[Commissioning]	% Diff.
6 FFF	0.674	0.678	0.590
6 WFF	0.676	0.686	1.458
10 WFF	0.733	0.737	0.543

The dose rate calculated by the TPS is compared to the Linac output measurements under the same geometry and the results are shown in Table 4.3 below.

Table 4.3: Comparison between the calculated TPS and Linac measured dose rate.

Energy (MV)	Linac (cGy/MU)	TPS (cGy/MU)	% Diff.
6 FFF	0.813	0.829	1.93
6 WFF	0.804	0.818	1.71
10 WFF	0.886	0.901	1.66

The percentage difference between the measured and the calculated dose rate was found to be well within 2%.

4.3.1 Lateral charged particle equilibrium radius

The radius of the lateral charged particle equilibrium r_{LCPE} is determined for all the volumetric detectors to be used in small photon field output factor measurements. The radius of LCPE for each photon energy based on the beam quality was determined by using the following equation [20]:

$$r_{LCPE} = 8.369 * TPR_{20,10}(10) - 4.382 \tag{4.2}$$

Where $TPR_{20,10}$ (10) is the tissue-phantom ratio, also known as beam quality index, measured at 10 x 10 cm^2 field size. The relationship between the detector radius and the lateral distribution of charged particles depends on the beam quality of the incident radiation. Therefore, the required chamber radius is calculated using equation 4.2 to establish the LCPE.

Table 4.4 below presents the two PTW ionization chamber specifications used in this study.

Table 4.4: PTW ionization chamber specifications used for measurements

Ionization chamber	V [cm^3]	R [mm]	L [mm]	t [g/cm^2]
PTW 30013 Farmer type	0.60	3.05	23.0	4.55
PTW 31021 Semiflex 3D	0.07	2.40	4.80	0.084
PTW 31014 Pinpoint	0.015	1.00	5.00	0.085

The chamber to be used for FOF measurements depends on the FWHM measured at a depth of 10 cm for each field size, and the relationship is expressed by the following expression[20]:

$$FWHM \geq 2 * r_{LCPE} + d \tag{4.3}$$

Where d is the extended dimensions of the chamber in either the longitudinal direction or radial direction and depends on the cavity length, cavity radius, and wall thickness. In the longitudinal direction, d is determined as follows:

$$d = L + t \tag{4.4}$$

L refers to the length of the sensitive volume, and t is the thickness. Whereas in the radial direction of the chamber, d is calculated as follows:

$$d = 2 * (r + t) \tag{4.5}$$

r refers to the radius of the chamber's sensitive volume. Table 4.5 shows the calculated r_{LCPE} for three photon beams.

Table 4.5: Calculated r_{LCPE} for all three photon beams.

Energy (MV)	$TPR_{20,10}$ [Measured]	r_{LCPE}[cm]
6 FFF	0.674	1.259
6 WFF	0.676	1.275
10 WFF	0.733	1.753

As illustrated in the above table, the radius of the LCPE increases with an increase in photon energy. Tables 4.6, 4.7, and 4.8 show the calculated FWHM in three photon beams for the three volumetric detectors used in this study.

Table 4.6: Calculated 6MV FFF FWHM for different detectors.

Ionization chamber	2^*r_{LCPE} [cm]	d[cm]	FWHM [cm]
PTW 30013 Farmer type	2.517	2.755	5.272
PTW 31021 Semiflex 3D	2.517	0.780	3.297
PTW 31015 PinPoint	2.517	0.800	3.317

Table 4.7: Calculated 6MV FF FWHM for different detectors.

Ionization chamber	2*r_{LCPE} [cm]	d[cm]	FWHM [cm]
PTW 30013 Farmer type	2.551	2.755	5.306
PTW 31021 Semiflex 3D	2.551	0.780	3.331
PTW 31015 PinPoint	2.551	0.800	3.351

As per the calculated FWHM in Tables 4.6 and 4.7 the recommended field size for both Semiflex 3-D and PinPoint is $\geq$ 3 x 3 cm^2. According to the PTW manufacturer's catalog these two chambers can measure the minimum field size of 2 x 2 cm^2.

Table 4.8: Calculated 10MV FF FWHM for different detectors.

Ionization chamber	2*r_{LCPE} [cm]	d[cm]	FWHM [cm]
PTW 30013 Farmer type	3.505	2.755	6.260
PTW 31021 Semiflex 3D	3.505	0.780	4.285
PTW 31015 PinPoint	3.505	0.800	4.305

According to the calculated FWHM as shown in table table 4.8 above for 10MV WFF higher energy photon, it is recommended to use farmer type chamber for field size $\geq$ 6 x 6 cm^2.

4.3.2 Radiochromic film calibration

As illustrated in Figure 4.13, small pieces of films cut in rectangular shapes of approximately 2 x 25 cm^2 and exposed to known doses with 6MV photon beam. Film darkness increases with the absorbed dose ranging from 0 Gy up to 20 Gy:

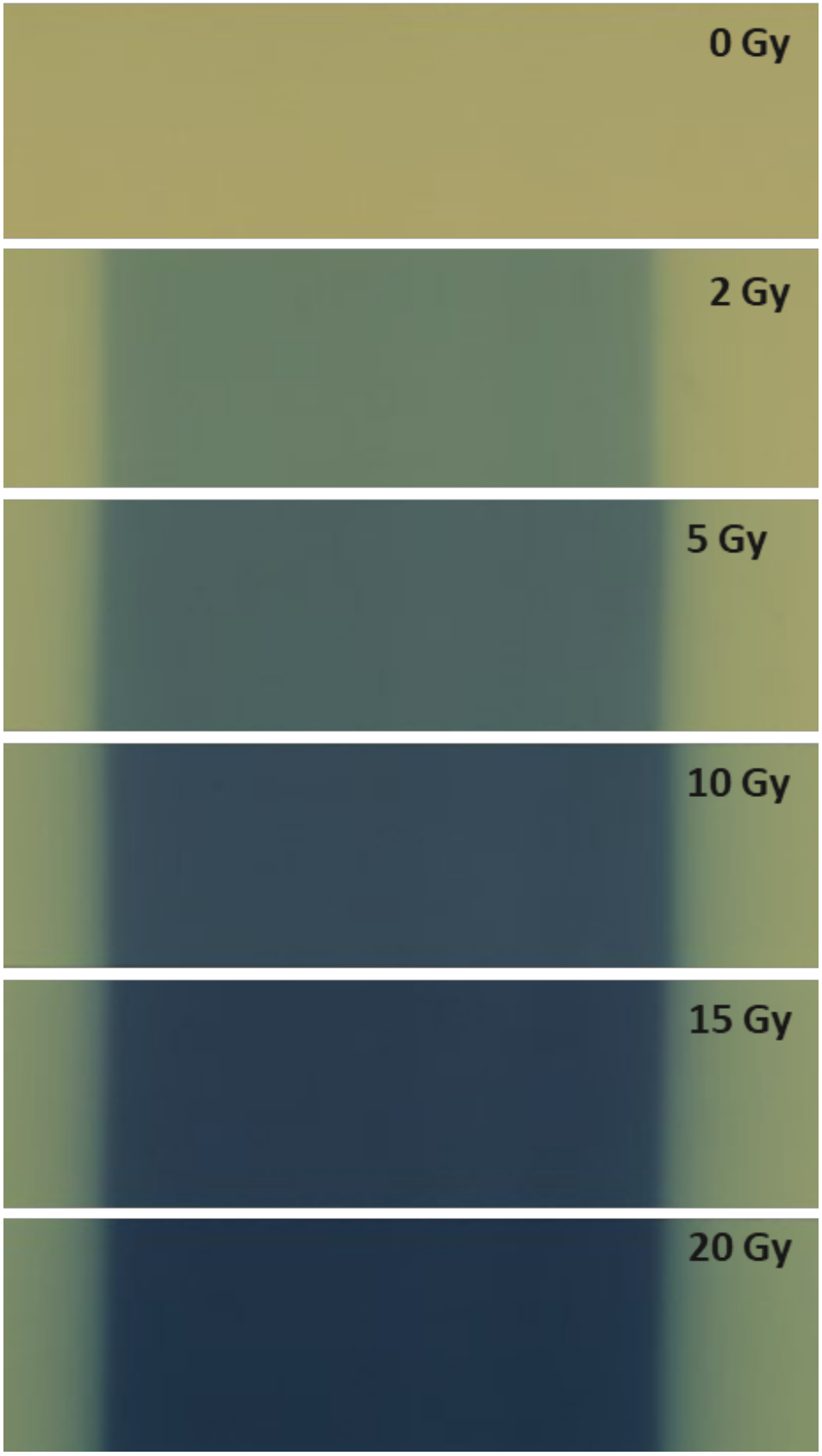

Figure 4.13: Images of the exposed films scanned using Epson scanner and saved in tiff format.

The dose-response curves for the GAFchromic EBT3 films produced using imageJ software are shown in the Figure 4.14 within the dose range of up to 8 Gy. A good fit was obtained using a simple second-order polynomial in origin for all three color channels: red, green, and blue.

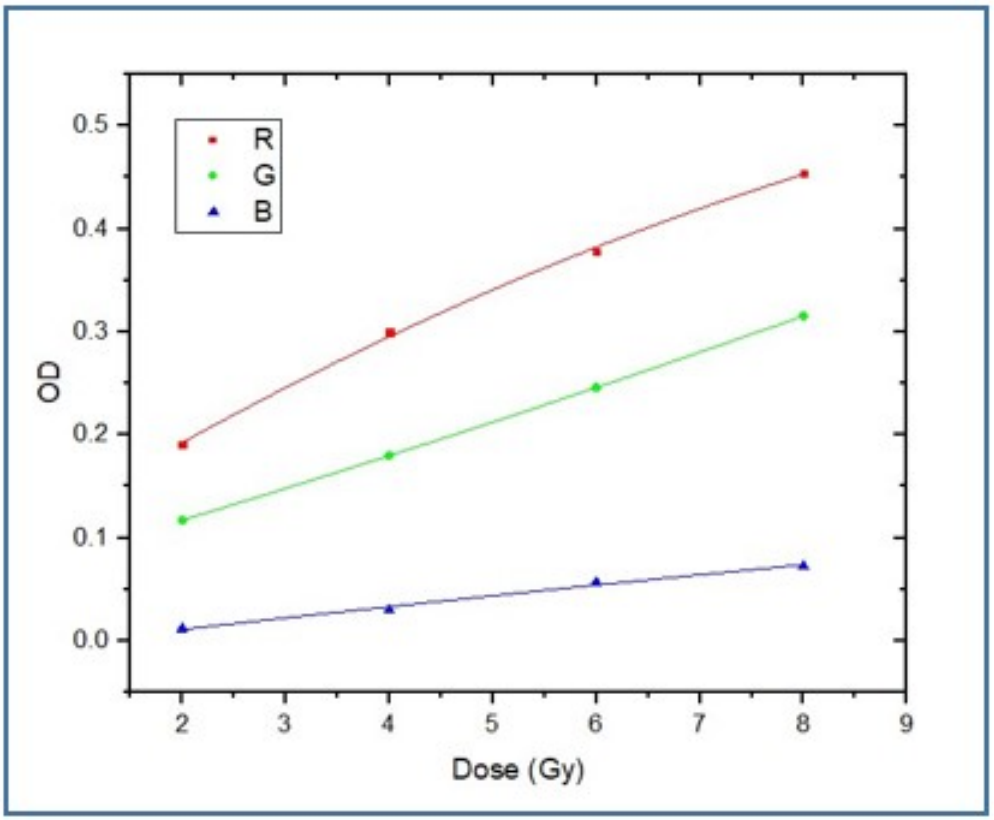

Figure 4.14: OD as a function of dose for the EBT3 film for all three different color channels: red, green and blue in 6MV photon energy.

The optical density for the blue colour channel is less sensitive to the increase in radiation dose. This behaviour was observed for all the three photon energies. However, dosimetry with all three colour channels is recommended depending on the clinical dose range that the film will be used for.

The red colour channel is highly sensitive to the absorbed dose compared to the other two channels. Hence, dosimetry was only done using the red colour channel with ImageJ software for all the three photon energies.

4.3.3 Absorbed dose and energy dependence of RCF

The response of the red colour channel with dose reaches a saturation point in higher doses. As per the specifications of the EBT3 film, the dose range is

from 0.1 Gy up to a maximum dose of 20 Gy. Figure 4.15 shows the mean grayscale of red color channel as a function of dose for all three photon energies. As illustrated by the figure below, RCFs were verified to be sensitive to the radiation dose. Film response decreased with an increased in dose. However, its response remain stable with an increase in photon energy from 6MV to 10MV.

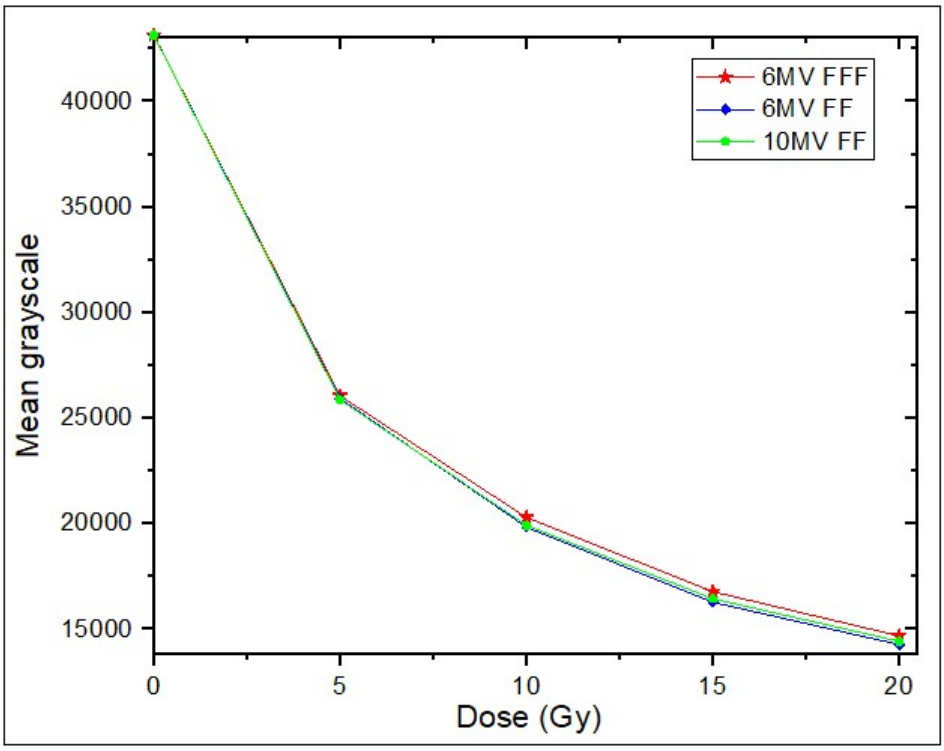

Figure 4.15: Response of EBT3 film with an increased in dose and photon energy

The red colour channel reaches the saturation point at higher doses beyond the 20 Gy level. Stereo-tactic radiosurgery uses doses beyond 20 Gy per fraction. The red channel shows no response in higher doses of 20 Gy; therefore it is important to characterize and validate the dose-response of the radiochromic film prior to any dosimetric application.

4.3.4 Dose response curves

Calibration curves of the film were obtained using 6MV FFF, 6MV FF, and 10MV FF photon energies. Rodbard function from ImageJ software was used to fit the EBT3 films in this study as shown by Figures 4.16, 4.17, and 4.18. Rodbard fitting model used with R^2 approximately equal to one.

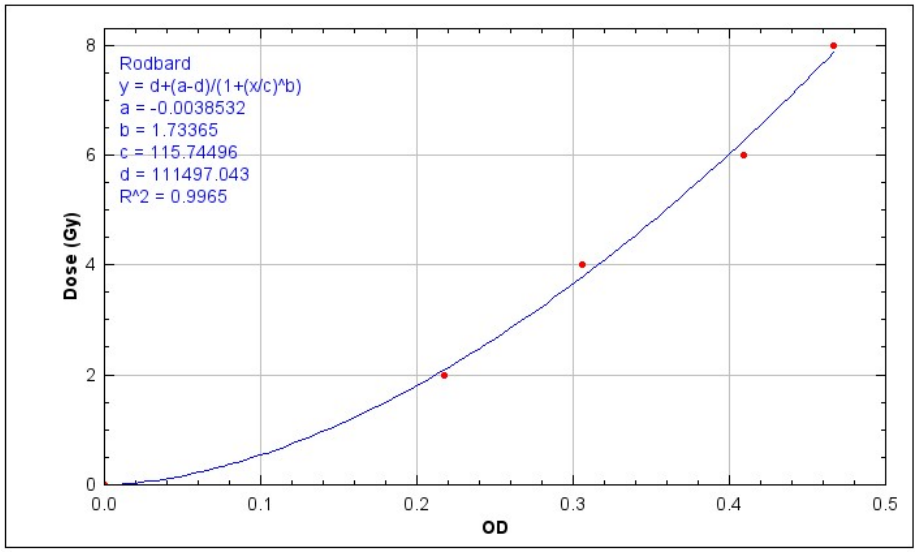

Figure 4.16: Optical density as a function of dose in 6MV FFF beam.

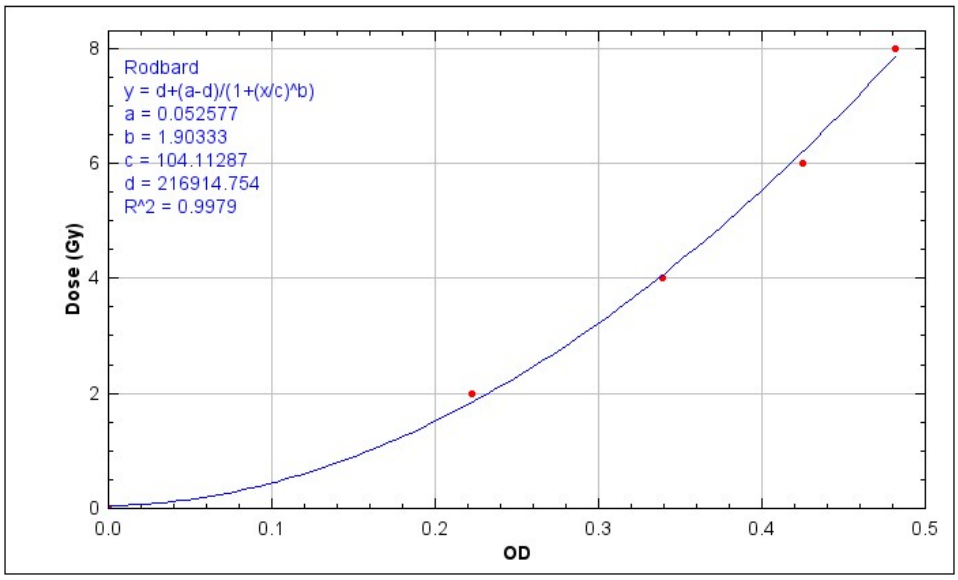

Figure 4.17: Optical density as a function of dose in 6MV FF beam.

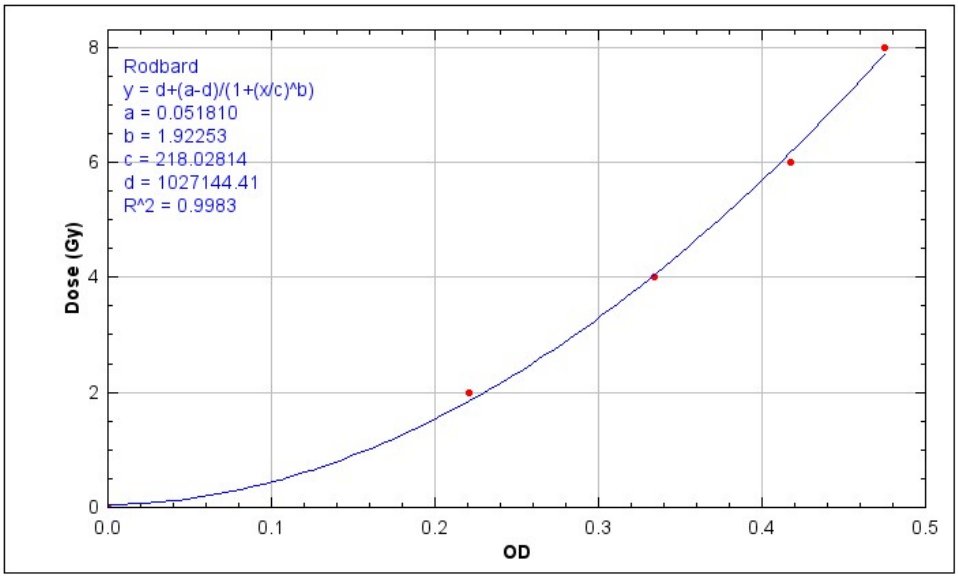

Figure 4.18: Optical density as a function of dose in 10MV FF beam.

The calibration curves established were used for all film dosimetry measurements since they were from the same batch. Mean pixel values were converted to OD from these calibration curves to plot beam profiles for films.

The above curves were used for all film dosimetry measurements in this study. The relationship between the dose and the mean gray scale values was determined by using Rodbard fitting function, and the dose was calculated by using the following equation:

$$y = c\left(\frac{x-a}{d-x}\right)^{1/b} \tag{4.6}$$

Where y is the absorbed dose calculated from the OD, x is the optical density of the film determined from the mean gray scale , and a, b, c, and d are the parameters obtained from the fit. The parameters a, b, c, and d used in fitting the curve are shown in each figure above (Figures 4.12 to 4.14). Equation 4.7 was used to convert the mean grayscale to dose or OD.

4.3.5 EPIQA configuration results

As per EPIQA manual, in the configuration process, the first step is to acquire the primary radiation without any attenuating material between the source and the EPID. Secondly, the images for MLC transmission were acquired. Thirdly, the ionization chamber measurements were performed to give a known dose to

the flat panel. Therefore, the total dose for each field size is calculated from both the primary radiation dose and MLC transmitted dose. The EPIQA configuration program was used to produce the results presented in this section.

Primary dose angular coefficient results are illustrated in Figs 4.19 and 4.20. Dose calibration factor (MU/Gy) for ionization chamber measurements performed at 10 cm depth in a solid water phantom is shown in Figs 4.21, and 4.22 for all three photon energies. The set-up for ionization chamber measurements was performed at 10 cm depth to match the EPID calibration point. Good data fit was obtained for all three photon beams.

Figs 4.23, and 4.24 present EPID output factor curves. The EPIQA software obtained a perfect fit for EPID measurements in all three photon beams.

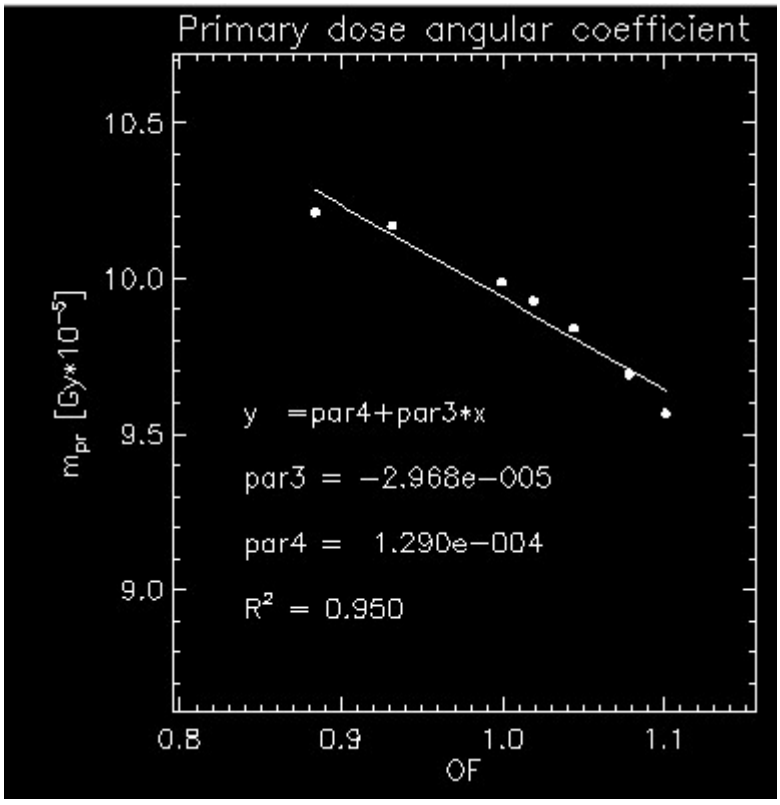

Figure 4.19: Primary dose angular coefficient fitting results in 6MV FF beam.

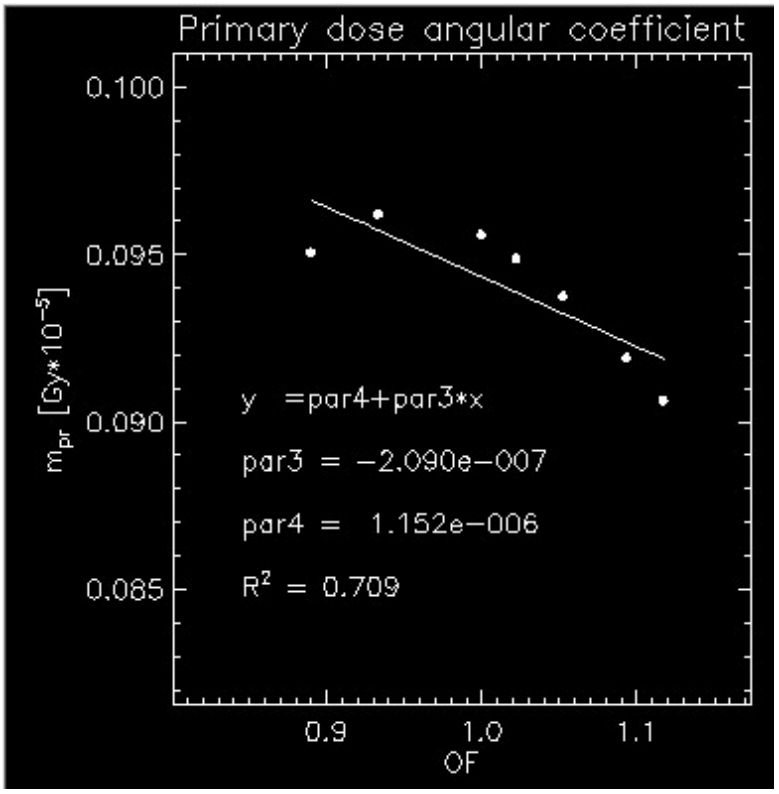

Figure 4.20: Primary dose angular coefficient fitting results in 10MV FF beam.

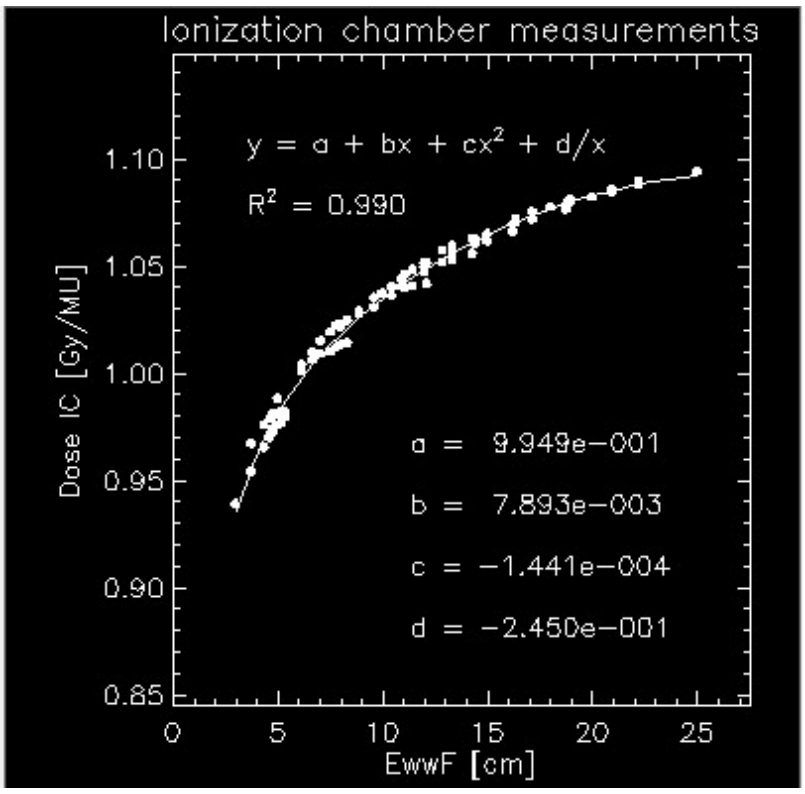

Figure 4.21: Ionization chamber data fitting results in 6MV FF beam.

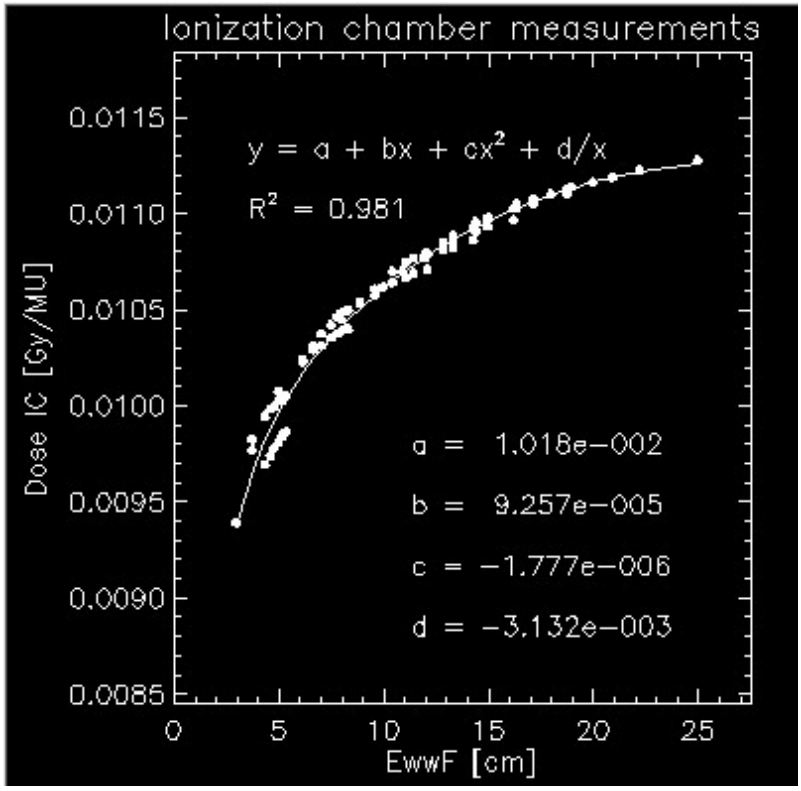

Figure 4.22: Ionization chamber data fitting results in 10MV FF beam.

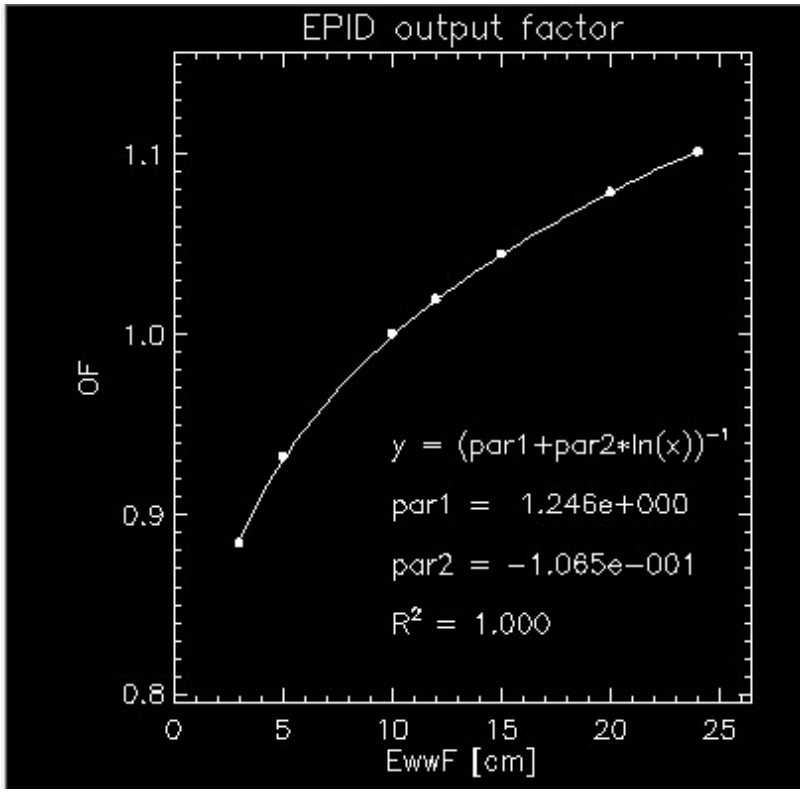

Figure 4.23: EPID output factor fitting results in 6MV FF beam.

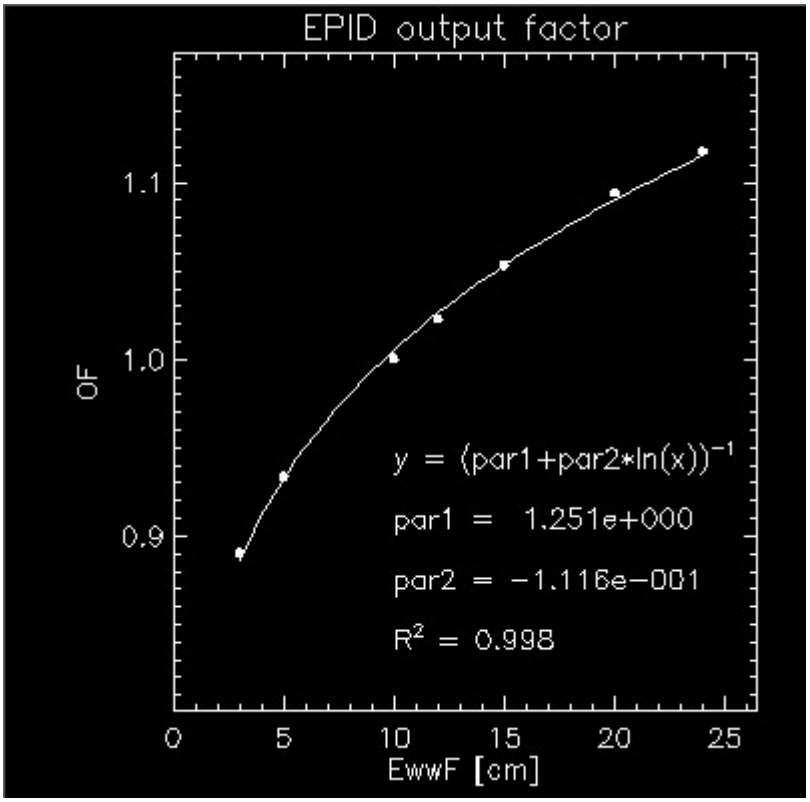

Figure 4.24: EPID output factor fitting results in 10 MV FF beam.

The calibration parameters shown by the curves above are necessary to configure the EPIQA algorithm for future EPID dosimetry purposes. In order to use the EPID for FOF measurements, the following data: primary and transmitted calibration images, ionization chamber data, and EPID output factor was acquired for two photon beam energies.

4.3.6 Measured field output factors

The response of various detectors was evaluated down to a very small field size of 0.5 x 0.5 cm^2 under the same reference conditions but different material media, water versus solid water. Figs 4.25, 4.26 and 4.27 illustrate the FOF measured with radiochromic film (EBT3 type) compared with FOF computed by the TPS at 10 cm depth. For CPE to exist, scatter around the chamber is required. So, as the field size is reduced, there is less contribution from the scatter component into the chamber volume; hence the rapid decrease in FOF is observed in field sizes below 1 x 1 cm^2. Also, the actual source is obscured in smaller fields less than 1 x 1 cm^2. This results in reduced beam intensity

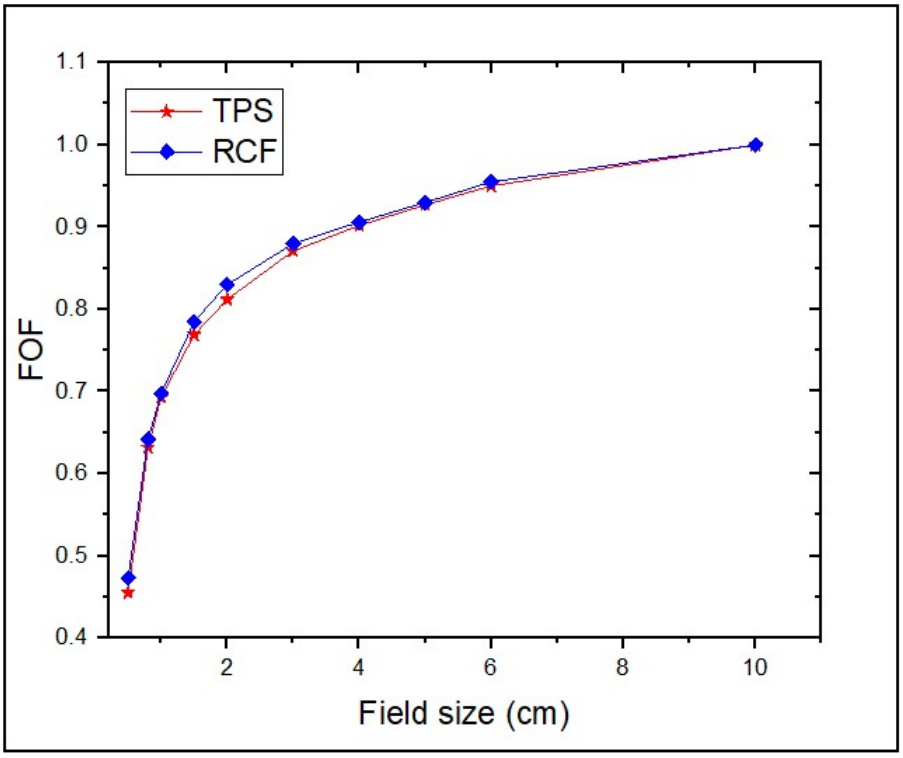

Figure 4.25: FOF results for EBT3 vs TPS data in a 6MV FFF beam.

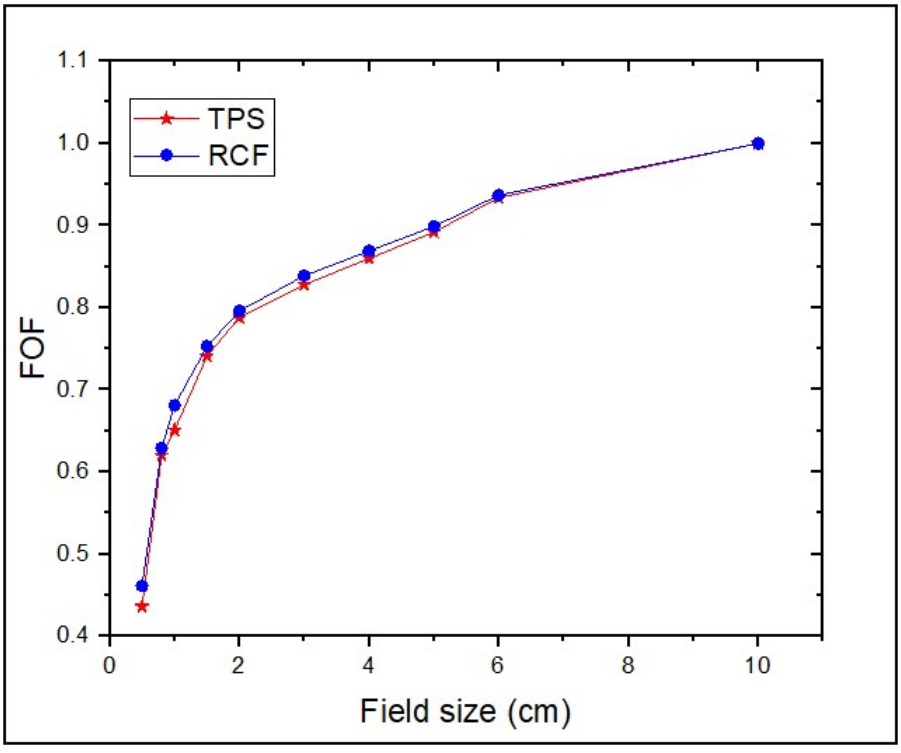

Figure 4.26: FOF results for EBT3 film vs. TPS data in a 6MV FF beam.

Film was found to be an appropriate detector for small field size measure-

ments. This is due to its higher spatial resolution. For 6MV FF beam, the FOF measured with a radiochromic film (RF) and FOF computed by TPS are in good agreement except for field sizes ranging from 0.5 x 0.5 cm^2 to 1 x 1 cm^2. The difference is well within 0.06%.

For both 6MV energy beams, the FOF is closer to the treatment planning values. Therefore, film was found to be suitable for all the measured field sizes.

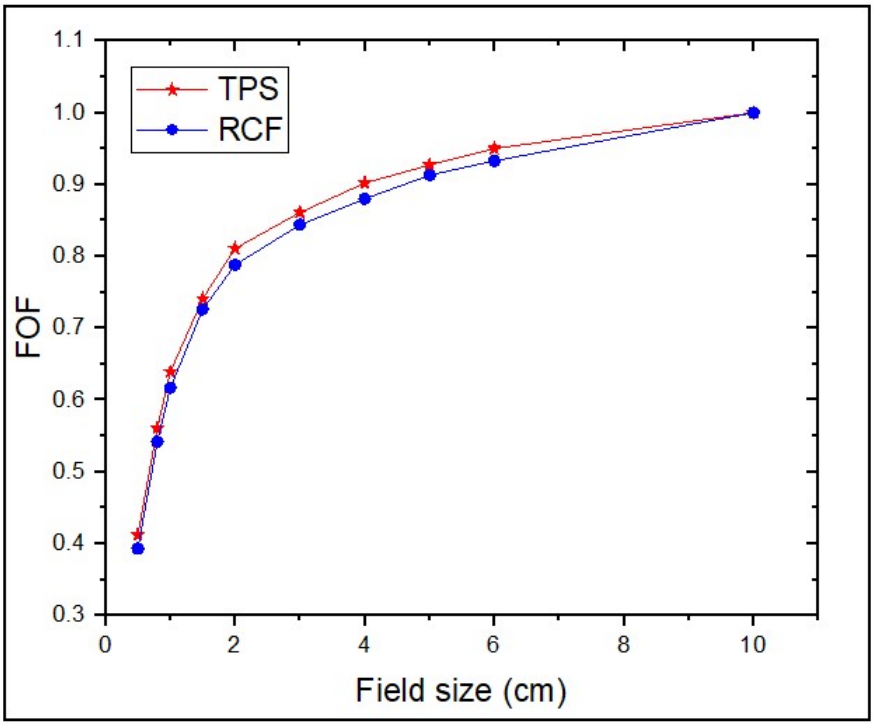

Figure 4.27: FOF results for EBT3 film vs. TPS data in a 10MV FF beam.

Notable variation in FOF values with 10 MV WFF beam was observed in fields ranging from 2 x 2 cm^2 to 6 x 6 cm^2 for the TP system against EBT3 film. This is due to uncertainties associated with film protocol, namely: film handling, irradiation, scanning, and analysis. This is illustrated by Figure 4.27 above.

The calculated TPS and the measured EBT3 FOF do not agree in a higher photon energy beam (10MV FF), as shown in Figure 4.27 for all beam sizes. The FOF values measured with EBT3 film are less than the calculated TP system data. Minimal variation in film response to different photon energies, the accuracy of the TPS mathematical models or algorithms and uncertainties in calibration for 10MV FF beam might have led to the observed discrepancies

between the measured FOFs and the TPS data.

The EBT3 film was then tested against two ionization chambers and a-Si EPID. FOF measured with different detectors is shown in Figs 4.28, 4.29, and 4.30 below. For a bigger detector size, less signal is measured in smaller field sizes due to volume averaging effect. Therefore, FOF is reduced.

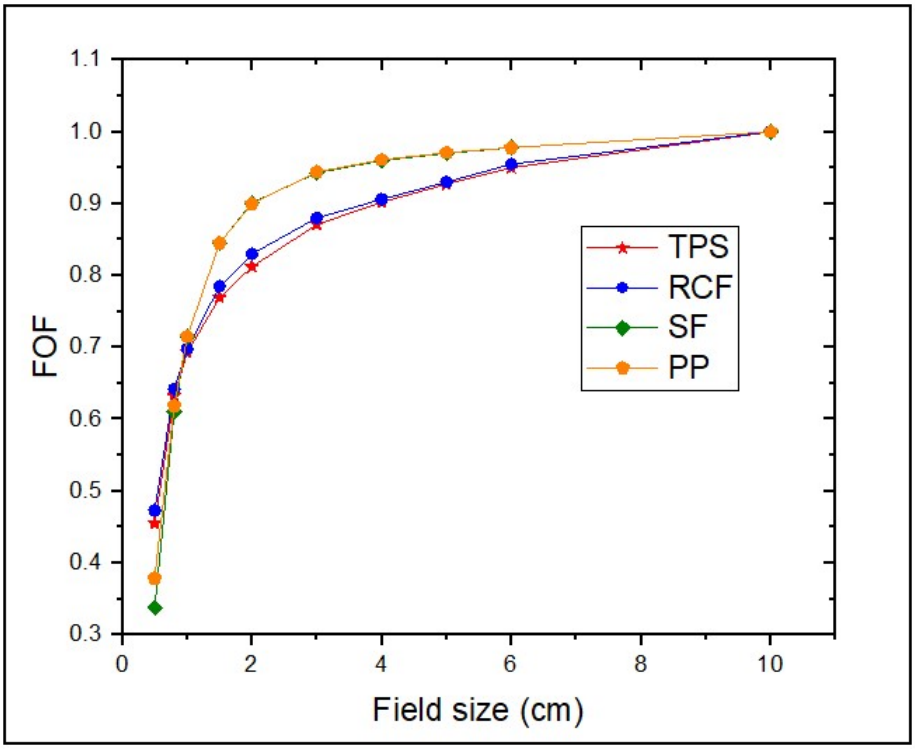

Figure 4.28: EBT3 film FOF compared to ICs FOF in 6MV FFF beam.

The a-Si EPID could not be used for FOF measurements in the 6MV FFF beam in this study, EPID's response showed very strong energy dependence.

The rapid decrease in FOF is much more pronounced in field sizes below 2 x 2 cm^2 irrespective of the photon energy used for irradiation. Compared to other detectors, the signal produced by EBT3 film is not significantly affected by the reduction in field size due to its high spatial resolution.

Misalignment of the volumetric detectors in smaller field sizes is much larger compared to the RC film. Positioning uncertainty in EBT3 film measurements is very minimal. Hence the distinction between the FOF measured with RC film FOF and TPS is very reasonable.

It should be noted that the two PTW ionization chambers used in this study are not recommended for determining FOF in small fields. Pinpoint chamber should not be used for field sizes smallers than 1 x 1 cm^2. Therefore, Table 26 from the IAEA TRS-483 does not provide FOCF for a PTW 31014 PinPoint detector [9].

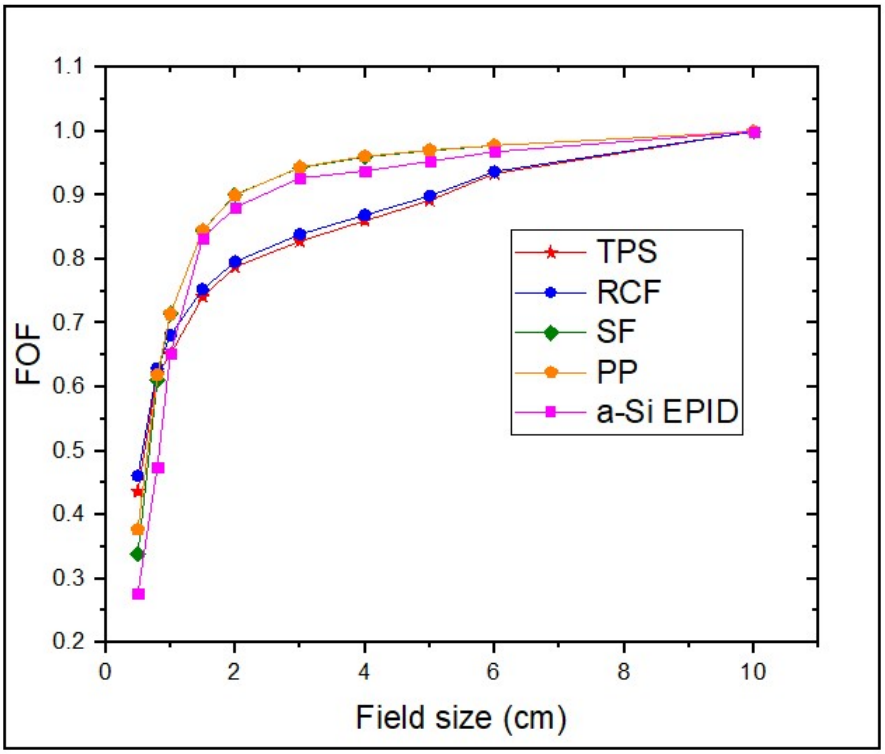

Figure 4.29: EBT3 FOF compared to ICs FOF and EPID in a 6MV FF beam.

The measured FOF with PinPoint, Semiflex chambers, and the EPID is larger than the FOF measured with EBT3 film and computed by TPS for beam sizes above 1 x 1 cm^2 for all three photon energies.

As discussed in section 4.3.2, the detector radius affects LCPE within the detector material. In a larger chamber radius, charged particles travel longer path length and therefore deposit more energy within the detector, resulting in more FOF values measured. PTW ionization chambers with relatively high radii are assumed to produce accurate results in field sizes larger than 2 x 2 cm^2 [54]. However, RCF with high spatial resolution has some limitations in terms of variation in response, handling, and appropriate calibration procedures.

There is a large difference in the smallest field (0.5 x 0.5 cm^2) between the a-Si EPID's response and the other detectors in the 6MV FF beam, followed by a PTW Semiflex 3-D chamber. As shown by the Figs 4.28, 4.29, and 4.30 for all three photon energies, TPS and RCF underestimate the true value of the FOF at field sizes greater than 2 x 2 cm^2.

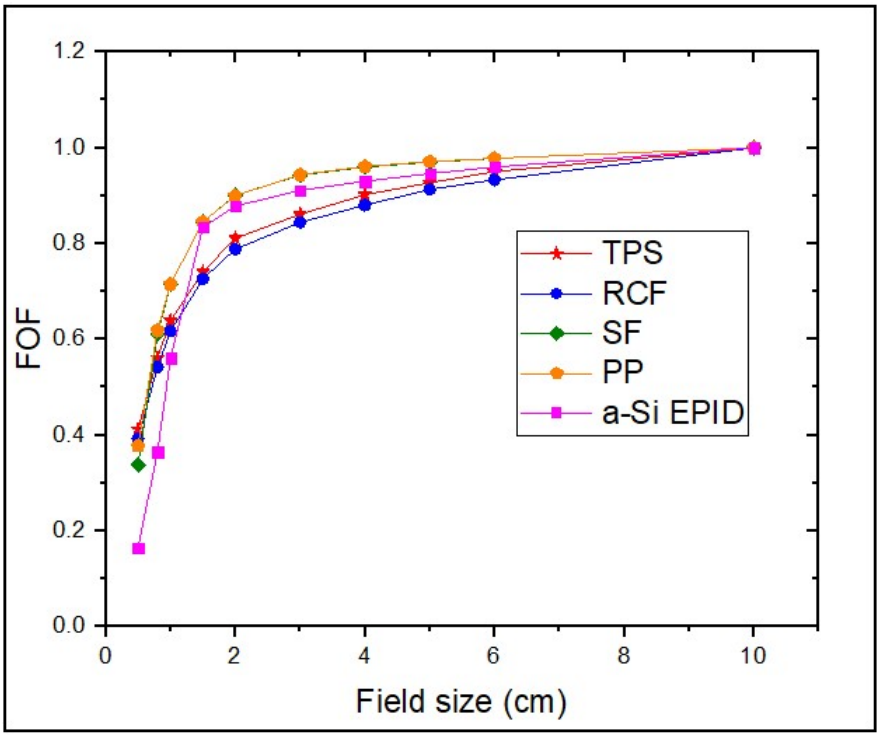

Figure 4.30: EBT3 FOF compared to ICs FOF and EPID in a 10MV FF beam.

As shown by the results obtained in the Figures above, the FOF is reduced in smaller fields $\leq$ 2 x 2 cm^2 due to the collimator system's partial occlusion of the primary photon source. Also, the influence of scattering decreases with field size, hence the loss of LCPE is observed in smaller field sizes [77].

The dose measured by the ionization chamber in narrow beams is underestimated in the central axis due to the volume averaging effect. This effect is observed for field sizes below 2 x 2 cm^2 in both volumetric detectors, PTW 31014 Pinpoint and PTW 31021 3-D Semiflex. Thus, the signal produced by these two detectors is directly related to their collecting volumes. The detector-sensitive volumes are large compared to the beam dimensions.

Values of the measured FOF with EBT3 film are compared with the published

data [42]. Figs 4.31, 4.32, and 4.33 show the comparison results between the data obtained in this study with the published data.

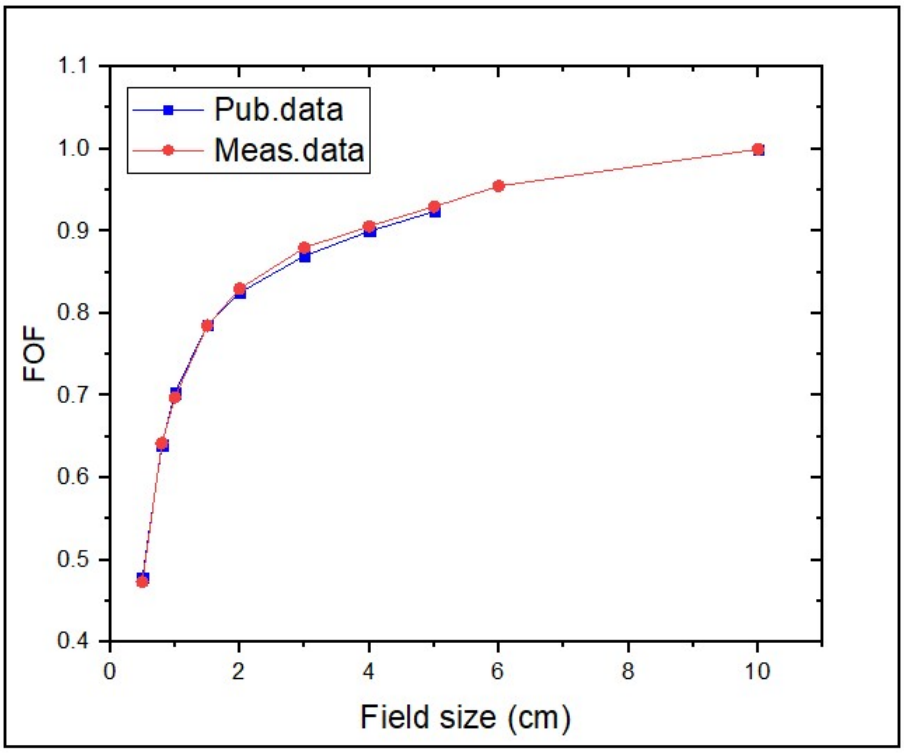

Figure 4.31: Measured FOF with EBT3 compared to the published data by Casar et al (2018) in a 6MV FFF beam.

As shown in Figure 4.31 above, the results obtained for the field output factor between the measured data and the data obtained by Casar et al (2018) show a good agreement for all the field sizes.

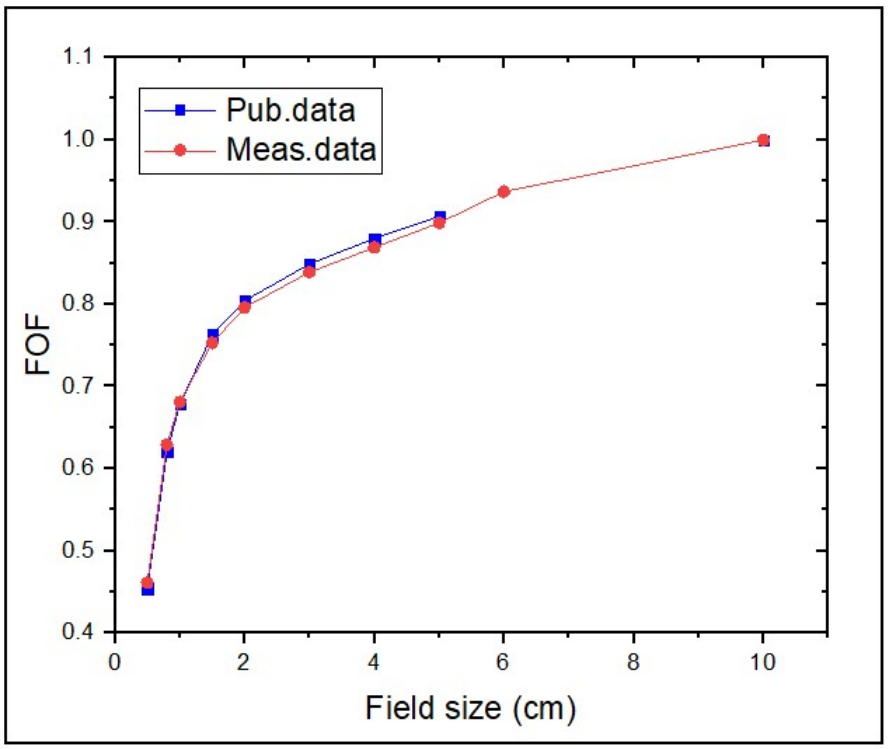

Figure 4.32: Measured FOF with EBT3 compared to the published data by Casar et al (2018) in a 6MV FF beam.

Comparison between FOF measured with EBT3 film in this study and the data published by Casar et al (2018) showed a good agreement in 6MV FF beam for all beam sizes. consequently, fairly good agreement between the measured and the published data is shown by all three photon energies.

The large variation between the FOF measured with the two volumetric detectors (3-D semiflex and Pinpoint) and RCF at field sizes above 2 x 2 cm^2 may be due to experimental uncertainties in the set-up.

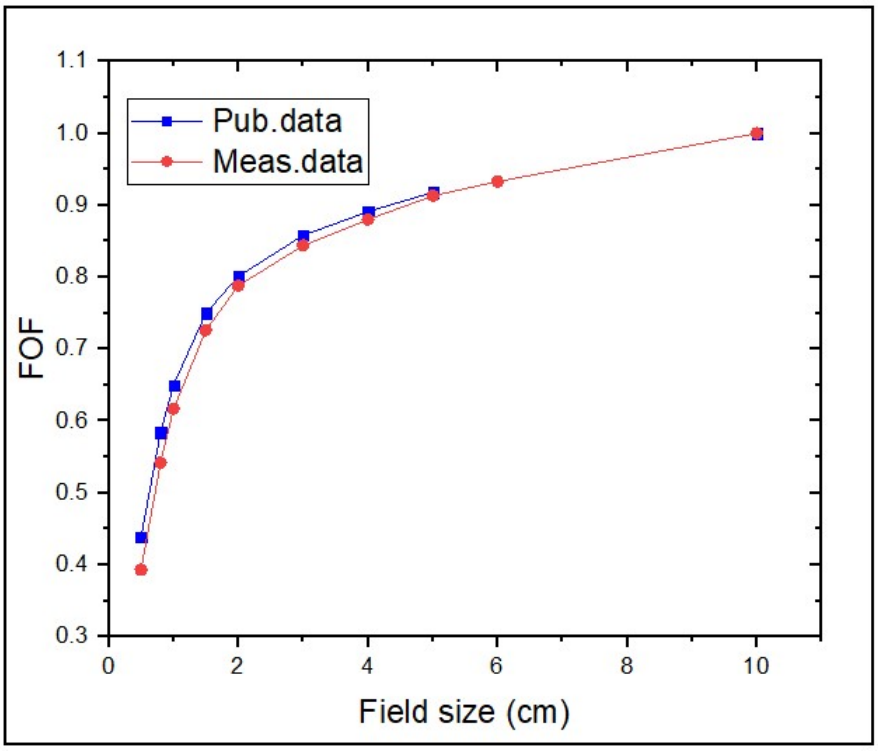

Figure 4.33: Measured data vs. the published data by Casar et al (2018) in a 10MV FF beam.

As shown by Figure 4.33 above, FOF measured with EBT3 film in a 10MV FF beam is compared with the published data, and the response of EBT3 film was found to be lower than the corresponding energy 10MV FF. This low response of RC film led to a significant difference in measured FOF compared to the planning data in all the field sizes in the 10 MV FF beam.

4.3.7 Energy dependence of the FOF with EBT3 film

Electrons created by photons move in all different directions. For higher photon energy beams, the lateral distance traveled by the charged particle is much longer within the field and in the field borders. As a result, these electrons contribute less dose in smaller field sizes which cause a decrease in the FOF with energy. A direct comparison between measured and published data using EBT3 film is shown in Figure 4.34. The figure below illustrates the variations in RCF response to different beam energies and field sizes.

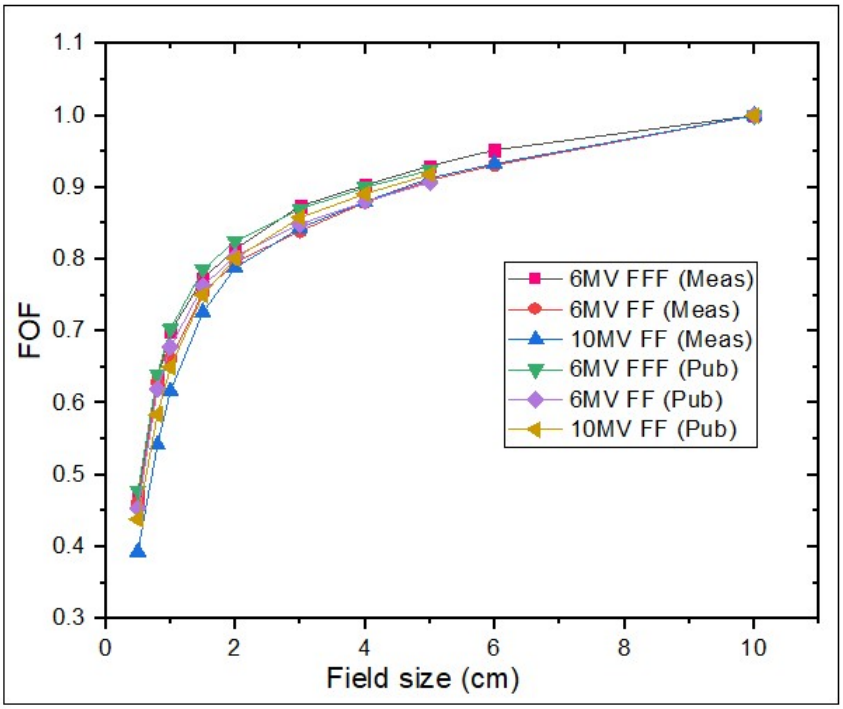

Figure 4.34: Variation of FOF with photon energy between measured and published data using EBT3 film.

As the beam energy increases, the electron range increases leading to the significant reduction in FOF measured by high energy photon beam (10MV FF beam). In addition, the increase in electron range causes a break free from the interaction point.

The published data was obtained from Casar et al 2019 [42]. The dose contributed by the laterally scattered electrons decreases with an increase in the energy of the photon beam. The non-equilibrium effect leads to a significant drop in FOF for small beams as shown by Figure 4.34 for the measured and published data.

A flattening filter reduces the dose rate but increases the scattered photons. Hence the dose is lower in both 6MV FF and 10MV FF beams compared to the unhardened beam (6MV FFF).

4.3.8 Percentage differences in measured FOF

The calculated % difference of the measured FOF with different detectors for 6MV FFF, 6MV FF, and 10MV FF beams are shown in Figures 4.35, 4.36, and 4.37 below. A big deviation is observed for both ionization chambers as

the field size is reduced. This behaviour is exactly the same in all three photon energies.

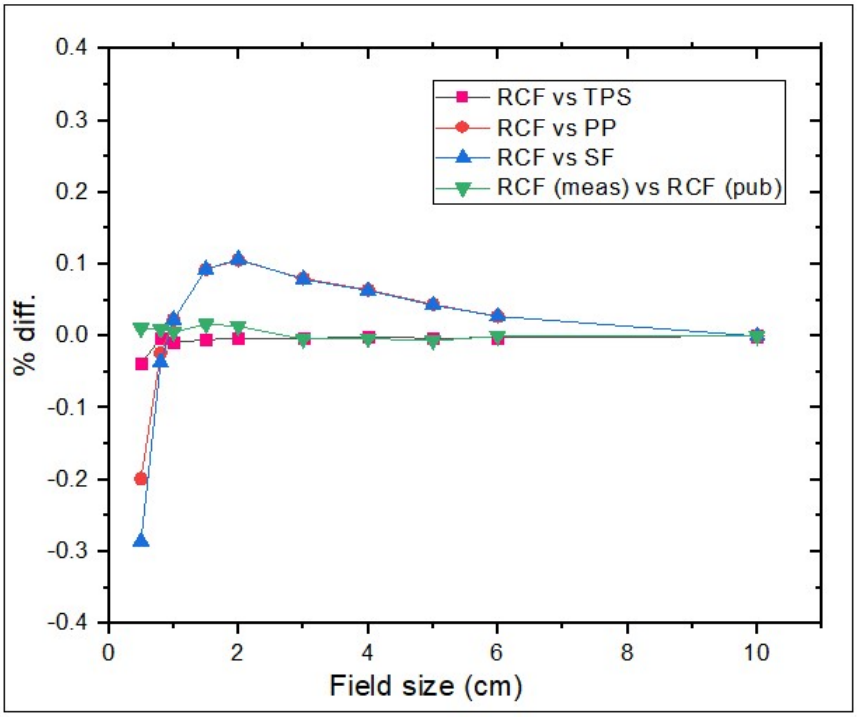

Figure 4.35: Variations in the measured FOF with different detectors used in small photon fields for 6MV FFF beam.

The percentage (%) difference observed is well within 0.3 between the TPS data and Semiflex 3D chamber. The percentage difference in all three photon energies increases further from zero percent for field sizes below 2 x 2 cm^2. PTW simiflex has a bigger sensitive volume compared to film and Pinpoint detectors. Hence there is a large % difference between the chamber and the computed TPS data.

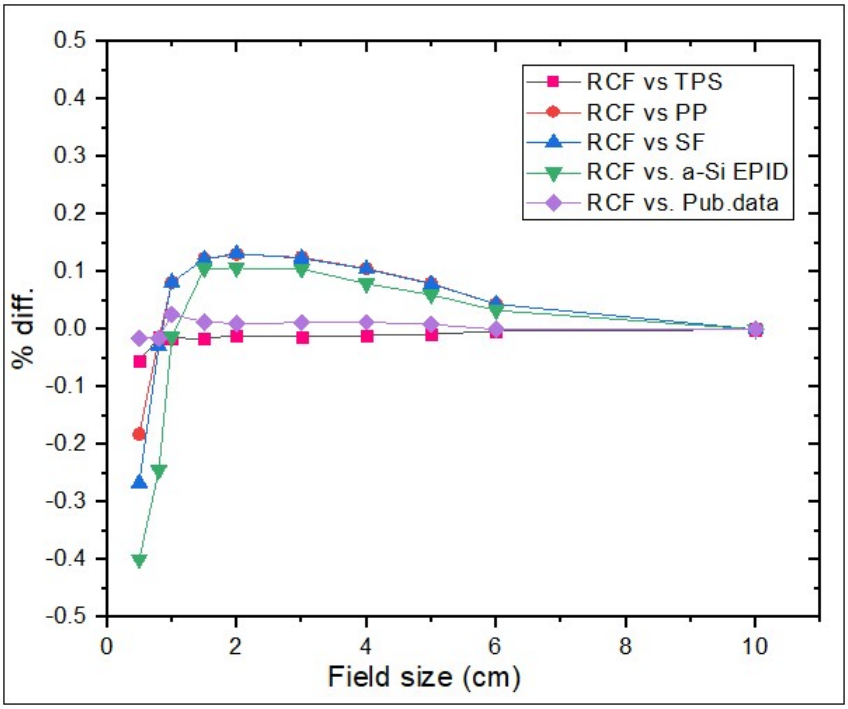

Figure 4.36: Variations in the measured FOF with different detectors used in small photon fields for 6MV FF beam.

As the field size decreases below 2 x 2 cm^2, the points start to spread out as shown by all three graphs, Figs 4.35, 4.36, and 4.37 respectively. The same behavior is observed in all three photon energies, flattening filter-free beam and the other two flattened beams. The penumbra for small fields becomes very large and overlap with the primary photon fluence. This overlap of the penumbra results in the FOF being underestimated by the two volumetric detectors and the EPID compared to the reference values (TPS data). Less of a spread in data points is observed with an increase in field size closer to 6 x 6 cm^2. However, the difference is well within 0.2% for field sizes above 2 x 2 cm^2 in 6MV FFF beam. The maximum % difference of 0.4 is seen between TPS data and a-Si EPID for the smallest field size of 0.5 x 0.5 cm^2.

In smaller field sizes, it is not practical to minimize the spread of data points due to volume averaging effect of the detectors and LCPE in small field sizes. The entire chamber sensitive volume is outside the fluence. Only the center of the detector is irradiated directly by the primary photon fluence; but the measured signal is averaged over the entire sensitive volume. This results in the underestimation of dose shown by Figures: 4.35, 4.36, and 4.37. There is a big % difference between the TP data and the a-Si EPID, as well as the PTW

3D Semiflex chamber in smaller field sizes

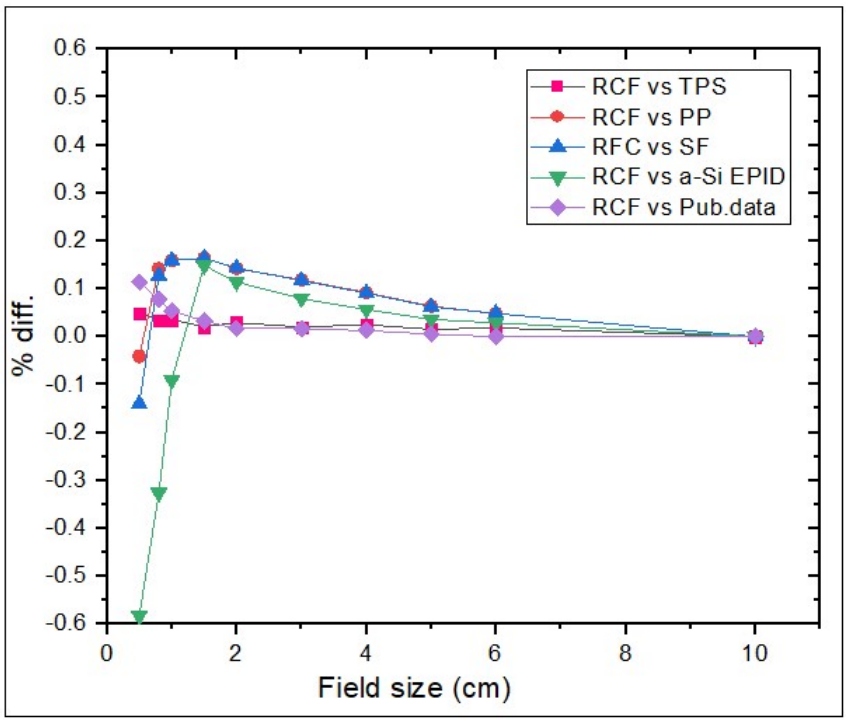

Figure 4.37: Variations in the measured FOF with different detectors used in small photon fields for 10MV FF beam.

The maximum % difference of 0.6 (Figure 4.40 above) is observed between the TPS and EPID data for the smallest field size of 0.5 x 0.5 cm^2. Even though the a-Si EPID is said to have a high spatial resolution, the largest % difference of 0.6 in FOF for the smallest beam size of 0.5 x 0.5 cm^2 was obtained.

The FOF measured with EBT3 film were closer to the calculated TPS data than the other two air-filled ionization chambers and EPID. The ionization chambers (ICs) and the EPID measured the FOF more accurately for field sizes $\geq$ 2 x 2 cm^2 in three photon energies. No results were presented for EPID in 6MV FFF beam.

Chapter 5

Conclusion

The joint IAEA-AAPM TRS 483 protocol addresses dosimetry issues up to 10MV photon beam. Hence only three photon energy beams were used in this study. Various detectors were used to compare with radiochromic film, also to verify their limitations in small field measurements, as well as to examine the differences in their responses.

The measured data was compared to the calculated data from the TP system. As the TPS data was used in this work as a reference data, the maximum % difference obtained between EBT3 and TPS was well below 0.6 for the smallest F/S of 0.5 x 0.5 cm^2 in all three photon energies.

Film dosimetry is quite a lengthy and challenging process, that includes the following: film preparation, i.e handling films with clean gloves to avoid contamination, cutting films to the desired size for measurements, radiation exposure following the desired setup and irradiation parameters, scanning films using a suitable scanner and using the appropriate software for image analysis.

However, its high spatial resolution, and large detection area makes radiochrmic film a reliable reference detector for small FOF measurements. Therefore, repeatability of measurements was required to obtain accurate results. Proper protocol needed to be followed in a clinic to achieve very small uncertainty in the results. Consistence in the time period between irradiation and scanning is very important as the polymerization process continues after exposure to radiation. The 24 hour waiting period between irradiation and scanning was followed in this study, hence there was a huge delay in obtaining the results.

Although, the benefits of using film outweighed the challenges of setting-up a protocol; a new calibration curve for each batch of films must be created due to variation in different batches. The scanning direction also needs to be taken into consideration. Different signal in landscape orientation is obtained compared to portrait direction. Lateral response artifact produced by the scanner due to different film positioning within the scanner is one of the challenges encountered with film measurements. Also, the response of the film at the center of the scanner is different compared to the signal measured at the edges of the film scanner. Calibration curves had to be created for future film dosimetry. Therefore, the calibration was produced for every box of film due to batch to batch variability in sensitivity.

FOF were measured with different detectors to evaluate their limitations in small fields. High spatial resolution to allow accurate measurement of radiation doses at small scales, tissue equivalent and large detection area of radiochromic film made it to be an ideal detector for small FOF measurements. Film improved the accuracy of data collection, and has superior accuracy compared to all the detectors used in this study for beam profiles, FWHM, and FOF measurements. Therefore, it should be regarded as a reference detector for small fields.

The measured data was validated by comparing with the treatment planning data (commissioning data) and the published data. Small volume ion chambers are important small fields output factors measurements. Difference in collection volume produces differences in response due to volume averaging. Different penumbras are expected to be obtained in beam profile measurements.

All the results obtained with various detectors were compared with a reference data from the treatment planning system. FOF measured with the two volumetric detectors and 2-dimensional detectors (RCF and a-Si EPID) were compared to the planning data measured with different set-up. Detector alignment is very crucial in beam profile scanning to accurately determine the beam penumbra. The smallest volume detector is recommended to obtained the most accurate and sharpest penumbra. Small size detector results in a very precise measurements and less volume averaging effect.

Film results were validated by comparing with the published and software-calculated data, i.e TP system. FOF correction factor is not need in film measurements. In volumetric detectors, correction factors obtained from TRS 483 protocol were applied to the ratios of the measured data. This was done to all the small beam sizes below 3 x 3 cm^2. No better detector for small field measurements.

Most literature recommends the use of two or more detectors for small field measurements. Radiochromic films are known for their high dosimetric accuracy when properly calibrated due to their high spatial resolution, tissue-equivalent, minimal energy dependence, and less volume averaging effect. Therefore, RCF was found to be a suitable detector for small fields measurements due to less photon perturbation effect.

Chapter 6

Future work

The % difference between the measured EPID output factors and the calculated TPS data was observed during the measurements to be consistently higher in 6MV FFF beam; hence the a-Si EPID in flattening filter free (FFF) beam for FOF measurements was not used in this study. The discrepancies between the measured FOF with EPID and the FOF predicted by the TPS can be further investigated and corrected as needed

The radiation dose measured by the EPID in small photon fields for unflattened beams, and the influence of back scattered radiation in large fields versus small beams need to be properly evaluated. Therefore, the performance of EPID in FFF beams for small photon fields needs to be further investigated.

Bibliography

[1] Zaigham Abbas and Sakina Rehman. An overview of cancer treatment modalities. *Neoplasm*, 1:139–157, 2018.

[2] Rajamanickam Baskar, Kuo Ann Lee, Richard Yeo, and Kheng-Wei Yeoh. Cancer and radiation therapy: current advances and future directions. *International journal of medical sciences*, 9(3):193, 2012.

[3] Santivasi, Wil L and Xia, Fen. Ionizing radiation-induced DNA damage, response, and repair *Antioxidants & redox signaling*, 21(2):251–259, 2014.

[4] Janessa Laskin, Anthony J Cmelak, Steven Meranze, John Yee, and David H Johnson. Superior vena cava syndrome. In *Abeloff's Clinical Oncology: Fifth Edition*, pages 705–714. Elsevier Inc., 2014.

[5] Fraass, Benedick A and McShan, Daniel L and Ten Haken, Randall K. More than pretty pictures: 3-D treatment planning and conformal therapy *Medical Physics, 21(2):251–259, 2022.*

[6] Rajesh Kinhikar, Vinay Saini, Ritu Raj Upreti, Shrikant Kale, Avadhoot Sutar, Chandrashekhar Tambe, and Sudarshan Kadam. Measurement of the small field output factors for 10 mv photon beam using iaea trs-483 dosimetry protocol and implementation in eclipse tps commissioning. Biomedical Physics & Engineering Express*, 6(6):065005, 2020.*

[7] Ning Wen, Siming Lu, Jinkoo Kim, Yujiao Qin, Yimei Huang, Bo Zhao, Chang Liu, and Indrin J Chetty. Precise film dosimetry for stereotactic radiosurgery and stereotactic body radiotherapy quality assurance using gafchromic™ ebt3 films. Radiation Oncology*, 11(1):1–11, 2016.*

[8] Paolo Francescon, Sam Beddar, Ninfa Satariano, and Indra J Das. Variation of k q clin, q msr f clin, f msr for the small-field dosimetric parameters percentage depth dose, tissue-maximum ratio, and off-axis ratio. Medical physics*, 41(10):101708, 2014.*

[9] *American Association of Physicists in Medicine (AAPM et al. Dosimetry of small static fields used in external beam radiotherapy. an international code of practice for reference and relative dose determination. 2017.*

[10] *Hugo Palmans, Pedro Andreo, M Saiful Huq, Jan Seuntjens, Karen E Christaki, and Ahmed Meghzifene. Dosimetry of small static fields used in external photon beam radiotherapy: Summary of trs-483, the iaea–aapm international code of practice for reference and relative dose determination.* Medical physics*, 45(11):e1123–e1145, 2018.*

[11] *Lewis, David and Micke, Andre and Yu, Xiang and Chan, Maria F. An efficient protocol for radiochromic film dosimetry combining calibration and measurement in a single scan.* Journal of medical physics*, 39(10):6339–6350, 2012.*

[12] *Martin J Butson, KN Peter, Tsang Cheung, and Hani Alnawaf. Energy response of the new ebt2 radiochromic film to x-ray radiation.* Radiation Measurements*, 45(7):836–839, 2010.*

[13] *MM Aspradakis, JP Byrne, H Palmans, S Duane, J Conway, AP Warrington, and K Rosser. Ipem report 103: Small field mv photon dosimetry. Technical report, 2010.*

[14] *Anna Ralston, Paul Liu, Kirbie Warrener, David McKenzie, and Natalka Suchowerska. Small field diode correction factors derived using an air core fibre optic scintillation dosimeter and ebt2 film.* Physics in Medicine & Biology*, 57(9):2587, 2012.*

[15] *Alison JD Scott, Sudhir Kumar, Alan E Nahum, and John D Fenwick. Characterizing the influence of detector density on dosimeter response in non-equilibrium small photon fields.* Physics in Medicine & Biology*, 57(14):4461, 2012.*

[16] *David M Klein, Ramesh C Tailor, Louis Archambault, Lilie Wang, Francois Therriault-Proulx, and A Sam Beddar. Measuring output factors of small fields formed by collimator jaws and multileaf collimator using plastic scintillation detectors.* Medical physics*, 37(10):5541–5549, 2010.*

[17] *E Pantelis, A Moutsatsos, K Zourari, L Petrokokkinos, L Sakelliou, W Kilby, C Antypas, P Papagiannis, P Karaiskos, E Georgiou, et al. On the output factor measurements of the cyberknife iris collimator*

small fields: experimental determination of the correction factors for microchamber and diode detectors. Medical physics, *39(8):4875–4885, 2012.*

[18] Joao Seco, Ben Clasie, and Mike Partridge. Review on the characteristics of radiation detectors for dosimetry and imaging. Physics in Medicine & Biology, *59(20):R303, 2014.*

[19] Hamza Benmakhlouf, Josep Sempau, and Pedro Andreo. Output correction factors for nine small field detectors in 6 mv radiation therapy photon beams: a penelope monte carlo study. Medical physics, *41(4):041711, 2014.*

[20] H Palmans, P Andreo, M Saiful Huq, J Seuntjens, and K Christaki. Dosimetry of small static fields used in external beam radiotherapy: an iaea-aapm international code of practice for reference and relative dose determination. Vienna: International Atomic Energy Agency, *2017.*

[21] Indra J Das. Radiochromic film: role and applications in radiation dosimetry. *CRC Press, 2017.*

[22] Harold, E. The Physics of Radiology Fourth Edition. Charles C Thomas, Springfield, Illionis, USA, 1983.

[23] Wrya Parwaie, Soheila Refahi, Mahdieh Afkhami Ardekani, and Bagher Farhood. Different dosimeters/detectors used in small-field dosimetry: Pros and cons. Journal of medical signals and sensors, *8(3):195, 2018.*

[24] Indra Das. Th-a-213-00: small field dosimetry: overview of aapm tg-155 and the iaeaaapm code of practice. Medical Physics, *42(6Part41):3700–3700, 2015.*

[25] Henry Finlay Godson, M Ravikumar, KM Ganesh, S Sathiyan, and Y Retna Ponmalar. Small field output factors: Comparison of measurements with various detectors and effects of detector orientation with primary jaw setting. Radiation Measurements, *85:99–110, 2016.*

[26] Arash Darafsheh. Radiation Therapy Dosimetry: A Practical Handbook. *CRC Press, 2021.*

[27] Pavlos Papaconstadopoulos. On the detector response and the reconstruction of the source intensity distribution in small photon fields. *McGill University (Canada), 2016.*

[28] *Indra J Das, George X Ding, and Anders Ahnesjö. Small fields: nonequilibrium radiation dosimetry.* Medical physics, *35(1):206–215, 2008.*

[29] *Pedro Andreo, David T Burns, Alan E Nahum, Jan Seuntjens, and Frank Herbert Attix.* Fundamentals of ionizing radiation dosimetry. *John Wiley & Sons, 2017.*

[30] *Stanley H Benedict, Kamil M Yenice, David Followill, James M Galvin, William Hinson, Brian Kavanagh, Paul Keall, Michael Lovelock, Sanford Meeks, Lech Papiez, et al. Stereotactic body radiation therapy: the report of aapm task group 101.* Medical physics, *37(8):4078–4101, 2010.*

[31] *Christian P Karger, Oliver Jäkel, Hugo Palmans, and Tatsuaki Kanai. Dosimetry for ion beam radiotherapy.* Physics in Medicine & Biology, *55(21):R193, 2010.*

[32] *International Commission on Radiation Units and Measurements.* Fundamental quantities and units for ionizing radiation. *International commission on radiation units and measurements, 1998.*

[33] *M Saiful Huq. Absorbed dose determination in external beam radiotherapy: an international code of practice for dosimetry based on standards of absorbed dose to water. 2006.*

[34] *Faiz M Khan and John P Gibbons.* Khan's the physics of radiation therapy. *Lippincott Williams & Wilkins, 2014.*

[35] *Peter R Almond, Peter J Biggs, Bert M Coursey, William F Hanson, M Saiful Huq, Ravinder Nath, and David WO Rogers. Aapm's tg-51 protocol for clinical reference dosimetry of high-energy photon and electron beams.* Medical physics, *26(9):1847–1870, 1999.*

[36] *Ervin B Podgorsak et al.* Radiation oncology physics. *IAEA Vienna, 2005.*

[37] *AAPM Task Group 21, Radiation Therapy Committee. A protocol for the determination of absorbed dose from high-energy photon and electron beams.* Medical Physics, *10(6):741–771, 1983.*

[38] *LV Spencer and Frank H Attix. A theory of cavity ionization.* Radiation research, *3(3):239–254, 1955.*

[39] *P Francescon, S Cora, and N Satariano. Calculation of for several small detectors and for two linear accelerators using monte carlo simulations.* Medical physics, *38(12):6513–6527, 2011.*

[40] *Johnny E Morales, Martin Butson, Scott B Crowe, Robin Hill, and JV Trapp. An experimental extrapolation technique using the gafchromic ebt3 film for relative output factor measurements in small x-ray fields.* Medical Physics, *43(8Part1):4687–4692, 2016.*

[41] *P Francescon, W Kilby, and N Satariano. Monte carlo simulated correction factors for output factor measurement with the cyberknife system—results for new detectors and correction factor dependence on measurement distance and detector orientation.* Physics in Medicine & Biology, *59(6):N11, 2014.*

[42] *Božidar Casar, Eduard Gershkevitsh, Ignasi Mendez, Slaven Jurković, and M Saiful Huq. A novel method for the determination of field output factors and output correction factors for small static fields for six diodes and a microdiamond detector in megavoltage photon beams.* Medical physics, *46(2):944–963, 2019.*

[43] *Daniela Poppinga, Bjoern Delfs, Jutta Meyners, Dietrich Harder, Björn Poppe, and Hui Khee Looe. The output factor correction as function of the photon beam field size–direct measurement and calculation from the lateral dose response functions of gas-filled and solid detectors.* Zeitschrift für Medizinische Physik, *28(3):224–235, 2018.*

[44] *PTW, F. Ionizing radiation detectors including codes of practice 2017.*

[45] *Madelaine Tyler, Paul ZY Liu, Kin Wa Chan, Anna Ralston, David R McKenzie, Simon Downes, and Natalka Suchowerska. Characterization of small-field stereotactic radiosurgery beams with modern detectors.* Physics in Medicine & Biology, *58(21):7595, 2013.*

[46] *Godfrey Azangwe, Paulina Grochowska, Dietmar Georg, Joanna Izewska, Johannes Hopfgartner, Wolfgang Lechner, Claus E Andersen, Anders R Beierholm, Jakob Helt-Hansen, Hideyuki Mizuno, et al. Detector to detector corrections: a comprehensive experimental study of detector specific correction factors for beam output measurements for small radiotherapy beams.* Medical physics, *41(7):072103, 2014.*

[47] Antonella Fogliata and Luca Cozzi. Dose calculation algorithm accuracy for small fields in non-homogeneous media: the lung sbrt case. Physica Medica*, 44:157–162, 2017.*

[48] N Papanikolaou, JJ Battista, AL Boyer, C Kappas, E Klein, TR Mackie, M Sharpe, and J Van Dyk. Tissue inhomogeneity corrections for megavoltage photon beams aapm report 85. Medical Physics Pub for AAPM, New York*, page 8, 2004.*

[49] Sujatha Pai, Indra J Das, James F Dempsey, Kwok L Lam, Thomas J LoSasso, Arthur J Olch, Jatinder R Palta, Lawrence E Reinstein, Dan Ritt, and Ellen E Wilcox. Tg-69: radiographic film for megavoltage beam dosimetry. Medical physics*, 34(6Part1):2228–2258, 2007.*

[50] Martin J Butson, KN Peter, Tsang Cheung, and Peter Metcalfe. Radiochromic film for medical radiation dosimetry. Materials Science and Engineering: R: Reports*, 41(3-5):61–120, 2003.*

[51] Jefferson Sorriaux, A Kacperek, Séverine Rossomme, John Aldo Lee, D Bertrand, Stefaan Vynckier, and Edmond Sterpin. Evaluation of gafchromic® ebt3 films characteristics in therapy photon, electron and proton beams. Physica Medica*, 29(6):599–606, 2013.*

[52] Azam Niroomand-Rad, Charles Robert Blackwell, Bert M Coursey, Kenneth P Gall, James M Galvin, William L McLaughlin, Ali S Meigooni, Ravinder Nath, James E Rodgers, and Christopher G Soares. Radiochromic film dosimetry: recommendations of aapm radiation therapy committee task group 55. Medical physics*, 25(11):2093–2115, 1998.*

[53] Walt Bogdanich. Radiation offers new cures, and ways to do harm. New York Times*, 23:A1, 2010.*

[54] Antonio Gonzalez-Lopez, Juan-Antonio Vera-Sanchez, and Jose-Domingo Lago-Martin. Small fields measurements with radiochromic films. Journal of Medical Physics/Association of Medical Physicists of India*, 40(2):61, 2015.*

[55] Valeria Casanova Borca, Massimo Pasquino, Giuliana Russo, Pierangelo Grosso, Domenico Cante, Piera Sciacero, Giuseppe Girelli, Maria Rosa La Porta, and Santi Tofani. Dosimetric characterization and use of gafchromic ebt3 film for imrt dose verification. Journal of applied clinical medical physics*, 14(2):158–171, 2013.*

[56] MS Windows NT kernel description. `www.gafchromic.com`. *Accessed: 2021-10-13.*

[57] D Lewis. Radiochromic film. Wayne, NJ: International Specialty Products, *2010.*

[58] Wouter Crijns, Frederik Maes, UA Van Der Heide, and Frank Van den Heuvel. Calibrating page sized gafchromic ebt3 films. Medical physics, *40(1):012102, 2013.*

[59] Matthew Williams and Peter Metcalfe. Radiochromic film dosimetry and its applications in radiotherapy. In AIP Conference Proceedings, *volume 1345, pages 75–99. American Institute of Physics, 2011.*

[60] G Twork and A Sarfehnia. Su-e-t-88: Evaluation of the dose-rate dependency of gafchromic ebt3. Medical Physics, *40(6Part11):223–224, 2013.*

[61] Gary A Ezzell, Jay W Burmeister, Nesrin Dogan, Thomas J LoSasso, James G Mechalakos, Dimitris Mihailidis, Andrea Molineu, Jatinder R Palta, Chester R Ramsey, Bill J Salter, et al. Imrt commissioning: multiple institution planning and dosimetry comparisons, a report from aapm task group 119. Medical physics, *36(11):5359–5373, 2009.*

[62] Hossein Hassani, Hassan Ali Nedaie, Mohammad Hassan Zahmatkesh, and Kaveh Shirani. A dosimetric study of small photon fields using polymer gel and gafchromic ebt films. Medical dosimetry, *39(1):102–107, 2014.*

[63] Antony L Palmer, Alexis Dimitriadis, Andrew Nisbet, and Catharine H Clark. Evaluation of gafchromic ebt-xd film, with comparison to ebt3 film, and application in high dose radiotherapy verification. Physics in Medicine & Biology, *60(22):8741, 2015.*

[64] Livia Marrazzo, Margherita Zani, Stefania Pallotta, Chiara Arilli, Marta Casati, Antonella Compagnucci, Cinzia Talamonti, and Marta Bucciolini. Gafchromic® ebt3 films for patient specific imrt qa using a multichannel approach. Physica medica, *31(8):1035–1042, 2015.*

[65] Andre Micke, David F Lewis, and Xiang Yu. Multichannel film dosimetry with nonuniformity correction. Medical physics, *38(5):2523–2534, 2011.*

[66] S Thongsawad, S Srisatit, and T Fuangrod. Error detection sensitivity test using complex errors on three patient-specific vmat qa systems. In Journal of Physics: Conference Series*, volume 1285, page 012030. IOP Publishing, 2019.*

[67] Larry E Antonuk. Electronic portal imaging devices: a review and historical perspective of contemporary technologies and research. Physics in Medicine & Biology*, 47(6):R31, 2002.*

[68] Philip Vial, Peter B Greer, Lyn Oliver, and Clive Baldock. Initial evaluation of a commercial epid modified to a novel direct-detection configuration for radiotherapy dosimetry. Medical physics*, 35(10):4362–4374, 2008.*

[69] Mahsheed Sabet, Frederick W Menk, and Peter B Greer. Evaluation of an a-si epid in direct detection configuration as a water-equivalent dosimeter for transit dosimetry. Medical physics*, 37(4):1459–1467, 2010.*

[70] Wouter Van Elmpt, Leah McDermott, Sebastiaan Nijsten, Markus Wendling, Philippe Lambin, and Ben Mijnheer. A literature review of electronic portal imaging for radiotherapy dosimetry. Radiotherapy and oncology*, 88(3):289–309, 2008.*

[71] Giuseppe Stella, Nina Cavalli, Elisa Bonanno, Lucia Zirone, Giuseppina Rita Borzì, Martina Pace, Andrea Girlando, Anna M Gueli, and Carmelo Marino. Sbrt/srs patient-specific qa using gafchromic™ ebt3 and filmqa™ pro software. Journal of Radiosurgery & SBRT*, 8(1), 2022.*

[72] G Nicolini, A Clivio, E Vanetti, H Krauss, P Fenoglietto, L Cozzi, and A Fogliata. Evaluation of an asi-epid with flattening filter free beams: applicability to the glaas algorithm for portal dosimetry and first experience for pretreatment qa of rapidarc. Medical physics*, 40(11):111719, 2013.*

[73] Giorgia Nicolini, Eugenio Vanetti, Alessandro Clivio, Antonella Fogliata, Stine Korreman, Jiri Bocanek, and Luca Cozzi. The glaas algorithm for portal dosimetry and quality assurance of rapidarc, an intensity modulated rotational therapy. Radiation Oncology*, 3(1):1–10, 2008.*

[74] Arpita Agarwal, Nikhil Rastogi, KJ Maria Das, SA Yoganathan, D Udayakumar, and Shaleen Kumar. Investigating the electronic portal imaging device for small radiation field measurements. Journal of Medical Physics*, 42(2):59, 2017.*

[75] *Tsang Cheung, Martin J Butson, and KN Peter. Post-irradiation colouration of gafchromic ebt radiochromic film.* Physics in Medicine & Biology, *50(20):N281, 2005.*

[76] *S Reinhardt, M Hillbrand, JJ Wilkens, and W Assmann. Comparison of gafchromic ebt2 and ebt3 films for clinical photon and proton beams.* Medical physics, *39(8):5257–5262, 2012.*

[77] *Itumeleng Setilo, Oluwaseyi Michael Oderinde, and Freek Cp du Plessis. The effect of ssd, field size, energy and detector type for relative output factor measurement in small photon beams as compared with monte carlo simulation.* Polish Journal of Medical Physics and Engineering, *25(2):101–110, 2019.*